

Mazin Al-saedi

## **FLEXIBLE MULTIBODY DYNAMICS AND INTELLIGENT CONTROL OF A HYDRAULICALLY DRIVEN HYBRID REDUNDANT ROBOT MACHINE**

Thesis for the degree of Doctor of Science (Technology) to be presented  
with due permission for public examination and criticism in the Auditorium  
of 1382 at Lappeenranta University of Technology, Lappeenranta, Finland  
on the 3rd of June, 2014, at noon.

- Supervisor Professor Heikki Handroos  
Laboratory of Intelligent Machines  
Faculty of Technology  
Lappeenranta University of Technology  
Finland
- Reviewers Professor Giuseppe Carbone  
Laboratory of Robotics and Mechatronics  
University of Cassino  
Italy
- Professor Fernando Gomez-Bravo  
Departamento de Ingeniería Electrónica de Sistemas Informáticos y  
Automática.  
University of Huelva  
Spain
- Opponents Professor Giuseppe Carbone  
Laboratory of Robotics and Mechatronics  
University of Cassino  
Italy
- Professor Fernando Gomez-Bravo  
Departamento de Ingeniería Electrónica de Sistemas Informáticos y  
Automática.  
University of Huelva  
Spain

ISBN 978-952-265-594-3  
ISBN 978-952-265-595-0 (PDF)  
ISSN-L 1456-4491  
ISSN 1456-4491  
Lappeenrannan teknillinen yliopisto  
Yliopistopaino 2014

## **Abstract**

**Mazin Al-saedi**

**Flexible multibody dynamics and intelligent control of a hydraulically driven hybrid redundant robot machine**

Lappeenranta 2014

144 pages

Acta Universitatis Lappeenrantaensis 577

Diss. Lappeenranta University of Technology

ISBN 978-952-265-594-3, ISBN 978-952-265-595-0 (PDF), ISSN-L 1456-4491,

ISSN 1456-4491.

The assembly and maintenance of the International Thermonuclear Experimental Reactor (ITER) vacuum vessel (VV) is highly challenging since the tasks performed by the robot involve welding, material handling, and machine cutting from inside the VV. The VV is made of stainless steel, which has poor machinability and tends to work harden very rapidly, and all the machining operations need to be carried out from inside of the ITER VV. A general industrial robot cannot be used due to its poor stiffness in the heavy duty machining process, and this will cause many problems, such as poor surface quality, tool damage, low accuracy. Therefore, one of the most suitable options should be a light weight mobile robot which is able to move around inside of the VV and perform different machining tasks by replacing different cutting tools.

Reducing the mass of the robot manipulators offers many advantages: reduced material costs, reduced power consumption, the possibility of using smaller actuators, and a higher payload-to-robot weight ratio. Offsetting these advantages, the lighter weight robot is more flexible, which makes it more difficult to control. To achieve good machining surface quality, the tracking of the end effector must be accurate, and an accurate model for a more flexible robot must be constructed.

This thesis studies the dynamics and control of a 10 degree-of-freedom (DOF) redundant hybrid robot (4-DOF serial mechanism and 6-DOF 6-UPS hexapod parallel mechanisms) hydraulically driven with flexible rods under the influence of machining forces. Firstly, the flexibility of the bodies is described using the floating frame of reference method (FFRF). A finite element model (FEM) provided the Craig-Bampton (CB) modes needed for the FFRF. A dynamic model of the system of six closed loop mechanisms was assembled using the constrained Lagrange equations and the Lagrange multiplier method. Subsequently, the reaction forces between the parallel and serial parts were used to study the dynamics of the serial robot. A PID control based on position predictions was implemented independently to control the hydraulic cylinders of the robot.

Secondly, in machining, to achieve greater end effector trajectory tracking accuracy for surface quality, a robust control of the actuators for the flexible link has to be deduced. This thesis investigates the intelligent control of a hydraulically driven parallel robot part based on the dynamic model and two schemes of intelligent control for a

hydraulically driven parallel mechanism based on the dynamic model: (1) a fuzzy-PID self-tuning controller composed of the conventional PID control and with fuzzy logic, and (2) adaptive neuro-fuzzy inference system-PID (ANFIS-PID) self-tuning of the gains of the PID controller, which are implemented independently to control each hydraulic cylinder of the parallel mechanism based on rod length predictions. The serial component of the hybrid robot can be analyzed using the equilibrium of reaction forces at the universal joint connections of the hexa-element. To achieve precise positional control of the end effector for maximum precision machining, the hydraulic cylinder should be controlled to hold the hexa-element.

Thirdly, a finite element approach of multibody systems using the Special Euclidean group  $SE(3)$  framework is presented for a parallel mechanism with flexible piston rods under the influence of machining forces. The flexibility of the bodies is described using the nonlinear interpolation method with an exponential map. The equations of motion take the form of a differential algebraic equation on a Lie group, which is solved using a Lie group time integration scheme. The method relies on the local description of motions, so that it provides a singularity-free formulation, and no parameterization of the nodal variables needs to be introduced. The flexible slider constraint is formulated using a Lie group and used for modeling a flexible rod sliding inside a cylinder. The dynamic model of the system of six closed loop mechanisms was assembled using Hamilton's principle and the Lagrange multiplier method. A linearized hydraulic control system based on rod length predictions was implemented independently to control the hydraulic cylinders.

Consequently, the results of the simulations demonstrating the behavior of the robot machine are presented for each case study.

In conclusion, this thesis studies the dynamic analysis of a special hybrid (serial-parallel) robot for the above-mentioned special task involving the ITER and investigates different control algorithms that can significantly improve machining performance. These analyses and results provide valuable insight into the design and control of the parallel robot with flexible rods.

**Keywords:** hybrid robot, flexible multibody dynamics, floating frame of reference, hydraulic control, Adaptive Neural Fuzzy control, Lie group, Special Euclidean group.

UDC: 531.3:62-231.3:621.865.8:519.2:510.22:51.001.57

## Acknowledgements

I would like to express my deepest gratitude to my supervisor Professor Dr. Heikki Handroos and to Associated Professor Dr. Huapeng Wu for making this thesis possible. I am grateful for the opportunity I was given to participate in this most interesting research project and will always be thankful for their reading of the early drafts of my proposal, their insightful technical and editorial advice, their suggestions and continuous encouragement, and their patient assistance.

I would also like to recognize Dr. Oleg Dmitrochenko and Dr. Tuomas Rantalainen, who were great sources of inspiration. I thank them for their guidance and encouragement throughout my doctoral studies, for their tireless efforts to provide me with an excellent understanding of the research environment, and for teaching me the analytical rigors of advanced mathematics of multibody dynamics. Finally, I am grateful that Oleg and Tuomas always took the time to help me whenever I knocked on their doors.

In the course of my studies, the Laboratory of Intelligent Machines afforded me many opportunities to attend relevant international conferences. These events helped me to gain knowledge in my area of research and to develop a better understanding of international culture.

I also benefited a great deal from my research visit to the Multibody and Mechatronic Systems Lab, LTAS, University of Liege, Belgium. I wish to express my thanks to Professor Dr. Olivier Bruls for his cheerful welcome to his lab in the summer of 2013 and for ensuring that my stay was as profitable as possible. I especially appreciated the collaboration with Valentin Sonneville. Our numerous discussions were invaluable to the elaboration of the fourth chapter of my thesis.

A warm thank you goes to all the members of our sister laboratory at the Lappeenranta University of Technology, the Laboratory of Machine Design. Special thanks go to Prof. Dr. Aki Mikkola, John Bruzzo Escalante, Emil Kurvinen, Elias Altarriba, Janne Heikkinen, Antti Valkeapää, Dr. Marko Matikainen, and R Scott Semken.

To all my colleagues and friends at the university, I offer my deepest gratitude for the pleasant work environment and colorful leisure time. I will never forget the colleagues and friends with whom I shared many enjoyable discussions and memorable moments: Dr. Rafael Åman, Dr. Pasi Luukka, Lauri Luostarinen, Dr. Yongbo Wang, Ming Li, Juha Koivisto, Anna-Kaisa Partanen, and Eeva Häyrinen.

Last, but not least, I would like to give my heartfelt thanks to my brothers and sisters. I am greatly in debt to all my family members for their encouragement and support. Finally, I would like to dedicate this thesis to my dearest parents, who gave me unconditionally throughout my life their kindly support, motivation, patience, and care.

Mazin Al-saedi

June 2014

Lappeenranta, Finland



# Contents

Abstract

Acknowledgements

## Contents

<b>Nomenclature</b>	<b>9</b>
<b>1 Introduction</b>	<b>15</b>
1.1 The International Thermonuclear Experimental Reactor (ITER).....	15
1.2 Main types of hybrid (serial-parallel) robots .....	15
1.3 Flexible multibody dynamics.....	18
1.4 ANFIS and fuzzy tuning of a PID controller for trajectory tracking of a flexible hydraulically driven parallel robot machine .....	21
1.5 Special Euclidean group for dynamics and control.....	23
1.6 Objectives of the study .....	25
1.7 Outline of the thesis.....	27
1.8 Scientific contributions and publications .....	28
<b>2 Flexible multibody dynamics using the FFRF technique and PID control</b>	<b>31</b>
2.1 Strain Analysis in multibody dynamics.....	31
2.2 Coordinate System of a Hybrid Robot .....	32
2.2.1 Description a hybrid robot .....	32
2.2.2 Inverse kinematics of 6-UPS parallel robot.....	34
2.2.3 Spatial coordinate system of a parallel robot arm.....	36
2.2.4 The rotation matrix and the Euler parameters.....	37
2.3 Description of a flexible body.....	40
2.3.1 Component mode synthesis .....	40
2.3.2 Equation of motion of a multibody system.....	42
2.4 Modeling of constraints .....	45
2.4.1 Kinematic joint description.....	45
2.4.2 Basic constraint equations .....	46
2.5 Dynamic equation of the six closed loop parallel mechanism.....	48
2.6 Forces of a hydraulic cylinder.....	49
2.6.1 Generalized forces of a hydraulic cylinder .....	49
2.6.2 Derivation of the hydraulic forces.....	50
2.6.3 PID control of the parallel mechanism .....	54
Summary .....	56
2.7 Analysis of the serial part of the hybrid robot .....	57
2.8 Robot parameters .....	59
2.9 Discussion.....	60
2.10 Simulation results .....	62
<b>3 Intelligent methods for tuning the PID controller of a hybrid robot</b>	<b>73</b>

3.1	Introduction.....	73
3.2	Fuzzy method for tuning the PID gains.....	74
3.2.1	Fuzzy controller and its membership function.....	74
3.3	ANFIS controller.....	81
3.3.1	Learning and adaptation in fuzzy systems via a neural network	82
3.3.2	ANFIS algorithm and structure:.....	86
3.4	Robot parameters, simulation results and discussion.....	89
3.5	Analysis of the serial part of the hybrid robot .....	96
<b>4</b>	<b>Special Euclidean group for flexible multibody dynamics of a hydraulically driven parallel mechanism</b>	<b>99</b>
4.1	Fundamentals of the Special Euclidean group, $SE(3)$ .....	99
4.2	General description of multibody systems .....	103
4.3	Modeling of constraints .....	104
4.3.1	Kinematic of joint description.....	104
4.3.2	Kinematics of a multibody system .....	106
4.3.3	Constraint equations .....	107
4.3.4	Constraint gradient .....	109
4.4	Flexible beam.....	110
4.4.1	Beam kinematics .....	110
4.4.2	Kinetic and strain energies.....	111
4.4.3	Finite element discretization .....	112
4.4.4	Discretized beam equations .....	113
4.5	Flexible sliding joint.....	114
4.6	Hydraulic control .....	116
4.6.1	Derivation of the hydraulic forces.....	116
4.6.2	PID control of the parallel robot .....	118
4.7	Dynamic equations of mechatronic systems.....	119
4.7.1	Dynamic equations .....	119
4.7.2	Description of the integration algorithm.....	120
4.8	Robot parameters .....	123
4.9	Discussion.....	123
4.10	Simulation results .....	125
<b>5</b>	<b>Conclusions</b>	<b>131</b>
5.1	Key results of the work.....	131
	Conclusion 1 .....	131
	Conclusion 2 .....	131
	Conclusion 3 .....	132
5.2	Suggestions for improving performance of the hybrid robot and for the future work.....	134
	<b>References</b>	<b>135</b>



## Nomenclature

### Latin alphabet

$0$	zero matrix	
$\mathbf{A}^i$	the rotation matrix of a body $i$	
$\mathbf{A}_f^{Pi}$	is a rotation matrix that describes the orientation due to deformation at the location of node $P^i$ with respect to the local frame	
$A_2, A_1$	the infill and return effective action areas	$m^2$
$\bar{\mathbf{a}}_i^{cr}$	the relative acceleration of rod with respect to cylinder	
$Be$	the water bulk modules	
$b$	the coefficient of friction (impedance coefficient)	$N.s/m$
$\mathbf{C}$	is the vector of nonlinear constraint equations of the parallel robot	
$\mathbf{C}_q$	the Jacobian matrix of the nonlinear constraint equations	
$\mathbf{C}^s$	basic constraints of spherical constraint on two points	
$\mathbf{C}^{d1}$	basic constraints of perpendicular constraint type 1	
$\mathbf{C}^{d2}$	basic constraints of Perpendicular constraint type 2	
$C_{ic}$	internal leakage	
$\mathbf{C}_{\bar{\theta}i}$	the Jacobian matrix for generalized coordinates related to the orientation	
$\mathbf{C}_{qf^i}$	the Jacobian matrix for generalized coordinates related to the flexibility	
$c_v$	the flow coefficient of the orifice	
$\mathbf{d}^{ij}$	a vector from $P^i$ to $P^j$ defined in the global coordinate system	
$\mathbf{d}$	the relative configuration vector	
$E$	Young's modulus	
$e$	the error between the predicted $l_d$ and presented $l$ lengths	
$\dot{e}$	the error derivative between the predicted $l_d$ and presented $l$ lengths	
$\mathbf{e}_{l,U}$	the displacement parts of the relative motions.	
$\mathbf{e}_{l,\Omega}$	the rotation parts of the relative motions.	
$e_0^i, e_1^i, e_2^i, e_3^i$	Euler parameters of each cylinder	
$\exp_{SO(3)}$	the exponential map of the Special Orthogonal group	
$\exp_{SE(3)}$	the exponential map of the Special Orthogonal group.	
$\mathbf{f}^0$	deformation gradient in the reference configuration	
$\mathbf{F}_f^i$	the vector of the external forces associated with the nodal coordinates of the flexible body	
$G$	group contains elements	
$J$	the second moment of inertia	

---

$\mathbf{H}$	the group of homogenous transformations combining a rotation matrix and a position vector.	
$\mathbf{H}_A, \mathbf{H}_B$	the nodal homogeneous matrices of respectively node A and B	
$\mathbf{H}_{j,I}$	is a homogeneous matrix that describes the relative motion between the two nodes due to the joint I.	
$\mathbf{H}_0$	nodal material frames at node in the initial state	
$\mathbf{H}_j, \mathbf{H}_{j+1}$	nodal material frames at nodes $s_j$ and $s_{j+1}$ respectively.	
$\tilde{\mathbf{h}}$	the $4 \times 4$ matrix $\tilde{\mathbf{h}}$ belongs to $\mathfrak{se}(3)$ , the Lie algebra of $SE(3)$	
$\mathbf{h}_U$	the position elements of $\tilde{\mathbf{h}}$	
$\mathbf{h}_\Omega$	the set of skew-symmetric matrices built upon the three components of $\mathbf{h}_\Omega$	
$\mathbf{I}$	the $3 \times 3$ identity matrix	
$\mathbf{g}_{ext}$	the external forces vector	
$\mathbf{K}_p$	the proportional coefficient gain	
$\mathbf{K}_d$	the derived coefficient gain	
$\mathbf{K}_i$	the integral coefficient gain	
$\mathbf{K}_U$	stiffness matrix contains the axial and shear stiffnesses	
$\mathbf{K}_\Omega$	stiffness matrix contains the torsional and bending stiffnesses	
$\mathbf{K}_{CB}^i$	The modal stiffness matrix of the flexible body	
$\mathbf{K}_{orth}^i$	the diagonal modal stiffness matrices of the orthonormalized CB modes.	
$f$	frequency	
$F_x$	the machining force in the x direction	
$F_y$	the machining force in the y direction	
$F_z$	the machining force in the z direction	
$\mathbf{F}_{hi}$	The hydraulic forces inside each cylinder	
$\log_{SO(3)}$	the logarithmic map of the Special Orthogonal group.	
$\mathbf{M}_{CB}^i$	The modal mass matrix of the flexible body	
$\mathbf{M}_{arm}^i$	The mass matrix of each arm of the parallel robot	
$\mathbf{M}_{orth}^i$	the diagonal modal mass matrices of the orthonormalized CB modes.	
$\mathbf{n}_U$	the position elements of given six-dimensional vector	
$\mathbf{n}_\Omega$	the rotation elements of given six-dimensional vector	
$n_c$	set of nonlinear algebraic constraint equations	
$n$	generalized coordinates of all bodies of the parallel robot	
$\mathbf{O}_0$	a constant rotation matrix built on the unit vectors along the neutral axis and the cross-sections that accounts for the orientation of the beam in the reference configuration with respect to the inertial frame.	
$P_L$	the load pressure	
$P_1, P_2$	the infill and return water cavity pressures	Pa

$p_s$	the pressure of the system source	
$\mathbf{Q}_e^i$	the vector of generalized external forces associated with generalized coordinates of body i	
$\mathbf{Q}_f^i$	The vector of the elastic force	
$\mathbf{Q}_v$	a quadratic velocity vector	
$\mathbf{Q}^c$	the constraint force vector for the system	
$\mathbf{q}^{iT}$	the generalized coordinates defining the position of node $P^i$	
$\dot{\mathbf{q}}^i$	the generalized coordinates defining the velocity of node $P^i$	
$q_1, q_2$	elements of group	
$Q_L$	the load flow	
$Q_1, Q_2$	the infill and return flows	$m^3/s$
$\mathbf{R}$	a rotation matrix	
$\mathbb{R}^3$	Euclidian vector of three dimension	
$\mathbf{r}_i^{cr}$	The unit vector of the relative position of the coordinate system of a rod to the coordinate system of a cylinder in the global system	
$\mathbf{r}_i^r$	the global position of the coordinate system of a rod	
$\mathbf{r}_i^c$	the global position of the coordinate system of a cylinder	
$\dot{\mathbf{r}}^i$	the global velocity vector of an arbitrary point on the body	
$s$	the spatial parameter along the neutral axis of a beam	
$\mathbf{T}^i$	The kinetic energy of a one beam element	
$\mathbf{T}_{SO(3)}$	tangent operator	
$t$	time	
$\bar{\mathbf{u}}_f^{Pi}$	the vectors describing the translational deformed positions of node $P^i$ with respect to a flexible body i reference coordinate system	
$V^i$	the volume of body i	$m^3$
$V_1, V_2$	the infill and return volumes inside cylinder	$m^3$
$\bar{\mathbf{v}}_f^i$	The vector due to deformation at the location of node $P^i$ within the frame of reference	
$\bar{\mathbf{v}}^i$	a unit vector defined in the undeformed state emanating from node $P^i$	
$\bar{\mathbf{v}}_i^{cr}$	the relative velocity of rod with respect to cylinder	
$\mathbf{v}_{J,I}$	a $6 \times 1$ vector related to the time derivative of the transformation matrix $H_{J,I}$	
$\mathbf{v}_{j,I}$	the time derivative coordinates $\alpha_j$	
$W_s^i$	the virtual work of the elastic forces resulting from the deformation of a rod	
$W_e^i$	the virtual work due to externally applied forces	
$x_v$	the spool position	

$\mathbf{x}$	a position vector
$\underline{\mathbf{x}}_{\max}, \underline{\mathbf{x}}_{\min}$	the maximum and minimum of the input values of error
$\underline{\mathbf{y}}_{\max}, \underline{\mathbf{y}}_{\min}$	the maximum and minimum of the input values of error dot
$\mathbf{x}'_i, \mathbf{y}'_i, \mathbf{z}'_i$	the coordinate system

### Greek alphabet

$\zeta_i$	the vector joint of the $i^{\text{th}}$ cylinder on the fixed plate with respect to frame O
$\alpha, \beta, \gamma$	Euler angles
$\dot{\alpha}_i$	relative velocity
$\Gamma_i$	the rotation matrix of the $x'_i, y'_i, z'_i$ coordinate system with respect to global system
$\delta^i$	the vector of the physical displacement of the node (the nodal coordinates)
$\ddot{\delta}^i$	the vector second derivative of the physical displacement of the node (the nodal coordinates)
$\delta \mathbf{h}$	the variation of $\mathbf{h}$
$\boldsymbol{\varepsilon}^{Pi}$	the vector that represents the rotation of an infinitesimal volume at the node $P^i$ with respect to flexible body $i$ coordinate system
$\tilde{\boldsymbol{\varepsilon}}^{Pi}$	a skew symmetric matrix associated with the vector $\boldsymbol{\varepsilon}^{Pi}$
$\varepsilon$	deformation
$\eta$	coordinate for the position of body $l$ along the flexible body
${}^e \boldsymbol{\theta}^i$	vector of Euler parameters of each cylinder
$A$	rotation angle of the rotation table
$\lambda$	weight coefficient (crisp value)
$\boldsymbol{\lambda}$	the vector of Lagrange multipliers
$\mu(z)$	the membership degree of the output
$\pi$	tilting angle of the hexa-element
$\Phi^{iP}$	The Craig-Bampton modal matrix
$\Phi_R^{iP}$	the modal matrix whose columns describe only the translational mode shapes
$\Phi_\theta^{iP}$	the modal matrix that describes the rotational mode shapes
$\rho^i$	the mass density of body $i$
$\Phi_C^i$	the matrix of static correction modes
$\Phi_N^i$	A shape matrix that contains only normal modes
$\Phi_{CB}^i$	the non-orthogonal CB deformation modes
$\phi_{jN}^i$	eigenvectors which are called normal modes

---

$\Psi$	the constraint equations
$\Psi_q$	the constraint gradient
$\omega_{jN}^i$	a set of the $j^{\text{th}}$ eigenvalues or natural frequencies
$\hat{\omega}_j^i$	a set of eigenvalues or natural frequencies associated with the selected orthonormalized CB modes



## 1 Introduction

### 1.1 The International Thermonuclear Experimental Reactor (ITER)

To match the requirements of field work specifications, a hybrid redundant robot integrates the benefits of both serial and parallel kinematics, for instance, the large workspace of serial robots, the good stiffness performance of parallel robots, and high accuracy. The assembly and maintenance of International Thermonuclear Experimental Reactor (ITER) (Figure 1.1) vacuum vessel (VV) (Figure 1.1) is highly challenging since the tasks performed by the robot involve welding, remote material handling, and machine cutting from inside the VV (Pessi *et al.*, 2007). The VV is made of stainless steel which have poor machinability compared to regular carbon steel because they are tougher, gummier and tend to work harden very rapidly, and all the machining operations need to be carried out from inside of ITER VV. Commercially available CNC machining center cannot be used for this purpose due to its big size and high weight. Furthermore, the general industrial serial robot cannot be used due to its poor stiffness in the heavy duty machining process, and this will cause lots of problems: bad surface quality, tool damage, bad accuracy and so on. Therefore, one of the most suitable options should be a light weight mobile robot which has the ability of moving around inside of VV and performing different machining tasks by replacing different cutting tools as shown in Figure 1.3 and Figure 1.4. Consequently, a hybrid parallel-serial robot (Figure 1.2) has been developed that has ten degrees of freedom (DOF). A Stewart parallel mechanism contributes six DOF, and the serial mechanism provides the remaining four.

### 1.2 Main types of hybrid (serial-parallel) robots

There are two main types of hybrid (serial-parallel) robots:

- 1- Serial-parallel configuration.
- 2- Parallel-serial configuration.

The robot under study is considered as hybrid (serial-parallel) robot machine. However, the first type is distinguished by: fast end-effector, big volume of working space, high local speed and high local acceleration (due to short links), and long trajectories. Therefore, this type of hybrid robot is used for machining applications like laser cutting and assembling tasks. Conversely, the second type of hybrid robot (parallel-serial) is distinguished by: slow speed of the end effector, small volume of working space, and local speed is not high. However, this type has stiffer base because the base is the parallel mechanism structure. This kind of hybrid robot is able to operate with high

performances operations such as surgery applications (Carbone *et al.*, 2001), also for performing a multi-step arc welding process, where this kind of robot is highly capable of reducing the actuating energy (Mohammadipanah and Zohoor, 2009).

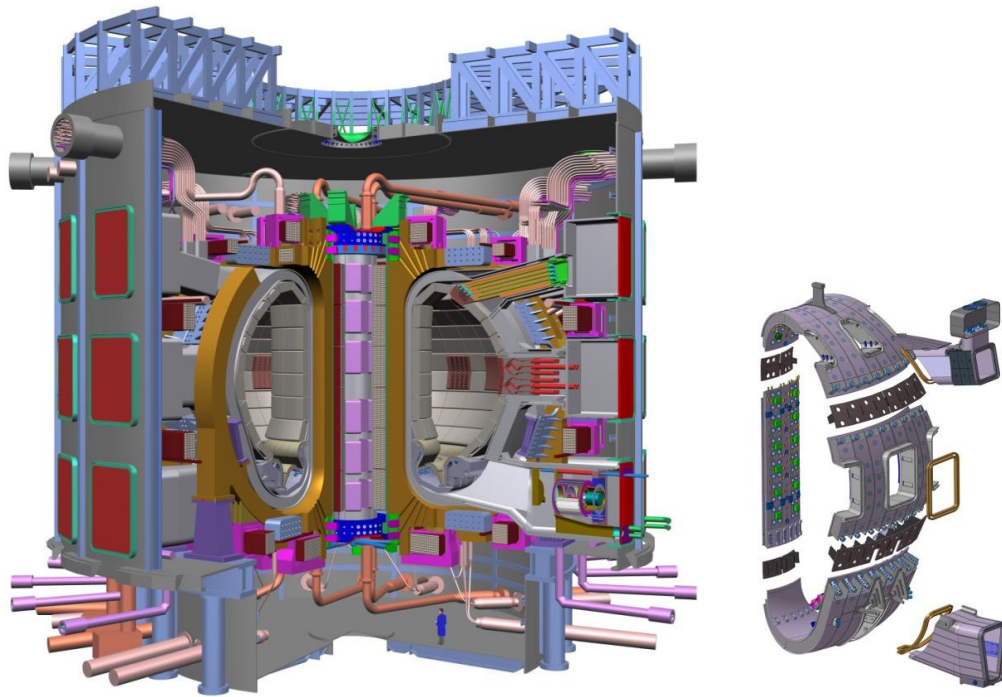


Figure 1.1: International Thermonuclear Experimental Reactor (ITER).

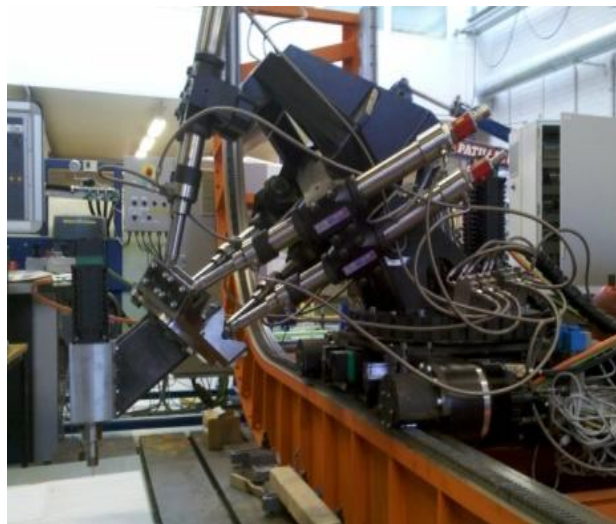


Figure 1.2: Hybrid robot and the construction of the parallel robot.



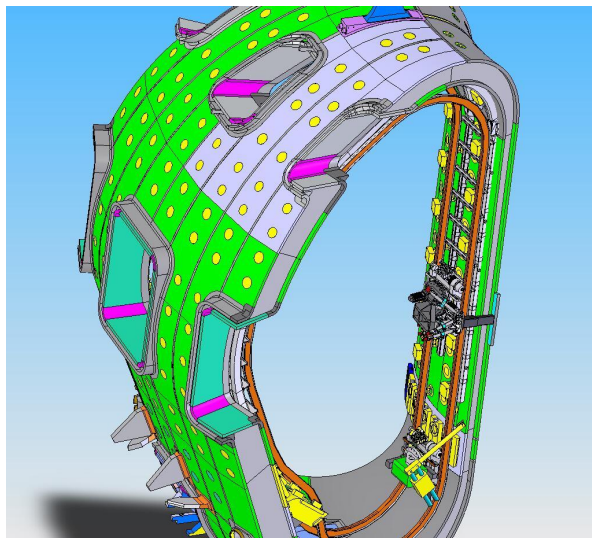


Figure 1.3: The hybrid robot movement inside one section of the Vacuum Vessel of (ITER).

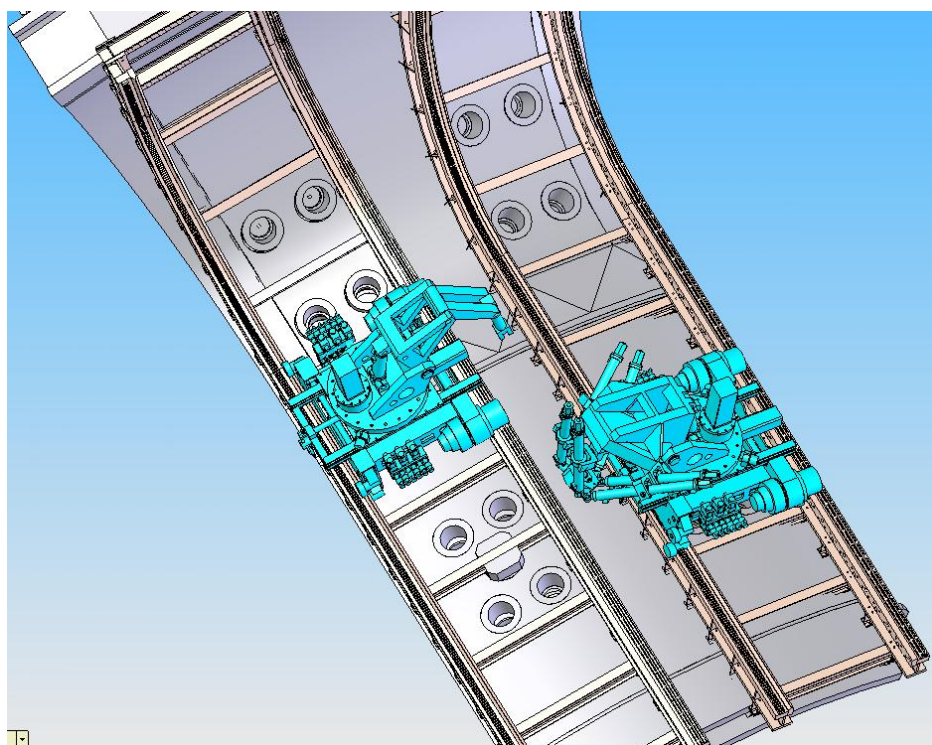


Figure 1.4: The hybrid robot movement inside one quarter section of the Vacuum Vessel of (ITER).

### 1.3 Flexible multibody dynamics

Reducing the mass of the robot manipulators offers many advantages: reduced material costs, reduced power consumption, the possibility of using smaller actuators, and a higher payload-to-robot weight ratio. Despite these advantages, the lighter weight robot is more flexible, which makes it more difficult to control. To achieve good machining surface quality, the tracking of the end effector must be accurate, and an accurate model for the more flexible robot must be constructed.

Because of the reduced structural stiffness, the inertial forces generated from acceleration will lead to exaggerated and unwanted displacements and vibration. These undesired motions will degrade system performance significantly by decreasing positioning accuracy and increasing settling times. Even worse, they will result in system instability. Therefore, for accurate control in high performance systems, the flexibility of the mechanical components must be taken into account (Wang *et al.*, 2010). A hybrid redundant robot with flexible piston rods is studied here.

Several researchers have studied open-loop mechanisms such as flexible serial robots. For instance, Sunada and Dubowsky (1983) used constraint modes and fixed-interface normal modes to reduce the nodal DOFs in a flexible serial robot component to modal DOFs. Nominal motion was obtained from a dynamic independent analysis of a rigid body model. Next, they generated linear structural equations of motion for the deformation variables with time-varying coefficient matrices. The application of their approach is limited, because it ignores coupling between gross motion and small elastic deformation.

Accounting for structural flexibility in the dynamic modeling of parallel mechanisms, characterized by multiple spatial closed-loop chains, has not been studied extensively. Traditionally, in the rigid link case, parallel platforms are readily modeled with independent coordinates with inverse kinematics models, while parallel platforms with flexible links are more difficult to model because of the unavailability of closed-form solutions to the inverse kinematic model. Consequently, dynamic coupling effects among the various kinematic chains of the mechanisms, and coupling between rigid body motion and flexible motion are generally more complex to model than in the serial mechanism case (Wang and Mills, 2006). Setting up the mathematical model for a general flexible parallel manipulator is challenging. The nominal motion of the manipulator involves variable geometries resulting in varying system parameters. So, the equations of motion are usually configuration dependent and need to be computed for each configuration of the manipulator (Zhao *et al.*, 2011).

Recently, in line with growing interest in the use of parallel kinematics machine tools, researchers have been examining the dynamics of flexible parallel robots, which have multiple closed-loop chains. Fattah *et al.* (1995) used the finite element method (FEM) and the Euler-Lagrange formulation to model the flexible linkage of a parallel manipulator with three degrees of freedom assuming that the influence of flexible

---

motion on the rigid motion is negligible. With the piston being modeled as a mass-spring-damper, a set of twelve Lagrange equations for the flexible Stewart manipulator was derived by Lee and Geng (1993) using a tensor representation. Zhaocai and Yueqing (2008) studied the flexible planar parallel robot. This study was limited due to its use of the so-called driving force method, which is approximate. Wiens and Hardage (2006) presented a methodology and experimental study for modeling the structural dynamics of a parallel kinematic machine. They replaced the constraints between the links and moving plate with boundary conditions.

Among studies tackling the subject of the vibration of a hexapod parallel robot, considerable effort has been dedicated to application of the finite element method. Without considering the effects of nominal motion, Zhou *et al.* (2006) provided the stationary vibration model of the flexible 3PRS parallel kinematic machine where the links were modeled as finite elements and the joint as virtual spring/dampers. Then, a nonstationary model of the same parallel kinematic machine was developed using the elasto-dynamics method by Zhou *et al.* (2007). Modeling of the 8-PSS flexible redundant parallel manipulator was investigated by Zhao *et al.* (2011), who assumed the rigid dynamic model is presented first. Then, the actuating forces could be achieved. Finally, the kineto-elastodynamic model of the manipulator was developed using the finite element method and substructure synthesis technique. In structural dynamics, constraint equations are linear in the elastic coordinates and can be applied using a Boolean matrix that has constant elements. Unfortunately, this approach cannot be adopted in the dynamics of elastic mechanical systems because of the inertial properties, the eigenspectra vary with time, and because of the nonlinearities in the constraint equations (Shabana, 2005).

Carbone (2011) used the lumped mass approach to analysis flexible parallel robot. In his approach, he assumed that the compliance of each component of a multibody robot system can be modelled with lumped parameters by using linear and torsional springs. It is noteworthy that he assumed that the stiffness matrix is kinematic configuration dependent, i.e., the stiffness matrix is a function of time for a given end-effector trajectory.

Zhang *et al.* (2007) studied the effects of elastic deformation on the rigid body motions of 3PRR flexible intermediate links based on the Assumed Mode Method (AMM). However, gravitational potential energy is not included in their study, and they neglected the Lagrange multiplier when reducing the equations of motion.

Finite element analysis is usually used to obtain the static and dynamic responses of a system loaded by known forces. However, the AMM is used not only to obtain the dynamic responses of the system, but also to control unwanted vibration and end effector motion. Compared to FEA, the drawbacks of the AMM are as follows (Vakil *et al.*, 2008): (i) The mode shapes employed in the AMM are an approximation of the real mode shapes of the system. (ii) The nonlinear strain energy terms, which lead to effects such as stress stiffening, cannot be addressed properly. (iii) The AMM does not lead to

a realistic approximation of the dynamic model for a flexible rod with a varying cross-section, such as a tapered beam. These drawbacks result in errors when the AMM is used to model a flexible rod. Furthermore, when using the AMM to model flexibility as the number of links increases, the calculation of the Lagrangian equation and evaluation of the derivatives become more lengthy and complex, and thus more prone to error (Vakil *et al.*, 2008).

Recently, more attention has been given to studying the flexibility of mechanisms using floating frame of reference techniques (FFRF). With FFRFs, the equations of motion are expressed in terms of a coupled set of reference and elastic coordinates. The reference coordinates define body location and orientation, while the elastic coordinates define body deformation with respect to its reference. The elastic coordinates can be determined using the finite element method or the experimental identification technique (Wang *et al.*, 2010). In the FFRF, deformations are usually expressed using methods based on the FEM approach. Thus, the motion of each point on the flexible body is regarded as the superposition of the rigid body motions in the global coordinate system and local flexible deformations in the floating frame (Wang and Mills, 2004). To decrease the number of coordinates related to flexibility, Shabana and Wehage (1983) proposed the use of component mode synthesis (CMS). In CMS, a set of nodal coordinates from an FE model can be replaced by a smaller number of modal coordinates. As a result, the system size and computational time are considerably reduced. In addition, since the high frequency modes are eliminated, larger time steps can be used in the simulation. Yoo and Haug (1986) introduced the use of static correction modes to account for local deformation due to joint constraints and force components.

Wang and Mills (2004) introduced a CMS procedure for developing a dynamic model of a flexible link planar parallel platform with PZT transducers. They used the result of the rigid body simulation of actuation forces and joint constraint forces as inputs for the flexible multibody simulation.

The formulation of kinematic joints composed of simple basic constraints in the case of systems of rigid bodies has been formulated by Haug (1989). Bay and Han (2000) modeled joint constraints using virtual bodies. In their approach, the constraints were developed between massless rigid bodies. However, adding virtual bodies increases computational time. Shabana (2005) established an approach based on intermediate body fixed joint coordinate systems that are rigidly attached to joint definition points. In this approach, by assuming the joint axis can be described as a rigid line, the joint coordinate systems are used to derive basic constraint equations including sliding joints.

Manipulators with prismatic joints are also used widely in industry. However, research on this type of manipulator has not received the attention it deserves. Hwang and Haug (1990) illustrated basic constraint types used with translational joint models, which account for the deformation of the axis line. They used the FFRF approach accounting

for multiple contact points, whereas the numerical results are only shown in the case of a single contact point.

Korkealaakso *et al.* (2009) presented an approach for the modeling of joint constraints for flexible multibody systems using three basic constraint primitives. The terms of the Jacobian matrix and the terms related to second time differentials of constraint equations are explicitly presented. One of the examples they studied was the flexible slider mechanism. However, the cylinder of the flexible slider mechanism is fixed to the framework using a bracket joint. It cannot move while the rod is sliding inside the cylinder.

#### **1.4 ANFIS and fuzzy tuning of a PID controller for trajectory tracking of a flexible hydraulically driven parallel robot machine**

Flexible robot manipulators exhibit many advantages over rigid robots: they require lighter material, consume less power, require smaller actuators, and have a higher payload-to-robot weight ratio. Despite these advantages, the modeling and control of flexible manipulators is more difficult than controlling rigid manipulators (Al-saedi *et al.*, 2012). Thus, in machining, to achieve better end effector trajectory tracking accuracy for surface quality, complex and more accurate control of the actuators for the flexible link has to be created. To minimize the tracking errors, dynamic forces need to be compensated by the controller.

However, the closed mechanical chains make the dynamics of the parallel manipulators highly complex and their dynamic models highly nonlinear even though some of the parameters, such as masses, can be determined; other parameters such as centripetal and Coriolis forces, variation in the location of the center of gravity, modeling errors and disturbances such as machining forces, cannot be determined exactly. As a result, many of the control methods are not sufficiently efficient. The difficulty in the control of the parallel robot lies in the need for the simultaneous control of the trajectories of its six actuators. This also means that there will be a limitation to the error permitted for each actuator (Indrawanta and Santoso, 2009).

In recent years, significant efforts have been made by researchers across the world to control parallel robots. Various approaches have been proposed; for example, Hopkins and Williams (2002) used the PID control method and Indrawanta and Santoso (2009) implemented the sliding mode control method. The fuzzy logic method was also used to control parallel robots; for example, Yongsheng *et al.* (2010) formulated the enhanced fuzzy sliding mode controller for a 3-DOF parallel manipulator. The method of neural networks was also attractive and used by researchers for control actuated parallel robots, e.g. by Akbas (2008) and Li *et al.* (2008). Seifried *et al.* (2011) analysed the feed forward control for flexible multibody system using flexible model inversion. Unfortunately, the feed forward control method characterized by phase lagging and the

disturbance variables must be measured on-line, in many applications, this is not feasible. Furthermore, finding the flexible model inversion is not simply for complex mechanism like the flexible parallel robot. Wu *et al.* (2014) used the feed forward method plus the feedback method together to eliminate the disadvantages of each other for chatter suppression in robot machines.

The PID controllers can be described based on their robust performance in a wide range of operating conditions and their functional simplicity, which allows operation in a simple, straightforward manner. However, the highly nonlinear nature of the parallel robot means that a PID controller can perform well only in a particular operating range. The PID controllers can basically be divided into two categories. In the first category, the PID parameters are fixed in the entire control process after they have been tuned or adjusted in a certain optimal way. However, it is difficult to obtain satisfactory performance when the control system is highly nonlinear and heavily coupled. The second category is self-tuning to the first type. The structure is similar to the first type, but the parameters can be manipulated online based on parameter estimation in order to make the system more adaptive and robust. However, conventional PID controllers are still widely used in robot control, when the system parameters such as mass and inertia are not accurately measured. If they vary under different operating conditions, the conventional PID controllers may not achieve satisfactory performance (Tian, 2004). In order to obtain global results, it is necessary to re-tune the PID controller when the operating range is changed, and different techniques from nonlinear control theory are required (Ravi *et al.*, 2011).

Robotic machines, unlike humans, lack the ability to solve problems using imprecise information requiring restrictive assumptions for the plant model and for the control to be designed (e.g. linearity). To emulate this ability, fuzzy logic and fuzzy sets are introduced (Ravi *et al.*, 2011). The fuzzy controller can be designed without knowing the mathematical model of the system, and instead by mimicking human operators' thinking processes through linguistic rules. These rules reflect human experience or knowledge about how to control the dynamic system. In addition, unlike PIDs, fuzzy controllers are nonlinear and adaptive in nature, thereby giving a robust performance under parameter variations and a load disturbance effect (Tian, 2004). Fuzzy logic control systems, which have the capability of transforming linguistic information and expert knowledge into control signals (Melba Mary *et al.*, 2007), are currently being used in a wide variety of complex and nonlinear processes in engineering applications.

Although fuzzy logic systems, which can reason with imprecise information, are good at explaining their decisions, they cannot automatically acquire the rules used to make those decisions (Aldair, 2010). On the other hand, artificial networks are good at recognizing patterns and have the ability to train the parameters of a control system, but they are not good at explaining how they reach their decisions. These limitations in both systems have stimulated the creation of intelligent hybrid systems (such as neuro-fuzzy systems) where the two techniques are combined in such a manner that the limitations of the individual techniques are overcome. The neuro-adaptive learning techniques

---

provide a method for the fuzzy modelling procedure to acquire information about a data set. This technique gives the fuzzy logic capability to compute the membership function parameters that effectively allow the associated fuzzy inference system to track the given input and output data (Aldair, 2010).

In order to achieve accurate trajectory tracking and good control performance, a number of control schemes have been developed, amongst these, the adaptive neuro-fuzzy inference system (ANFIS). The ANFIS is a fuzzy inference system implemented in the framework of adaptive networks. By using a hybrid learning procedure, the ANFIS can construct an input-output mapping based on both human knowledge (in the form of fuzzy **if-then** rules) and stipulated input-output data pairs. The hybrid learning algorithm identifies the membership function parameters of single-output, Sugeno type fuzzy inference systems (FIS) (Adhyaru *et al.*, 2010). A combination of least mean squares (LMS) and backpropagation gradient descent methods is used for training FIS membership function parameters to model a given set of input/output data. The parameters associated with the membership functions change through the learning process. The training process stops whenever the designated epoch number is reached or the training error goal is achieved. Adhyaru *et al.* (2010), Bachir and Zoubir (2012), and Ngo *et al.* (2012) used the ANFIS to control a serial robot by training the input/output PID control data. Under conditions of uncertainty, the model parameters of parallel manipulators can be identified by using the ANFIS control algorithm. Such an algorithm can be performed in a real time control application (Aldair, 2010).

## 1.5 Special Euclidean group for dynamics and control

In the floating frame of reference formulation (FFRF) Shabana (2005) employs two sets of generalized coordinates; absolute reference and local elastic coordinates. Thus, the motion of each point on the flexible body is regarded as the superposition of the rigid body motions in the global coordinate system and local flexible deformations in the floating frame (Wang and Mills, 2004). As the result of using the floating frame (body coordinate system), this formulation leads to geometric nonlinearities due to the nature of the generalized coordinates used to capture the change of orientation of the body coordinate system. Such geometric nonlinearities make the formulation of most joint constraints highly nonlinear and complex. Furthermore, the use of the FFRF that often employs modal reduction techniques makes the formulation of some joints such as the sliding or prismatic joints between two flexible bodies very difficult (Hwang and Haug, 1990). The difficulties associated with the formulation of the prismatic joints between two flexible bodies are the result of the change in boundary conditions due to the relative motion of the two bodies connected by this joint. As the result of the continuous changes in the boundary conditions, one set of linear vibration modes cannot be used to accurately represent the dynamics of the prismatic joint (Sugiyama *et al.*, 2003).

The finite element approach of multibody systems has been significantly studied, for instance by Geradin and Cardona (2001). Nodal values, measuring positions and orientations with respect to a global frame are introduced to describe the configuration of rigid and flexible multibody systems. Then inertia properties are assigned to some nodes, and kinematic constraints are used to model the physical links between the nodes of the system. Based on the finite element concept, this approach allows one to write systematically the equations of motion by collecting generic expressions which are slightly tuned according to a system part of interest. This results in second order differential-algebraic equations for which a suitable time integration solver has been used.

The nodal approach has been brought to a new level by exploiting the underlying Lie group structure of the configuration space (Brüls *et al.*, 2011). The equations of motion are then formulated as a set of differential-algebraic equations on a Lie group, without the need to refer to a particular set of coordinates. These equations are then solved using recently developed Lie group time integration schemes (Brüls *et al.*, 2012; Brüls and Cardona, 2010). A key aspect of the abstract approach is that it systematically avoids any parameterization of the total motion, but it naturally leads to local parameterizations. In particular, this framework reduces the non-linearity of the equations of motion and leads to a naturally singularity-free formulation.

The description of rigid and flexible bodies in this research relies on kinematic assumptions on the position of their material points by introducing rotation variables (Geradin and Cardona, 2001). Several methods have been explored to represent rotation variables such as the parameterization of rotation (Geradin and Cardona, 2001) or the Lie group methods (Simo, 1985; Brüls *et al.*, 2012; Brüls *et al.*, 2011; Brüls and Cardona, 2010). In this research examines a Lie group method which is based on the differential geometry of the nonlinear configuration space. The Lie group  $\mathbb{R}^3 \times SO(3)$  has been widely used for rigid formulations. This research considers the Lie group  $SE(3)$  which has been applied to rigid body problems, particularly in robotic applications (Murray *et al.*, 1994). Compared to  $\mathbb{R}^3 \times SO(3)$ ,  $SE(3)$  implies a stronger coupling between the position and rotation variables. The mathematics of this group is described by Murray *et al.* (1994) and some practical advantages have already been pointed out for the formulation of rigid multibody systems using absolute coordinates (Brüls and Cardona, 2010).

In this research, a straight beam finite element formulation is used to describe flexible bodies. In the finite element context, a spatial discretization of the beam is introduced by a nonlinear interpolation method of nodal values and the discrete problem is then derived from a variation principle. Geradin and Cardona (2001), Brüls *et al.* (2012) and Crisfield and Jelenic (1999) maintain that the positions and the rotations are interpolated separately since they are considered to be fundamentally independent. In contrast, the  $SE(3)$  Lie group framework used in this research introduces a natural coupling of the position and rotation variables thanks to an exponential interpolation method which



---

exhibits important theoretical and numerical advantages (Sonneville *et al.*, 2014). The equations of motion of the mechanical system take the form of second-order ordinary differential equations on the Lie group. The equations are then solved using the generalized- $\alpha$  Lie group integrators developed by Brüls *et al.* (2012), Brüls *et al.* (2011), and Brüls and Cardona (2010). The proposed approach relies on a rigorous mathematical frame based on the Lie group theory. Since a Lie group solver is used, it is remarkable that the dynamic equation is formulated in a parameterization-free way and that no parameterization of the nodal variables needs to be introduced. The theory naturally leads to a frame-invariant, compact and elegant formulation of the beam finite element (Sonneville *et al.*, 2014).

The formulation of kinematic joints composed of simple basic constraints in the case of systems of rigid bodies has been formulated by Haug (1989). Bay and Han (2000) modeled joint constraints using virtual bodies. In their approach, the constraints were developed between massless rigid bodies. However, adding virtual bodies increases the computational time. Shabana (2005) established an approach based on intermediate body fixed joint coordinate systems that are rigidly attached to joint definition points. Manipulators with prismatic joints are also used widely in industry. However, research on this type of manipulator has not received the attention it deserves. Hwang and Haug (1990) illustrated basic constraint types used with translational joint models, which account for the deformation of the axis line. They used the FFRF approach accounting for multiple contact points, whereas the numerical results are only shown in the case of a single contact point. Korkealaakso *et al.* (2009) presented an approach for the modeling of joint constraints for flexible multibody systems using three basic constraint primitives. One of the examples they studied was the flexible slider mechanism. However, the cylinder of the flexible slider mechanism is fixed to the framework using a bracket joint. It cannot move while the rod is sliding inside the cylinder. The constraint equation of the sliding joint, which allows mass to move along a flexible cable, was proposed using the Absolute Nodal Coordinate Formulation (ANCF) by Sugiyama and Han (2000). This method assumed the cable would have only one beam element. Therefore, if a cable is modeled with two or more beam elements, discontinuity at the nodal points makes this method difficult to employ in modeling the sliding joint. Lee *et al.* (2008) state that the three-dimensional sliding joint was developed using the ANCF for large deformable beams consisting of several finite elements, and the sliding joint crosses a node between the beam elements. This may result in problems of numerical discontinuity; therefore, they overcome this issue by reconstructing the Jacobian matrix when the sliding joint moves a node (Lee *et al.*, 2008).

## 1.6 Objectives of the study

The main objective of the study is to develop a multibody dynamic simulation of a serial-parallel hybrid robot with the interactions of an intelligent hydraulic control

system to reduce vibration. This improves the accuracy and performance of the end effector during the required tasks, such as machining and welding.

The main objective of the study is divided into three goals. The first goal is to analyze a hybrid robot coordinate system. The rods inside each rigid cylinder are considered flexible. By coupling the finite element method, multibody dynamics, the floating frame of reference formulation and the Craig-Bampton method to the deformable rods and to reduce the size of the system the essential dynamic behavior of the entire structure can be modeled with a relatively small number of degrees of freedom (DOF) along with the flexible body description. Constraint modelling is described where the translational joint between the sliding flexible rod and the rigid cylinder is modelled as two sets of constraint vectors to obtain a proper kinematic model of the joint. The dynamic equations of the six closed loop parallel robot are studied, as well as the hydraulic forces inside each cylinder and the design of the hydraulic control system and control law. Later, the dynamics of the serial robot part are analyzed using the reaction forces at the universal joints. Finally, robot parameters, an ADAMS<sup>TM</sup> model of the parallel robot built to verify the validity of the simulation, and simulation results are presented.

For the above-mentioned dynamic model of the hybrid serial-parallel robot, the second goal is the application of Fuzzy logic and ANFIS, which are included in the Artificial Intelligent (AI) techniques to control a hydraulically driven parallel robot by tuning the PID gains. A hydraulic control system is designed and control law is used. Consequently, the fuzzy-PD self-tuning of the gains ( $K_p$  and  $K_d$ ) is designed for each hydraulic cylinder controller. The ANFIS-PD self-tuning control is also designed for the same reason. In addition, the dynamics and control of the serial part are studied using the equilibrium of reactions at the universal joints. Finally, using the real robot parameters, simulation studies were conducted to demonstrate the performance of the proposed controllers.

The third goal, again, for the same reason, is to introduce a hydraulically driven parallel mechanism of flexible rods slide inside each rigid cylinder, the Special Euclidean group SE(3) method. Constraints modeling which includes the kinematics of joint description and constraint equations is presented. The flexibility of a rod of a robot arm is described using the nonlinear interpolation method with an exponential map, which introduces a natural coupling between the position and rotation variables. The internal and external forces are derived from variational principles. The flexible slider constraint is formulated using a Lie group and used for modeling a flexible rod sliding inside a cylinder. The hydraulic forces inside each cylinder as well as the design of a hydraulic control system and PID control law are studied. The equations of motion of the six closed loop parallel robot take the form of a set of differential–algebraic equations on a Lie group, which is solved using a Lie group time integration scheme. The method relies on a local description of motions, so that it provides a singularity-free formulation. No parameterization of the nodal variables needs to be introduced, and the method exhibits important advantages regarding numerical implementation. Finally,

robot parameters, an ADAMS<sup>TM</sup> model of the parallel robot built to verify the validity of the simulation, and simulation results are presented, respectively.

The computational environment MATLAB<sup>TM</sup> 8.0.0.783 was the tool selected for the multibody simulation implementation in all of the goals.

## 1.7 Outline of the thesis

The following section presents the work carried out in this study.

In **chapter 2**, the flexibility of the bodies is described using the floating frame of reference method. The dynamic model of the system of six closed loop mechanisms was assembled using the constrained Lagrange equations and the Lagrange multiplier method. The reaction forces between the parallel and serial parts were used to study the dynamics of the serial robot. A hydraulic control system of a linearized PID was implemented independently to control the hydraulic cylinders of the parallel and serial robots. The results of the simulations demonstrating the behavior of the robot machine are presented.

**Chapter 3** investigates the intelligent control of a hydraulically driven parallel robot part based on the dynamic model, and two control schemes: (1) a fuzzy-PID self-tuning controller and (2) ANFIS-PID self-tuning of the gains of the PID controller, which are implemented independently to control each hydraulic cylinder of the parallel robot based on rod length predictions. Subsequently, the serial component of the hybrid robot can be analyzed using the equilibrium of reaction forces at the universal joint connections of the hexa-element. Finally, simulated results that demonstrate the robot behaviors are presented.

**Chapter 4** presents the dynamics of a hydraulically driven parallel robot. The rods inside each rigid cylinder are considered flexible. The fundamentals of the Special Euclidean group  $SE(3)$  are introduced. Constraints modeling which includes the kinematics of a joint description and constraint equations is presented. The flexibility of a rod of a robot arm is described using the nonlinear interpolation method with an exponential map. The internal and external forces are derived from variational principles. The flexible slider constraint is formulated using a Lie group and used for modeling a flexible rod sliding inside a cylinder. The hydraulic forces inside each cylinder as well as the design of a hydraulic control system and control law are studied. The equations of motion of the six closed loop parallel robot take the form of a set of differential-algebraic equations on a Lie group, which is solved using a Lie group time integration scheme. Finally, robot parameters, an ADAMS<sup>TM</sup> model of the parallel robot built to verify the validity of the simulation, and simulation results are presented.

**Chapter 5** provides the conclusions and recommendations for future research.

## 1.8 Scientific contributions and publications

The main scientific contributions of this thesis are the following

- The thesis presents the dynamic modeling of the 6-UPS parallel robot with flexible rods sliding into cylinders using the floating frame of reference method.
- The thesis analyzes the dynamics and control of the serial robot part of the hybrid robot using the reaction forces at the connecting universal joints.
- The thesis presents two methods of tuning the gains of a PID controller – the fuzzy-PID and ANFIS-PID – and demonstrates that the ANFIS-PID is the best.
- The thesis presents the dynamic modeling of the 6-UPS parallel robot with flexible rods sliding into cylinders using the Special Euclidean Group  $SE(3)$ .

### Referred scientific journals

- Mazin I. Al-saedi , Huapeng Wu, Heikki Handroos, and Tuomas Rantalainen. Flexible Multibody Dynamics Modelling and Control of a Hydraulically Driven Hybrid Redundant Robot Machine, *accepted to be published in the Journal of Robotica*, 2014.
- Mazin I. Al-saedi, Huapeng Wu, Heikki Handroos,: ANFIS and Fuzzy Tuning of PID Controller for Trajectory Tracking of a Flexible Hydraulically Driven Parallel Robot Machine, *Journal of Automation and Control Engineering*, ISSN:2301-3702, Vol.1, No.2, March, 2013, pp. 70-77.
- Mazin I. Al-saedi, Huapeng Wu, and Heikki Handroos, Intelligent controller of a flexible hybrid robot machine for ITER assembly and maintenance. *Journal of Fusion Engineering (paper accepted to be published in the Journal of Fusion Engineering in press, 2014)*.
- Huapeng Wu, Yongbo Wang, Ming Li, Mazin Al-saedi, Heikki Handroos, Chatter suppression methods of robot machines for ITER Vacuum Vessel assembly and maintenance. *Journal of Fusion Engineering (paper accepted to be published in the Journal of Fusion Engineering in press, 2014)*.

### International conferences with review process:

- Huapeng Wu, Yongbo Wang, Ming Li, Mazin Al-saedi, and Heikki Handroos, Chatter suppression methods of robot machines for ITER Vacuum Vessel assembly and maintenance. *Proceedings of the 11<sup>th</sup> International Symposium on Fusion Nuclear Technology*, 16-20 September 2013. Barcelona, Spain.
- Mazin I. Al-saedi, Huapeng Wu, and Heikki Handroos Intelligent controller of a flexible hybrid robot machine for ITER assembly and maintenance. *Proceedings*

of the 11<sup>th</sup> International Symposium on Fusion Nuclear Technology 16-20 September 2013, Barcelona, Spain.

- Mazin I. Al-saedi, Huapeng Wu, and Heikki Handroos, ANFIS and Fuzzy Tuning of PID Controller for Trajectory Tracking of a Flexible Hydraulically Driven Parallel Robot Machine. *Proceedings of the ICCAE 2013, Jan. 12-13, 2013, Brussels, Belgium.*
- Mazin I. Al-saedi, Huapeng Wu, and Heikki Handroos, Flexible Multibody Dynamics and Control of A Novel Hydraulically Driven Hybrid Redundant Robot Machine, *the 2<sup>nd</sup> International conference on Applied Robotics for the Power Industry*, ETH Zurich, Switzerland, September 11-13, 2012, pp. 159-164.
- Mazin I. Al-saedi, Heikki Handroos, and Huapeng Wu, *Multibody Dynamics and Control of A Novel Hydraulically Driven Hybrid Redundant Robot Machine*, *the 5<sup>th</sup> (ICARA 2011) conference of IEEE in Wellington, New Zealand* on 7-9 Dec. 2011, pp. 133-138.



## **2 Flexible multibody dynamics using the FFRF technique and PID control**

### **2.1 Strain Analysis in multibody dynamics**

Generally, the deformations and corresponding strains of a body within a flexible multibody system can be studied using four approaches:

- 1- The nonlinear finite element approach (Shabana, (2005), De Jalon and Bayo, (1994)).
- 2- The linear theory of elastodynamics (Shabana, (2005)).
- 3- The lumped mass approach (Shabana, (1996)).
- 4- The floating frame of reference formulation FFRF (Shabana, (2005)).

In the first approach, such as the absolute nodal coordinate formulation ANCF (Shabana, (2005)), and is basically devoted for large deformation analysis of flexible multibody system. In the formulation, slopes and positions are used as the nodal coordinates instead of infinitesimal or finite rotations. The advantages of using the ANCF in the dynamic analysis of flexible multibody systems are its simplicity in describing some of the joint constraints and formulating the generalized forces. In addition this formulation leads to constant mass matrix which simplifies the nonlinear equations of motion. However, for a body with a complex geometry, where the discretization results in a large number of nodal degrees of freedom, the method may be considered computationally expensive (De Jalon and Bayo, (1994)).

In the second approach, the response of the flexible body is calculated by uncoupling rigid body motion and elastic deformation. To this end, the flexible multibody system is first assumed to be a collection of rigid bodies. The final response of the system can be obtained by superimposing the deformation on the rigid motion of the body. However, in this approach, the deformation of the body is assumed to be small and has a negligible effect on the rigid body motion. Accordingly, the inertia terms in the reference equations are assumed to be independent of the elastic deformation. In this approach the deformation and large body motion are not coupled, possibly leading to an unnatural solution (Shabana, (2005)).

In the lumped mass approach, the flexible body is idealized into several rigid body mass elements. Spring elements are placed between these masses to account for flexibility. The stiffness of each spring located between each mass element can be usually obtained using the finite element method. In the lumped mass approach, the use of deformation modes (mode shape functions) to study the flexibility of the body is not possible. Therefore, this approach can be considered to be computationally expensive for a flexible body with complicated geometry.

The approach based on the floating frame of reference formulation FFRF can be used in the analysis of flexible bodies that undergo large reference displacements; rotational and translational, with small deformations (Shabana, (2005)). The configuration of the flexible body in the FFRF is described using a mixed set of absolute reference and local deformation coordinates. In this approach, classical linear finite element is embedded in the multibody formalism. Unlike the first and third approaches, the size of the problem can be reduced in the FFRF by using deformation mode shapes. In contrast to the approach based on the linear theory of elastodynamics, the rigid body motion and deformations are coupled in the FFRF, which makes it suitable for general applications.

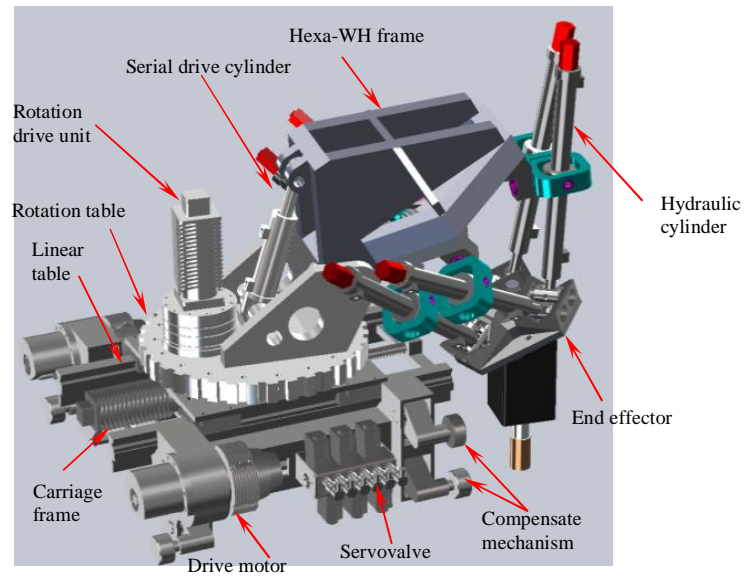
## **2.2 Coordinate System of a Hybrid Robot**

### **2.2.1 Description a hybrid robot**

The hybrid robot has ten degrees of freedom (Figure 2.1(a) and (b)), and it consists of two relatively independent sub-structures. The carriage provides four degrees of freedom: rotation, linear motion, tilt rotation, and tracking motion that enlarges the workspace and offers high mobility. The 6-UPS hexa-parallel mechanism, driven by six hydraulic cylinders, contributes six degrees of freedom to the end effector. Consequently, the robot is a hybrid redundant manipulator with four degrees of freedom provided by the serial kinematic axis. During the process of machining, however, the carriage will be locked on the track rail, and the other three actuators in the serial mechanism will be in a fixed position. Therefore, only the parallel mechanism contributes motion to the machine tool. The 10-DOF prototype is equipped with water hydraulic drives since large quantities of oil are not allowed in ITER.



(a) Solid model



(b) Wire frame

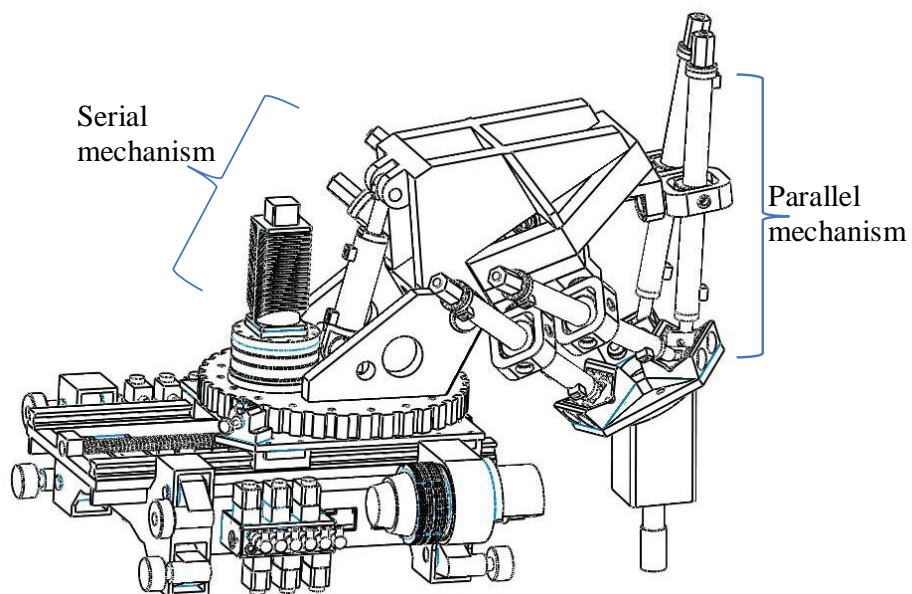


Figure 2.1: Hybrid robot construction (serial 6-UPS parallel) robot (a) Solid model (b) Wire frame.

2.2.2 Inverse kinematics of 6-UPS parallel robot

The inverse kinematics for the carriage is defined as to find the values of four actuators (two translations and two rotations) for a given position and orientation of hexa-frame defined as  $P_4$  with respect to frame  $\{O\}$ . The principle of the carriage mechanism is described in Figure 2.2(a).

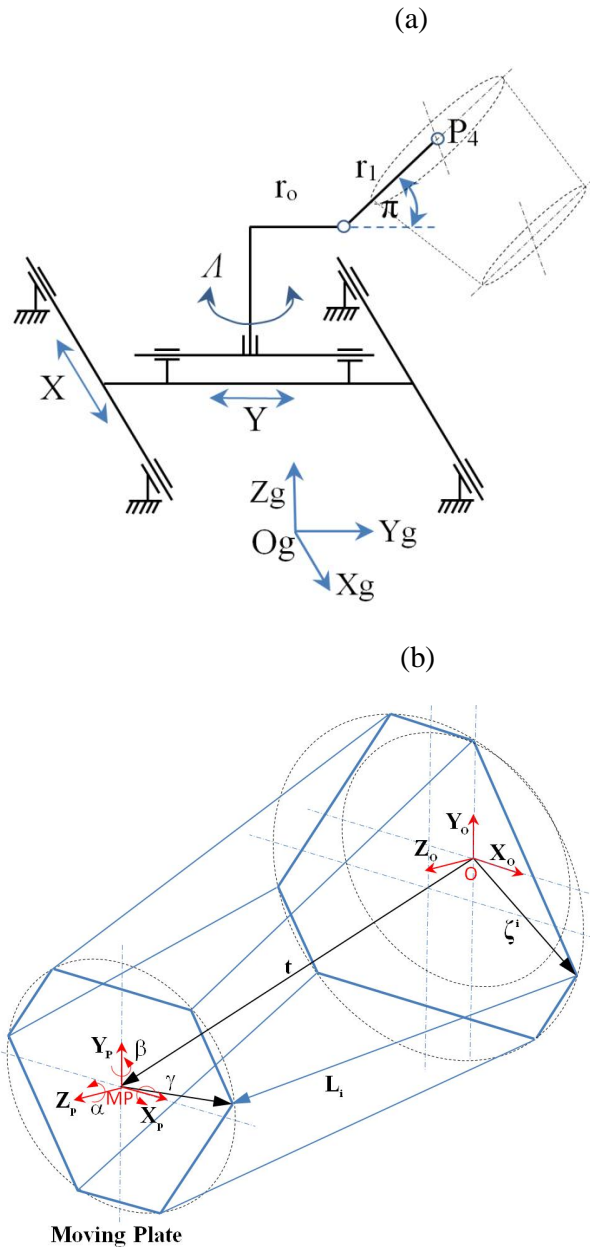


Figure 2.2: Kinematic analysis of the (a) serial mechanism and (b) 6-UPS parallel mechanism.

The rotation angle  $\pi$  values are limited into a few constant values, i.e.,  $0^\circ$ ,  $\pm 90^\circ$  and  $180^\circ$ . Fixing  $\pi$ , for a given position  $P_4(x,y,z)$  of the center of hexa-frame, we have

$$X + (r_0 + r_1 \cos \pi) \cos \Lambda = x, \quad (2.1)$$

$$Y + (r_0 + r_1 \cos \pi) \sin \Lambda = y, \quad (2.2)$$

$$r_1 \sin \pi = z, \quad (2.3)$$

where the variables:  $r_1$ ,  $r_0$ ,  $X$ ,  $Y$ , and  $\Lambda$  can be seen in Figure 2.2(a). Then

$$\pi = \arcsin(z/r_1), \quad (2.4)$$

$$X = x - (r_0 + r_1 \cos \pi) \cos \Lambda, \quad (2.5)$$

$$Y = y - (r_0 + r_1 \cos \pi) \sin \Lambda, \quad (2.6)$$

The inverse kinematics for a 6-UPS parallel robot is defined as finding the strokes for each cylinder for a given position and orientation of the end effector with respect to the hexa-frame (fixed plate). Here, O in Figures 2.2(b) coincides with  $P_4$  on the carriage side in Figures 2.2(a). Figures 2.2(b) shows the vector analysis of the 6-UPS parallel mechanism while Figures 2.3 shows the construction of each arm. Thus a vector loop equation for each leg can be written as

$$\bar{\mathbf{L}}_i = \mathbf{t} + \mathbf{R}\bar{\mathbf{r}}'_i - \boldsymbol{\zeta}_i \quad i = 1, 2, \dots, 6 \quad (2.7)$$

where  $\mathbf{R}$  is a rotation matrix defined by using Euler angles as

$$\mathbf{R} = \begin{bmatrix} c\alpha c\beta & c\alpha s\beta s\gamma - s\alpha c\gamma & c\alpha s\beta c\gamma + s\alpha s\gamma \\ s\alpha c\beta & s\alpha s\beta s\gamma + c\alpha c\gamma & s\alpha s\beta c\gamma - c\alpha s\gamma \\ -s\beta & c\beta s\gamma & c\beta c\gamma \end{bmatrix} \quad (2.8)$$

$\boldsymbol{\zeta}_i$  is the vector joint of the  $i^{\text{th}}$  cylinder on the fixed plate with respect to frame O, and  $\bar{\mathbf{r}}'_i$  is the vector of the joint of the  $i^{\text{th}}$  cylinder on the end effector with respect to frame MP.

Then, the length of each leg can be determined, with a Cartesian coordinate vector  $\mathbf{t}$  ( $x$ ,  $y$ ,  $z$ ) defined with respect to frame MP, by the Euclidean norm

$$l_i = \|\bar{\mathbf{L}}_i\| = \sqrt{(\mathbf{t} + \mathbf{R}\bar{\mathbf{r}}'_i - \boldsymbol{\zeta}_i)(\mathbf{t} + \mathbf{R}\bar{\mathbf{r}}'_i - \boldsymbol{\zeta}_i)} \quad (2.9)$$

Equations (2.7) and (2.9) represent the closed-form solution of the inverse kinematic problem in the sense that the required actuator lengths can be determined using

Equation (2.9) for a given vector  $\mathbf{q}(x, y, z, \alpha, \gamma, \beta)$ , representing the position and orientation of the moving platform.

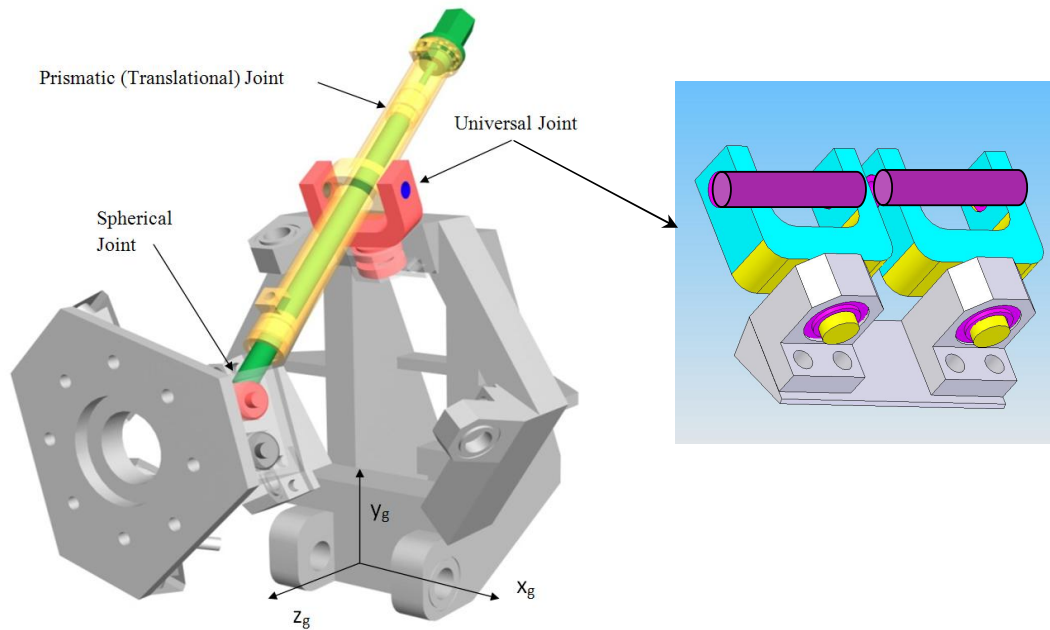


Figure 2.3: Scheme of the 6-UPS parallel robot and the Universal joints.

### 2.2.3 Spatial coordinate system of a parallel robot arm

As previously mentioned, the floating frame of reference formulation was adopted for this flexible multi-body system. In the FFRF, there are two coordinate frame types: the global frame and the floating frame (Shabana, 2005). The global frame is used to describe the motion of the reference frame of individual flexible bodies on which the location and orientation of the floating frame are defined. Local deformations of the flexible bodies are expressed in the floating frame.

Thus, the motion of each point on the flexible body is regarded as the superposition of rigid body motion in the global coordinate and flexible deformation in the local floating frame coordinate (Wang *et al.*, 2010).

The deformation of a flexible body (rod) with respect to its frame of reference can be formulated using the finite element method. In the case of slender members, shear deformation can be neglected. Therefore, each rod is modeled as a Euler-Bernoulli beam. Longitudinal deformation is neglected since the axial stiffness of intermediate

links is much higher than the lateral stiffness (Zhang *et al.*, 2007). Each rod is divided into six elements and seven nodes. Figure 2.4 explains the floating frame of reference coordinate systems used to describe the change in the position of a point  $P^i$  in a deformed body  $i$ .  $X_g Y_g Z_g$  is the global coordinate frame, and  $x_i y_i z_i$  is the floating frame attached to element no. 1 of undeformed rod  $i$  at node 1, where  $x_i$  is along the direction of the undeformed rod  $i$ . The floating frame is body fixed, i.e. moving with the rod  $i$ .

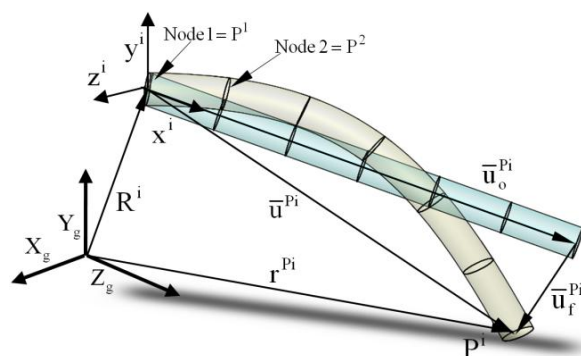


Figure 2.4: The position of a node  $P^i$  in a floating frame coordinate and finite elements of the  $i^{\text{th}}$  flexible rod.

The position of an arbitrary point (node)  $P^i$  on a flexible body  $i$  can be described in a global coordinate system as follows.

$$\mathbf{r}^{P^i} = \mathbf{R}^i + \mathbf{A}^i \bar{\mathbf{u}}^{P^i} = \mathbf{R}^i + \mathbf{A}^i (\bar{\mathbf{u}}_0^{P^i} + \bar{\mathbf{u}}_f^{P^i}) \quad (2.10)$$

where  $\mathbf{R}^i$  is the translational vector of the FFR ( $x_i y_i z_i$ ) of a body  $i$  with respect to the global coordinate frame system,  $\bar{\mathbf{u}}^{P^i}$  is the position vector of point (node)  $P^i$  within the frame of reference,  $\bar{\mathbf{u}}_0^{P^i}$  and  $\bar{\mathbf{u}}_f^{P^i}$  are the vectors describing the translational undeformed and deformed positions of node  $P^i$  with respect to a flexible body  $i$  reference coordinate system.  $\mathbf{A}^i$  is the rotation matrix of a body  $i$  (the rotation matrix of each robot arm construction ‘‘Cylinder-rod’’).

#### 2.2.4 The rotation matrix and the Euler parameters

The rotation matrix of the robot arm construction (Cylinder-rod) can be found using the following steps. Let the rotation matrix of the  $x'_i y'_i z'_i$  coordinate system with respect to the global system ( $3 \times 3$ ) be as follows.

$$\Gamma'_i = [\mathbf{x}'_i | \mathbf{y}'_i | \mathbf{z}'_i] \tag{2.11}$$

where

$$\mathbf{x}'_i = \zeta_i \times \mathbf{z}'_i / \|\zeta_i \times \mathbf{z}'_i\| \tag{2.12}$$

$$\mathbf{y}'_i = \mathbf{z}'_i \times \mathbf{x}'_i \tag{2.13}$$

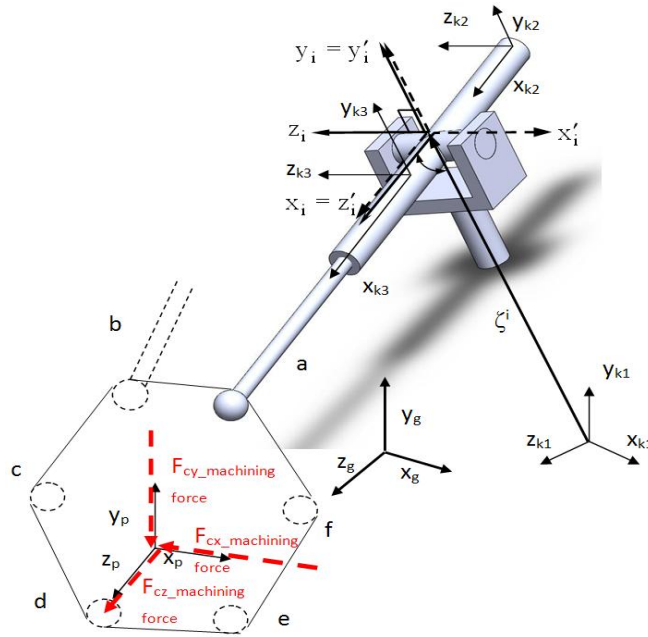


Figure 2.5: Coordinate system of each element in the parallel arm

Following a  $-90^\circ$  rotation angle about the  $y'_i$  axis, a new coordinate system  $x_i y_i z_i$  can be achieved (Figure 2.5) to align the  $x'_i$  axis with the longitudinal axis of the  $i$  flexible rod as prescribed by the Przemienicki model (Przemienicki, 1985). Hence, a new directional cosine matrix can be written as follows:

$$\Gamma_i = [\Gamma'_i] [\Gamma_{\theta_y=-90}] \tag{2.14}$$

This rotation matrix can be written as follows:

$$\mathbf{\Gamma}_i = \begin{bmatrix} \mathbf{r}_{11}^i & \mathbf{r}_{12}^i & \mathbf{r}_{13}^i \\ \mathbf{r}_{21}^i & \mathbf{r}_{22}^i & \mathbf{r}_{23}^i \\ \mathbf{r}_{31}^i & \mathbf{r}_{32}^i & \mathbf{r}_{33}^i \end{bmatrix} \quad (2.15)$$

To avoid singular conditions, the rotation matrix  $\mathbf{\Gamma}_i$  is expressed in terms of Euler parameters  ${}^e\boldsymbol{\theta}^i = [e_0^i \ e_1^i \ e_2^i \ e_3^i]$ . These parameters can be found as follows (Jazar, 2007):

$$e_0^i = \pm \sqrt{1 + \mathbf{r}_{11}^i + \mathbf{r}_{22}^i + \mathbf{r}_{33}^i} / 2 \quad (2.16)$$

$$e_1^i = (\mathbf{r}_{32}^i - \mathbf{r}_{23}^i) / 4e_0^i \quad (2.17)$$

$$e_2^i = (\mathbf{r}_{13}^i - \mathbf{r}_{31}^i) / 4e_0^i \quad (2.18)$$

$$e_3^i = (\mathbf{r}_{21}^i - \mathbf{r}_{12}^i) / 4e_0^i \quad (2.19)$$

Hence, the rotation matrix  $\mathbf{A}^i$  can be written using Euler parameters as follows:

$$\mathbf{A}^i = \begin{bmatrix} 1 - 2((e_2^i)^2 + (e_3^i)^2) & 2(e_1^i e_2^i - e_0^i e_3^i) & 2(e_1^i e_3^i + e_0^i e_2^i) \\ 2(e_1^i e_2^i + e_0^i e_3^i) & 1 - 2((e_1^i)^2 + (e_3^i)^2) & 2(e_2^i e_3^i - e_0^i e_1^i) \\ 2(e_1^i e_3^i - e_0^i e_2^i) & 2(e_2^i e_3^i + e_0^i e_1^i) & 1 - 2((e_1^i)^2 + (e_2^i)^2) \end{bmatrix} \quad (2.20)$$

where these parameters should satisfy the following mathematical constraint:

$$(e_0^i)^2 + (e_1^i)^2 + (e_2^i)^2 + (e_3^i)^2 = 1 \quad (2.21)$$

The first time derivative of the vector of Euler parameters  ${}^e\boldsymbol{\theta}^i$  and the angular velocity vector  $\bar{\boldsymbol{\omega}}^i$  has the following linear connection:

$$\bar{\boldsymbol{\omega}}^i = \bar{\mathbf{G}}^i {}^e\boldsymbol{\theta}^i \quad (2.22)$$

Local velocity transformation matrix  $\bar{\mathbf{G}}^i$  depends on the selected generalized coordinates. Using Euler parameters, the matrix  $\bar{\mathbf{G}}^i$  can be expressed as

$$\bar{\mathbf{G}}^i = \begin{bmatrix} -e_1^i & e_0^i & e_3^i & -e_2^i \\ -e_2^i & -e_3^i & e_0^i & e_1^i \\ -e_3^i & e_2^i & -e_1^i & e_0^i \end{bmatrix} \quad (2.23)$$

## 2.3 Description of a flexible body

### 2.3.1 Component mode synthesis

Component mode synthesis techniques aim to describe the large number of coordinates in the finite element model using a small number of modal coordinates based on deformation shape modes. Therefore, the dimensions of the FE model will be reduced. The deformation modes in this study were obtained using eigenvalue analysis based on the Craig-Bampton (CB) method with the orthonormalization procedure (Craig, and Kurdila, 2006, and Craig and Bampton, 1968). The equation of motion based on the flexible body FE model can be written as follows:

$$\mathbf{M}_f^i \ddot{\delta}^i + \mathbf{K}_f^i \delta^i = \mathbf{F}_f^i \quad (2.24)$$

where  $\delta^i$  is the vector of the physical displacement of the node (the nodal coordinates),  $\mathbf{M}_f^i$  and  $\mathbf{K}_f^i$  are the mass and stiffness matrices of the element obtained from the FE model, respectively, and  $\mathbf{F}_f^i$  is the vector of the external forces associated with the nodal coordinates of the flexible body. In the CB method, coordinates of the flexible body FE model are partitioned into boundary (B) and interior (I) nodal coordinates. Consequently, Equation (2.24) can be expressed in the following form:

$$\begin{bmatrix} \mathbf{M}_{BB}^i & \mathbf{M}_{BI}^i \\ \mathbf{M}_{IB}^i & \mathbf{M}_{II}^i \end{bmatrix} \begin{bmatrix} \ddot{\delta}_B^i \\ \ddot{\delta}_I^i \end{bmatrix} + \begin{bmatrix} \mathbf{K}_{BB}^i & \mathbf{K}_{BI}^i \\ \mathbf{K}_{IB}^i & \mathbf{K}_{II}^i \end{bmatrix} \begin{bmatrix} \delta_B^i \\ \delta_I^i \end{bmatrix} = \begin{bmatrix} \mathbf{F}_{fB}^i \\ \mathbf{F}_{fI}^i \end{bmatrix} \quad (2.25)$$

The CB method results in two sets of modes: non-orthogonal static correction modes and orthogonal normal modes. The static correction modes are obtained by applying the unit displacement to one boundary coordinate at a time while keeping the rest of the boundary coordinates constrained. The orthogonal normal modes are obtained by clamping all boundary nodes. Setting all the interior forces  $\mathbf{F}_{fI}^i$  to zero and setting  $\ddot{\delta} = 0$  in Equation (2.25) leads to (Craig and Bampton, 1968):

$$\delta_I^i = -[\mathbf{K}_{II}^i]^{-1} \mathbf{K}_{IB}^i \delta_B^i = \Phi_C^i \delta_B^i \quad (2.26)$$

where  $\Phi_C^i$  is the matrix of static correction modes, whose columns are the non-orthogonal constraint modes. The normal modes can be achieved by solving the following internal eigenvalue problem of the substructure clamped on its boundary.

$$[\mathbf{K}_{II}^i - (\omega_{jN}^i)^2 \mathbf{M}_{II}^i] \phi_{jN}^i = \mathbf{0} \quad (2.27)$$



This gives a set of the  $j^{\text{th}}$  eigenvalues or natural frequencies  $\omega_{jN}^i$  of the rod  $i$  associated with eigenvectors  $\phi_{jN}^i$ , which are called normal modes. The  $N$  superscript signifies the normal mode. A shape matrix that contains only normal modes can be constructed as follows:

$$\Phi_N^i = [\phi_{1N}^i, \phi_{2N}^i, \dots, \phi_{jN}^i] \quad (2.28)$$

The combination of these modes in a matrix gives the non-orthogonal CB deformation modes as follows:

$$\Phi_{CB}^i = \begin{bmatrix} \mathbf{I} & \mathbf{0} \\ \Phi_C^i & \Phi_N^i \end{bmatrix} \quad (2.29)$$

One of the advantages of using  $\Phi_{CB}^i$  is that it permits representing both the local deformation effects induced by the joints acting on the boundary DOF and the global deformation effects induced by the dynamic behavior of the body itself (Geradin *et al.*, 1994). The modal mass and stiffness matrices of the flexible body can be obtained respectively as follows:

$$\mathbf{M}_{CB}^i = \Phi_{CB}^{iT} \mathbf{M}_f^i \Phi_{CB}^i \quad (2.30)$$

$$\mathbf{K}_{CB}^i = \Phi_{CB}^{iT} \mathbf{K}_f^i \Phi_{CB}^i \quad (2.31)$$

$\mathbf{K}_{CB}^i$  is block diagonal, since there is no stiffness coupling between the static correction modes and normal modes. Conversely,  $\mathbf{M}_{CB}^i$  is not block diagonal because there is inertia coupling between the static correction modes and the normal modes. The CB modes described above cannot be used directly in the FFRF, since they are non-orthogonal. However, the modes can be orthonormalized as follows:

$$[\mathbf{K}_{CB}^i - (\hat{\omega}_j^i)^2 \mathbf{M}_{CB}^i] b_j^i = \mathbf{0} \quad (2.32)$$

where  $\hat{\omega}_j^i$  is a set of eigenvalues or natural frequencies associated with the selected  $s_m$  orthonormalized CB modes  $b_j^i$  of the flexible body. Assembling the new orthonormalized CB modes resulting from the orthonormalization procedure expressed in Equation (2.32) in a matrix results in

$$\Phi^i = [b_1^i \dots b_{s_m}^i] \quad (2.33)$$

where  $\Phi^i$  is the modal transformation matrix whose columns are the selected  $s_m$  orthonormalized CB modes.

Normalizing the orthonormalized CB modes with respect to mass and stiffness matrices of Equations (2.30) and (2.31), respectively, one can obtain the diagonal modal mass and stiffness matrices of the orthonormalized CB modes.

$$\mathbf{M}_{orth}^i = \mathbf{\Phi}^{iT} \mathbf{M}_{CB}^i \mathbf{\Phi}^i = \mathbf{I} \quad (2.34)$$

$$\mathbf{K}_{orth}^i = \mathbf{\Phi}^{iT} \mathbf{K}_{CB}^i \mathbf{\Phi}^i = \text{diag}((\hat{\omega}_1^i)^2, \dots, (\hat{\omega}_{s_m}^i)^2) \quad (2.35)$$

The resulting orthonormalized CB modes will contain approximate free-free modes (i.e. modes of the unconstrained body) and the vibration modes of the boundary DOF.

The Craig-Bampton modal matrix can be divided into two components as follows:

$$\mathbf{\Phi}^{iP} = \begin{bmatrix} \mathbf{\Phi}_R^{iP} \\ \mathbf{\Phi}_\theta^{iP} \end{bmatrix} \quad (2.36)$$

where  $\mathbf{\Phi}_R^{iP}$  is the modal matrix whose columns describe only the translational mode shapes of the node  $P^i$  within the assumed deformation modes of the flexible body  $i$  (see Shabana, 2005), and  $\mathbf{\Phi}_\theta^{iP}$  is the modal matrix that describes the rotational mode shapes of node  $P^i$ . Therefore, the displacement vector  $\bar{\mathbf{u}}_f^{P^i}$  can be expressed in modal coordinates with a modal matrix.

$$\bar{\mathbf{u}}_f^{P^i} = \mathbf{\Phi}_R^{iP} \mathbf{q}_f^i \quad (2.37)$$

where  $\mathbf{q}_f^i$  is a vector of modal coordinates. Consequently, the generalized coordinates defining the position of node  $P^i$  can be represented as

$$\mathbf{q}^{iT} = \left[ \mathbf{R}^{iT} \quad {}^e \boldsymbol{\theta}^{iT} \quad \mathbf{q}_f^{iT} \right]^T \quad (2.38)$$

Equation (2.10) can thus be rewritten using the generalized coordinates of the flexible body as follows:

$$\mathbf{r}^{P^i} = \mathbf{R}^i + \mathbf{A}^i (\bar{\mathbf{u}}_0^{P^i} + \mathbf{\Phi}_R^{iP} \mathbf{q}_f^i) \quad (2.39)$$

### 2.3.2 Equation of motion of a multibody system

The kinetic energy of a one beam element (Shabana, 2005) can be expressed as

$$\mathbf{T}^i = \frac{1}{2} \int_{V^i} \rho^i \dot{\mathbf{r}}^{iT} \dot{\mathbf{r}}^i dV^i = \frac{1}{2} \dot{\mathbf{q}}^{iT} \mathbf{M}^i \dot{\mathbf{q}}^i \quad (2.40)$$

where  $\rho^i$  and  $V^i$  are, respectively, the mass density and volume of body  $i$ ,  $\dot{\mathbf{r}}^i$  is the global velocity vector of an arbitrary point on the body, and  $\mathbf{M}^i$  is the mass matrix of the  $j^{\text{th}}$  beam element on the  $i^{\text{th}}$  rod. Therefore, the kinetic energy of the entire system is:

$$\mathbf{T}^i = \sum_{j=1}^{nj} \mathbf{T}^{ij} \quad (2.41)$$

The virtual work  $\delta W$  of the forces acting on rod  $i$  can be written as follows (Shabana, 2005):

$$\delta W^i = \delta W_s^i + \delta W_e^i \quad (2.42)$$

where  $\delta W_s^i$  is the virtual work of the elastic forces resulting from the deformation of a rod, and  $\delta W_e^i$  is the virtual work due to externally applied forces. These forces include the gravity effect, machining forces, and control forces. It can be stated that

$$\delta W_s^i = -\mathbf{q}^{iT} \mathbf{K}^i \delta \mathbf{q}^i \quad (2.43)$$

where  $\mathbf{K}^i$  is the stiffness matrix of the  $i^{\text{th}}$  rod and  $\mathbf{q}^i$  is the vector of generalized coordinates of the  $i$  rod. The stiffness matrix related to modal coordinates  $\mathbf{q}^i$  can be computed as  $\mathbf{K}^i = \mathbf{K}_{orth}^i$ , which is calculated by Equation (2.35). Meanwhile,

$$\delta W_e^i = \mathbf{Q}_e^{iT} \delta \mathbf{q}^i \quad (2.44)$$

where  $\mathbf{Q}_e^i$  is the vector of generalized external forces associated with generalized coordinates of body  $i$ . This leads to

$$\delta W^i = -\mathbf{q}^{iT} \mathbf{K}^i \delta \mathbf{q}^i + \mathbf{Q}_e^{iT} \delta \mathbf{q}^i = \mathbf{Q}^{iT} \delta \mathbf{q}^i \quad (2.45)$$

Taking into consideration the constraint equations, the Lagrange equations of the entire parallel robot, which include the elastic and the rigid bodies, can take the form (Shabana, 2005):

$$\frac{d}{dt} \left( \frac{\partial \mathbf{T}^i}{\partial \dot{\mathbf{q}}^i} \right)^T - \left( \frac{\partial \mathbf{T}^i}{\partial \mathbf{q}^i} \right)^T + \mathbf{C}_{qi}^T \boldsymbol{\lambda} = \mathbf{Q}^i \quad (2.46)$$

where  $\mathbf{C}_q$  is the Jacobian matrix of the nonlinear constraint equations,  $\mathbf{q}$  is the vector of  $n$  generalized coordinates of all bodies of the parallel robot, and  $\boldsymbol{\lambda}$  is the vector of

Lagrange multipliers. Substituting the kinetic energy  $\mathbf{T}^i$ ,  $\mathbf{C}_{qi}$ , and  $\mathbf{Q}^i$  into the Lagrangian Equation (2.46) gives the equations of the constrained motion of the flexible multibody system.

$$\mathbf{M}^i \ddot{\mathbf{q}}^i + \dot{\mathbf{M}}^i \dot{\mathbf{q}}^i - \left[ \frac{\partial}{\partial \mathbf{q}^i} \left( \frac{1}{2} \dot{\mathbf{q}}^{iT} \mathbf{M}^i \dot{\mathbf{q}}^i \right) \right]^T + \mathbf{C}_{qi}^T \boldsymbol{\lambda} = \mathbf{Q}_f^i + \mathbf{Q}_e^i \quad (2.47)$$

The equation can be written in a more compact form as

$$\mathbf{M}^i \ddot{\mathbf{q}}^i + \mathbf{C}_{qi}^T \boldsymbol{\lambda} = \mathbf{Q}_v^i + \mathbf{Q}_e^i + \mathbf{Q}_f^i \quad (2.48)$$

where  $\mathbf{M}^i$  is the mass matrix that can be written as follows:

$$\mathbf{M}^i = \int_{V^i} \rho^i \begin{bmatrix} \mathbf{I} & -\mathbf{A}_i \tilde{\mathbf{u}}^{iP} \bar{\mathbf{G}}^i & \mathbf{A}_i \Phi_R^{iP} \\ & -\bar{\mathbf{G}}^{iT} \tilde{\mathbf{u}}^{iP} \tilde{\mathbf{u}}^{iP} \bar{\mathbf{G}}^i & \bar{\mathbf{G}}^{iT} \tilde{\mathbf{u}}^{iP} \Phi_R^{iP} \\ sym & & \Phi_R^{iP^T} \Phi_R^{iP} \end{bmatrix} dV^i \quad (2.49)$$

and  $\mathbf{Q}_v$  is a quadratic velocity vector that can be defined as follows:

$$\mathbf{Q}_v^i = \int_{V^i} \rho^i \begin{bmatrix} \mathbf{A}_i \tilde{\boldsymbol{\omega}}^i \tilde{\boldsymbol{\omega}}^i \tilde{\mathbf{u}}^{iP} + 2\mathbf{A}_i \tilde{\boldsymbol{\omega}}^i \Phi_R^{iP} \dot{\mathbf{q}}_f^i \\ -\tilde{\mathbf{u}}^{iP^T} \tilde{\boldsymbol{\omega}}^i \tilde{\boldsymbol{\omega}}^i \tilde{\mathbf{u}}^{iP} \bar{\mathbf{G}}^i - 2\tilde{\mathbf{u}}^{iP^T} \tilde{\boldsymbol{\omega}}^i \Phi_R^{iP} \dot{\mathbf{q}}_f^i \bar{\mathbf{G}}^i \\ \Phi_R^{iP^T} \tilde{\boldsymbol{\omega}}^i \tilde{\boldsymbol{\omega}}^i \tilde{\mathbf{u}}^{iP} + 2\Phi_R^{iP^T} \tilde{\boldsymbol{\omega}}^i \Phi_R^{iP} \dot{\mathbf{q}}_f^i \end{bmatrix} dV^i \quad (2.50)$$

$\mathbf{Q}_v$  results from the differentiation of the kinetic energy with respect to time and with respect to the body coordinates. The quadratic velocity vector contains gyroscopic and Coriolis force components. The vector of the elastic force can be represented as follows.

$$\mathbf{Q}_f^i = - \begin{bmatrix} \mathbf{0} \\ \mathbf{0} \\ \mathbf{K}^i \mathbf{q}^i \end{bmatrix} \quad (2.51)$$

To solve Equation (2.48), which contains  $n + n_c$  unknowns, an additional set of  $n_c$  nonlinear algebraic constraint equations must be fulfilled:

$$\mathbf{C}(\mathbf{q}, t) = \mathbf{0} \quad (2.52)$$

where  $\mathbf{C}$  is the vector of nonlinear constraint equations of the parallel robot, and  $t$  is time. Equations (2.48) and (2.52) include a system of nonlinear differential algebraic equations (DAE). However, to solve the set of equations using ordinary integration

methods for differential equation (ODE), Equation (2.52) should be differentiated twice with respect to time (Shabana, 2005).

$$\mathbf{C}_q \ddot{\mathbf{q}} = \mathbf{Q}^c = -(\mathbf{C}_q \dot{\mathbf{q}})_q \dot{\mathbf{q}} \quad (2.53)$$

where  $\mathbf{Q}^c$  is the constraint force vector for the system.

## 2.4 Modeling of constraints

In this section, the constraint equations are derived for three basic constraint components, which can be further applied in the modeling of spherical joints, revolute joints, and translational joints. The terms within the equations of motion that are related to the constraints are formulated so they can be easily coupled to the system equations of motion, i.e. Equation (2.70).

### 2.4.1 Kinematic joint description

The vector  $\bar{\mathbf{v}}_f^i$ , due to deformation at the location of node  $P^i$  within the frame of reference, can be expressed as follows:

$$\bar{\mathbf{v}}_f^i = \mathbf{A}_f^{Pi} \bar{\mathbf{v}}^i \quad (2.54)$$

where  $\bar{\mathbf{v}}^i$  is a unit vector defined in the undeformed state emanating from node  $P^i$ , and  $\mathbf{A}_f^{Pi}$  is a rotation matrix that describes the orientation due to deformation at the location of node  $P^i$  with respect to the local frame. However, all the components in Equation (2.54) are described in the reference frame. The rotation matrix  $\mathbf{A}_f^{Pi}$  can be written as follows:

$$\mathbf{A}_f^{Pi} = \mathbf{I} + \tilde{\boldsymbol{\varepsilon}}^{Pi} \quad (2.55)$$

where  $\mathbf{I}$  is the  $3 \times 3$  identity matrix and  $\tilde{\boldsymbol{\varepsilon}}^{Pi}$  is a skew symmetric matrix associated with the vector  $\boldsymbol{\varepsilon}^{Pi}$  that represents the rotation of an infinitesimal volume at the node  $P^i$  with respect to the flexible body  $i$  coordinate system. Rotation changes due to deformation can be written as follows (Yoo and Haug, 1986):

$$\boldsymbol{\varepsilon}^{Pi} = \boldsymbol{\Phi}_\theta^{iP} \mathbf{q}_f^i \quad (2.56)$$

where  $\Phi_{\theta}^{iP}$  is the modal transformation matrix whose columns describe rotation coordinates of point  $P^i$  within the assumed deformation modes of the flexible body  $i$ , and  $\mathbf{q}_f^i$  is the vector of elastic coordinates.

### 2.4.2 Basic constraint equations

Joints in a multibody dynamic system can be described as combinations of three basic constraints (Korkealaakso *et al.*, 2009):

1) *Spherical constraint on two points  $C^s$* : This prevents translational movements between two bodies. The constraint equation can be defined at given points  $P^i$  and  $P^j$ . The constraint equation associated with points  $P^i$  and  $P^j$  can be written as follows:

$$\mathbf{C}^s = \mathbf{R}^j + \mathbf{A}_j \bar{\mathbf{u}}^{Pj} - \mathbf{R}^i - \mathbf{A}_i \bar{\mathbf{u}}^{Pi} = \mathbf{0} \quad (2.57)$$

2) *Perpendicular constraint  $C^{d1}$* : This prevents the rotation of vectors with respect to each other. The constraint equation for a perpendicular constraint of  $C^{d1}$  can be written as:

$$\mathbf{C}^{d1} = \mathbf{v}_f^{iT} \mathbf{v}_f^j = \bar{\mathbf{v}}^{iT} \mathbf{A}_f^{PiT} \mathbf{A}_i^T \mathbf{A}_j \mathbf{A}_f^{Pj} \bar{\mathbf{v}}^j = \mathbf{0} \quad (2.58)$$

3) *Perpendicular constraint  $C^{d2}$* : This differs from  $C^{d1}$  in that one of the vectors is defined as constant with respect to body  $i$ , whereas the other is defined between the bodies. The constraint equation for a perpendicular constraint of  $C^{d2}$  can be written as:

$$\begin{aligned} \mathbf{C}^{d2} &= \mathbf{v}_f^{iT} \mathbf{d}^{ij} = \bar{\mathbf{v}}^{iT} \mathbf{A}_i^T (\mathbf{R}^j + \mathbf{A}_j \bar{\mathbf{u}}^{Pj} - \mathbf{R}^i - \mathbf{A}_i \bar{\mathbf{u}}^{Pi}) \\ &= \bar{\mathbf{v}}^{iT} \mathbf{A}_f^{PiT} \mathbf{A}_i^T (\mathbf{R}^j + \mathbf{A}_j \bar{\mathbf{u}}^{Pj} - \mathbf{R}^i - \mathbf{A}_i \bar{\mathbf{u}}^{Pi}) = \mathbf{0} \end{aligned} \quad (2.59)$$

where  $\mathbf{d}^{ij}$  is a vector from  $P^i$  to  $P^j$  defined in the global coordinate system. By differentiating Equations (2.57), (2.58), and (2.59) twice with respect to time, the following equations can be obtained for each constraint.

$$\ddot{\mathbf{C}} = \mathbf{C}_q \ddot{\mathbf{q}} + (\mathbf{C}_q \dot{\mathbf{q}})_q \dot{\mathbf{q}} \quad (2.60)$$

Based on Equation (2.60), the following terms can be obtained for generalized coordinates related to the translation, orientation, and flexibility of the Jacobian matrix:

$$\mathbf{C}_q = \begin{bmatrix} \mathbf{C}_{Ri} & \mathbf{C}_{\bar{\theta}i} & \mathbf{C}_{qf^i} & \mathbf{C}_{Rj} & \mathbf{C}_{\bar{\theta}j} & \mathbf{C}_{qf^j} \end{bmatrix} \quad (2.61)$$

Similarly, a vector that includes quadratic velocity terms can be obtained from Equation (2.60) as follows:

$$\mathbf{Q}^c = -(\mathbf{C}_q \dot{\mathbf{q}})_q \dot{\mathbf{q}} \quad (2.62)$$

In summary, for modeling the parallel robot, the following constraints are required for description:

- spherical joint:  $\mathbf{C}^s$
- universal joint:  $\mathbf{C}^s$  and  $\mathbf{C}^{d1}$
- translational joint: three  $\mathbf{C}^{d1}$  and two  $\mathbf{C}^{d2}$ .

Obviously, the above-mentioned formulation of a translational joint can be applied to a body sliding with respect to the other by only one changing contact point and cannot be used directly for a constraint between bodies that have more than one changing contact point, for instance, a rod sliding inside a hydraulic cylinder (except when both of them are rigid bodies).

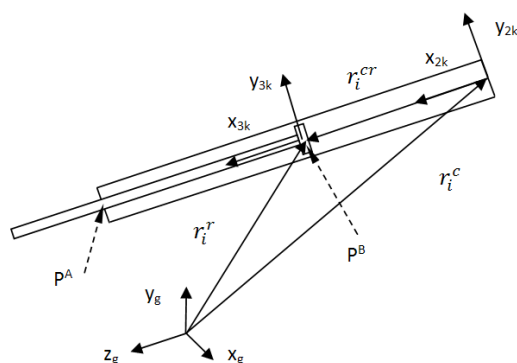


Figure 2.6: Vectors of hydraulic force inside a cylinder.

Each cylinder is constrained to the fixed plate using a universal joint. The rod is constrained to slide inside a cylinder using two changing contact points  $P^A$  and  $P^B$  (see Figure 2.6). This mechanism can be modeled using two  $\mathbf{C}^{d2}$  perpendicular constraints: at the location of node at  $P^A$  and at  $P^B$ , respectively, to prevent rotation around the two axes perpendicular to the sliding axle. The contact point of  $P^A$  can be found by interpolating between the neighboring nodes of each flexible rod for each time step. In addition, one  $\mathbf{C}^{d1}$  perpendicular constraint at the location of  $P^A$  is used to prevent rotation around the sliding axle.

## 2.5 Dynamic equation of the six closed loop parallel mechanism

The variables of Equation (2.48) can be written for the parallel robot studied in this chapter in a more compact form as follows:

$$\mathbf{M} = \text{diag}(\mathbf{M}_{arm(7+7+n_f) \times (7+7+n_f)}^1, \dots, \mathbf{M}_{arm(7+7+n_f) \times (7+7+n_f)}^6, \mathbf{M}_{mov\_pl(7+7)}) \quad (2.63)$$

where  $n_f$  is the number of selected modes. The mass matrix of each arm of the parallel robot can be written as:

$$\mathbf{M}_{arm}^i = \begin{bmatrix} \mathbf{M}_{flex\_rod}^i & \mathbf{0} \\ \mathbf{0} & \mathbf{M}_{rig\_cyl}^i \end{bmatrix} \quad i = 1, \dots, 6 \quad (2.64)$$

where the mass matrix of each flexible rod, according to Equation (2.49), is

$$\mathbf{M}_{flex\_rod}^i = \begin{bmatrix} \mathbf{m}_{RR}^i & \mathbf{m}_{R\theta}^i & \mathbf{m}_{Rf}^i \\ & \mathbf{m}_{\theta\theta}^i & \mathbf{m}_{\theta f}^i \\ sym & & \mathbf{m}_{ff}^i \end{bmatrix} \quad (2.65)$$

and the mass matrix of each rigid cylinder is

$$\mathbf{M}_{rig\_cyl}^i = \begin{bmatrix} \mathbf{m}_{RR}^i & \mathbf{m}_{R\theta}^i \\ sym & \mathbf{m}_{\theta\theta}^i \end{bmatrix} \quad (2.66)$$

Also,

$$\mathbf{q} = \left\{ \left[ \mathbf{R}, {}^e\boldsymbol{\theta} \right]_{cyl}^i, \left[ \mathbf{R}, {}^e\boldsymbol{\theta}, \mathbf{q}_f \right]_{rod}^i, \dots, \left[ \mathbf{R}, {}^e\boldsymbol{\theta} \right]_{moving\_plate} \right\}^T \quad i = 1, \dots, 6 \quad (2.67)$$

$$\mathbf{Q}^v = \left\{ \left[ \mathbf{Q}^v_R, \mathbf{Q}^v_\theta \right]_{cyl}^i, \left[ \mathbf{Q}^v_R, \mathbf{Q}^v_\theta, \mathbf{Q}^v_f \right]_{rod}^i, \dots, \left[ \mathbf{Q}^v_R, \mathbf{Q}^v_\theta \right]_{moving\_plate} \right\}^T \quad i = 1, \dots, 6 \quad (2.68)$$

$$\mathbf{Q}^e = \left\{ \left[ \mathbf{Q}^e_R, \mathbf{Q}^e_\theta \right]_{cyl}^i, \left[ \mathbf{Q}^e_R, \mathbf{Q}^e_\theta, \mathbf{Q}^e_f \right]_{rod}^i, \dots, \left[ \mathbf{Q}^e_R, \mathbf{Q}^e_\theta \right]_{moving\_plate} \right\}^T \quad i = 1, \dots, 6 \quad (2.69)$$

$\mathbf{C}_q$  is the Jacobian matrix of the nonlinear constraint equations. Figure 2.7 shows the non-zero elements of the Jacobian matrix. The parallel robot is composed of six similar arms, each contributes four constraints for the universal joint, five constraints for the translational joint, and three constraints for the spherical joint that connects the arm with the moving plate,  $\mathbf{q}$  is the vector of  $n$  generalized coordinates of all bodies of the parallel robot, and  $\boldsymbol{\lambda}$  is the vector of Lagrange multipliers.



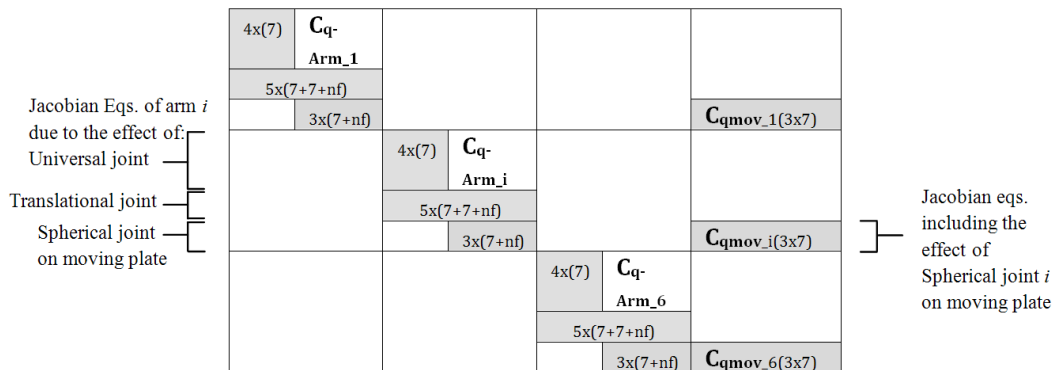


Figure 2.7: The non-zero elements of the Jacobian matrix of the parallel mechanism.

Combining Equations (2.48) and (2.60) into one matrix equation and transforming it into a first order descriptor form leads to this expression:

$$\begin{bmatrix} \mathbf{I} & \mathbf{0} & \mathbf{0} \\ \mathbf{0} & \mathbf{M}(\mathbf{q}) & \mathbf{C}_q^T(\mathbf{q}) \\ \mathbf{0} & \mathbf{C}_q(\mathbf{q}) & \mathbf{0} \end{bmatrix} \begin{Bmatrix} \dot{\mathbf{q}} \\ \ddot{\mathbf{q}} \\ \lambda \end{Bmatrix} = \begin{Bmatrix} \dot{\mathbf{q}} \\ \mathbf{Q}e + \mathbf{Q}v(\mathbf{q}, \dot{\mathbf{q}}) - \mathbf{K}\mathbf{q} \\ \mathbf{Q}c(\mathbf{q}, \dot{\mathbf{q}}) \end{Bmatrix} \quad (2.70)$$

This dynamic equation describes the overall rigid body motions of the moving platform and six rigid cylinders as well as the six flexible rods.

In Equation (2.70), the system matrices are non-diagonal, and therefore, there exists a coupling effect between the generalized rigid body motion coordinates  $\mathbf{R}_i$  and  $\boldsymbol{\theta}^i$  and the generalized elastic motion coordinates  $\mathbf{q}_f^i$ . Elastic deformation is observable in the rigid body motion and can be suppressed by controlling joint motions. This fact allows suppressing unwanted vibration by controlling the joint driving forces implemented through designing joint motion controllers (Zhang *et al.*, 2007).

## 2.6 Forces of a hydraulic cylinder

### 2.6.1 Generalized forces of a hydraulic cylinder

The hydraulic forces  $\mathbf{F}_{hi}$  inside each cylinder are considered external forces and can be included in the dynamic analysis as follows. The unit vector of the relative position of

the coordinate system of a rod to the coordinate system of a cylinder in the global system (see Figure 2.6) is given by

$$\hat{\mathbf{r}}_i^{cr} = \mathbf{r}_i^{cr} / \sqrt{\mathbf{r}_i^{crT} \mathbf{r}_i^{cr}} \quad (2.71)$$

where

$$\mathbf{r}_i^{cr} = \mathbf{r}_i^r - \mathbf{r}_i^c \quad i = 1, \dots, 6 \quad (2.72)$$

Therefore, the vectors of generalized forces associated with the generalized translation, orientation, and deformation coordinates are, respectively (Shabana, 2005),

$${}^r \mathbf{Q} e^i = \left[ \mathbf{F}_{hi} \hat{\mathbf{r}}_i^{cr} \quad -\mathbf{F}_{hi} \mathbf{G}_i^{rT} \tilde{\mathbf{u}}_i^{rT} \hat{\mathbf{r}}_i^{cr} \quad \mathbf{A}^i \Phi_R^{iP} \right] \quad (2.73)$$

$${}^c \mathbf{Q} e^i = \left[ -\mathbf{F}_{hi} \hat{\mathbf{r}}_i^{cr} \quad +\mathbf{F}_{hi} \mathbf{G}_i^{cT} \tilde{\mathbf{u}}_i^{cT} \hat{\mathbf{r}}_i^{cr} \right] \quad (2.74)$$

### 2.6.2 Derivation of the hydraulic forces

The parallel robot is driven by water hydraulic servo actuators because the hydraulic system offers high power density permitting lightweight construction, and water hydraulics is clean and suitable for the environment inside the ITER vacuum vessel. However, using water hydraulics for the drive is a challenge because of the limited flow rate of the servo valve. Speeds greater than 3 m/min result in greater than acceptable speed errors, and the robot will not track accurately (Pessi *et al.*, 2007).

The water hydraulic system comprises six cylinders for the parallel robot and one cylinder for the serial robot. Each is controlled by a Moog Type-30 servo valve. System pressures and flow rates in the system can be derived as follows.

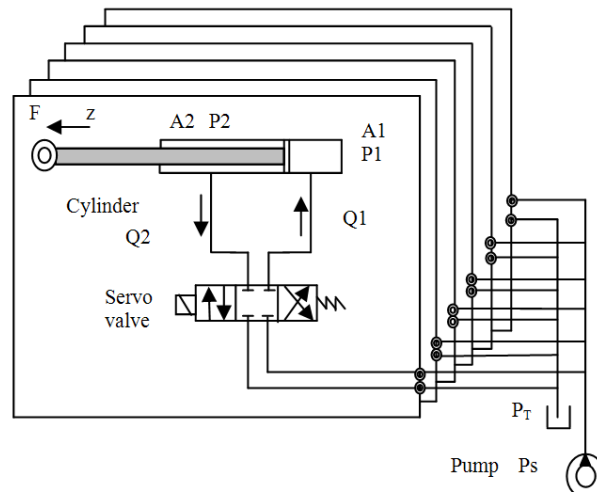


Figure 2.8: Hydraulic components of the parallel robot.

Assuming that  $P_1$  and  $P_2$  are the inflow and return water cavity pressures in Pa,  $A_1$  and  $A_2$  are the corresponding effective action areas in  $\text{m}^2$ , and  $Q_1$  and  $Q_2$  are the corresponding flows in  $\text{m}^3/\text{s}$  (see Figure 2.8), then:

$$P_L = F/A_1 = P_1 - P_2(A_2/A_1) \quad (2.75)$$

$$Q_L = Q_1 + nQ_2/(1 + n^2) \quad (2.76)$$

In this formula,  $P_L$  is the load pressure,  $Q_L$  is the load flow,  $n=A_2/A_1$ . The modeling of the valve openings proportional to the spool position  $x_v$  with  $\rho$  density and the flow can be described by the following:

$$Q_1 = c_v x_v \sqrt{2(p_s - p_1)/\rho} \quad (2.77)$$

$$Q_2 = c_v x_v \sqrt{2p_s/\rho} \quad (2.78)$$

where  $c_v$  is the flow coefficient. When the piston moves at a constant velocity:

$$Q_1 = A_1 \dot{x} \quad \text{and} \quad Q_2 = A_2 \dot{x} \quad (2.79)$$

where  $\dot{x}$  is the piston velocity. Using the linearization for Equations (2.77) and (2.78) give the following:

$$K_q = \partial Q_L / \partial x_v \quad \text{and} \quad K_c = \partial Q_L / \partial p_L \quad (2.80)$$

$$Q_L = K_q x_v - K_c p_L \quad (2.81)$$

When considering the flow continuity equation, the pressures inside chamber 1 and chamber 2 of a cylinder can be solved from the following equations:

$$\dot{p}_1 = \frac{Be}{A_1 \dot{x} + V_1} (Q_1 - A_1 \dot{x} - C_{ic} (p_1 - p_2)) \quad (2.82)$$

$$\dot{p}_2 = \frac{Be}{A_2 (L - x) + V_2} (-Q_2 + A_2 \dot{x} + C_{ic} (p_1 - p_2)) \quad (2.83)$$

where  $x$  is the displacement of a piston,  $L$  is the stroke,  $Be$  is the water bulk modulus,  $V_1$  and  $V_2$  are the volumes, and  $C_{ic}$  is internal leakage [(m<sup>3</sup>/s)/Pa]. The relative velocity  $\dot{x}$  and the relative acceleration  $\ddot{x}$  of a rod sliding inside a cylinder can be found as follows. Replacing, for convenience, the relative displacement of the rod with respect to cylinder  $x$  by  $\bar{r}_i^{cr}$ , the relative velocity  $\dot{x}$  by  $\bar{v}_i^{cr}$ , and the relative acceleration  $\ddot{x}$  by  $\bar{a}_i^{cr}$ , then:

$$\bar{r}_i^{cr} = \bar{r}_i^r - \bar{r}_i^c = \mathbf{A}_i^T (\mathbf{r}_i^r - \mathbf{r}_i^c) \quad i = 1, \dots, 6 \quad (2.84)$$

Deriving with respect to time leads to:

$$\bar{v}_i^{cr} = \dot{\bar{r}}_i^{cr} = \dot{\mathbf{A}}_i^T (\mathbf{r}_i^r - \mathbf{r}_i^c) + \mathbf{A}_i^T (\dot{\mathbf{r}}_i^r - \dot{\mathbf{r}}_i^c) \quad (2.85)$$

$$= \mathbf{A}_i^T \tilde{\boldsymbol{\omega}}_i^T (\mathbf{r}_i^r - \mathbf{r}_i^c) + \mathbf{A}_i^T (\dot{\mathbf{r}}_i^r - \dot{\mathbf{r}}_i^c) \quad (2.86)$$

Deriving again with respect to time leads to:

$$\bar{a}_i^{cr} = \dot{\bar{v}}_i^{cr} = \ddot{\mathbf{A}}_i^T (\mathbf{r}_i^r - \mathbf{r}_i^c) + \dot{\mathbf{A}}_i^T (\dot{\mathbf{r}}_i^r - \dot{\mathbf{r}}_i^c) + \dot{\mathbf{A}}_i^T (\dot{\mathbf{r}}_i^r - \dot{\mathbf{r}}_i^c) + \mathbf{A}_i^T (\ddot{\mathbf{r}}_i^r - \ddot{\mathbf{r}}_i^c) \quad (2.87)$$

$$= \left[ (\tilde{\boldsymbol{\alpha}}_i \mathbf{A}_i)^T + \left( (\tilde{\boldsymbol{\omega}}_i)^2 \mathbf{A}_i \right)^T \right] (\mathbf{r}_i^r - \mathbf{r}_i^c) + 2 \mathbf{A}_i^T \tilde{\boldsymbol{\omega}}_i^T (\dot{\mathbf{r}}_i^r - \dot{\mathbf{r}}_i^c) + \mathbf{A}_i^T (\ddot{\mathbf{r}}_i^r - \ddot{\mathbf{r}}_i^c) \quad (2.88)$$

where:

$$\boldsymbol{\alpha}_i = \mathbf{A}_i \bar{\mathbf{G}}_i \ddot{\boldsymbol{\theta}}_i \quad (2.89)$$

The hydraulic force produced inside a cylinder ( $F_h$ ) can be derived from the pressures acting on the piston as follows:

$$A_1 p_L = A_1 p_1 - A_2 p_2 \quad (2.90)$$

In addition,

$$F_h = A_1 p_L - m \ddot{x} - b \dot{x} \quad (2.91)$$

where  $b$  is the coefficient of friction (or impedance coefficient) (N.s/m). Substitution of Equations (2.82) and (2.83) into Equation (2.76) results

$$Q_L = A_1 \dot{x} + \frac{Vt}{2(1+n^2)Be} \dot{p}_L + C_{tc} p_L \quad (2.92)$$

where  $Vt$  is the total volume, and the total leakage coefficient is  $C_{tc} = ((1+n)/(1+n^3))C_{ic}$ . Applying the Laplace transformation to Equations (2.81), (2.82), (2.83), and (2.91), leads to (Dan *et al.*, 2010):

$$Q_L = K_q x_v - K_c p_L \quad (2.93)$$

$$Q_L = A_1 s x + \frac{Vt}{2(1+n^2)Be} s p_L + C_{tc} p_L \quad (2.94)$$

$$A_1 p_L = (ms^2 + bs)x + F_h \quad (2.95)$$

Equating Equations (2.93) and (2.94) gives the transfer function of the actuating unit of the valve controlled cylinder as follows:

$$K_q x_v = A_1 s x + \frac{Vt}{2(1+n^2)Be} s p_L + C_{tc} p_L + K_c p_L \quad (2.96)$$

Rearrange the last equation gives

$$K_q x_v - A_1 \dot{x} = \left[ \frac{Vt}{2(1+n^2)Be} s + C_{tc} + K_c \right] p_L \quad (2.97)$$

Errors between the predicted  $l_d$  and presented  $l$  lengths are used to determine the required force of the six actuators separately, using PID control algorithms. The controller is proposed as given by the following equation:

$$e(k+1) = l_d(k+1) - l(k) \quad (2.98)$$

where  $l_d$  is the desired local lengths of a rod.

### 2.6.3 PID control of the parallel mechanism

The popularity of PID controllers can be attributed partly to their robust performance in a wide range of operating conditions and partly to their functional simplicity, which allows simple and straightforward operation (Dorf and Bishop, 2005). To implement such a controller, three parameters must be determined for the given process: the proportional coefficient  $K_p$ , with integral coefficient  $K_i=K_p/T_i$ , and the derived coefficient  $K_d$ .

The PID controller has the following transfer function.

$$W(s) = K_p \left( 1 + \frac{1}{T_i s} + K_d s \right) \tag{2.99}$$

Figure 2.9 shows the block diagram of the control system for each cylinder.

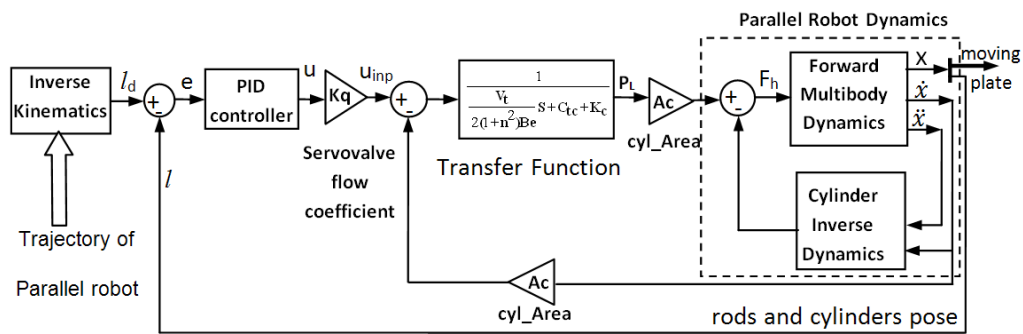


Figure 2.9: Block diagram of the control system of the parallel robot.

The traditional PID control is well-known as a discrete expression given by the equation

$$u = k_p e_t + k_i \sum_{j=0}^t e_{t-j} T + k_d \frac{e_t - e_{t-1}}{T} \tag{2.100}$$

with  $K_p$  being the proportional gain,  $K_i$  the integral gain and  $K_d$  the derivative gain. The control error  $e_t$  results from the deviation between the real length of the rod and the desired length of the rod. The index in the control error denotes the sampling time, meaning that  $e_{t-1}$  is the error of the previous sampling to  $e_t$ . The length of the time sampling period is given by  $T$  and finally the resulting control signal to trigger the valves is termed  $u$ .

This control seems to be the most common, but since the control signals are limited, the wind-up effects of the integral part can probably be encountered, meaning that the term  $\sum$  continues to integrate indefinitely. This might result in high control inputs even though the control error is low. Inevitably, the discrete control will lead to inadequate results. Consequently, the wind-up problem can be avoided by rewriting Equation (2.100) into its differential form:

$$\Delta u = u_t - u_{t-1} = k_p(e_t - e_{t-1}) + k_i T e_t + \frac{k_d}{T}(e_t - 2e_{t-1} + e_{t-2}) \quad (2.101)$$

where  $\Delta u$  is the difference of the control output between  $u_{t-1}$  and  $u_t$ .

The present control output is then defined by the sum of the previous control output and the differential output of Equation (2.101). This allows for limiting the control output to

$$u_t = (u_{t-1} + \Delta u) \Big|_{\min}^{\max} \quad (2.102)$$

where  $\Big|_{\min}^{\max}$  denotes the range of possible control values within the predefined boundaries. A possible MATLAB<sup>TM</sup> code for the described differential PID control of each cylinder is given in Figure 2.10.

```

% *****
% control cylinder 1
% *****
c1.K_p = 3.5 ; % proportional gain
c1.K_d = 2000; % derivative gain
c1.K_i = .005 ; % integral gain

c1.e_2 = c1.e_1; % error t_-2
c1.e_1 = c1.e; % error t_-1
c1.e = norm(L_d_1) - norm(dis(1).rpc); % error

c1.d_u = c1.K_p * (c1.e - c1.e_1) + c1.K_i * c1.e + c1.K_d * (c1.e - 2 * c1.e_1 + ...
    c1.e_2); % difference control output
c1.u = c1.u + c1.d_u; % control output

c1.u = sign(c1.u) * min(abs([x_1_max; c1.u])); % limit control output
c1.inp = 1.0078 * c1.u; % input to spool
c1.inp = (1* c1.u); % output of PID controller

```

Figure 2.10: MATLAB code for the described differential PID control of each cylinder.

### Summary of the proposed method

The proposed method in this chapter can be epitomized by the flow chart of Figure 2.11 as following

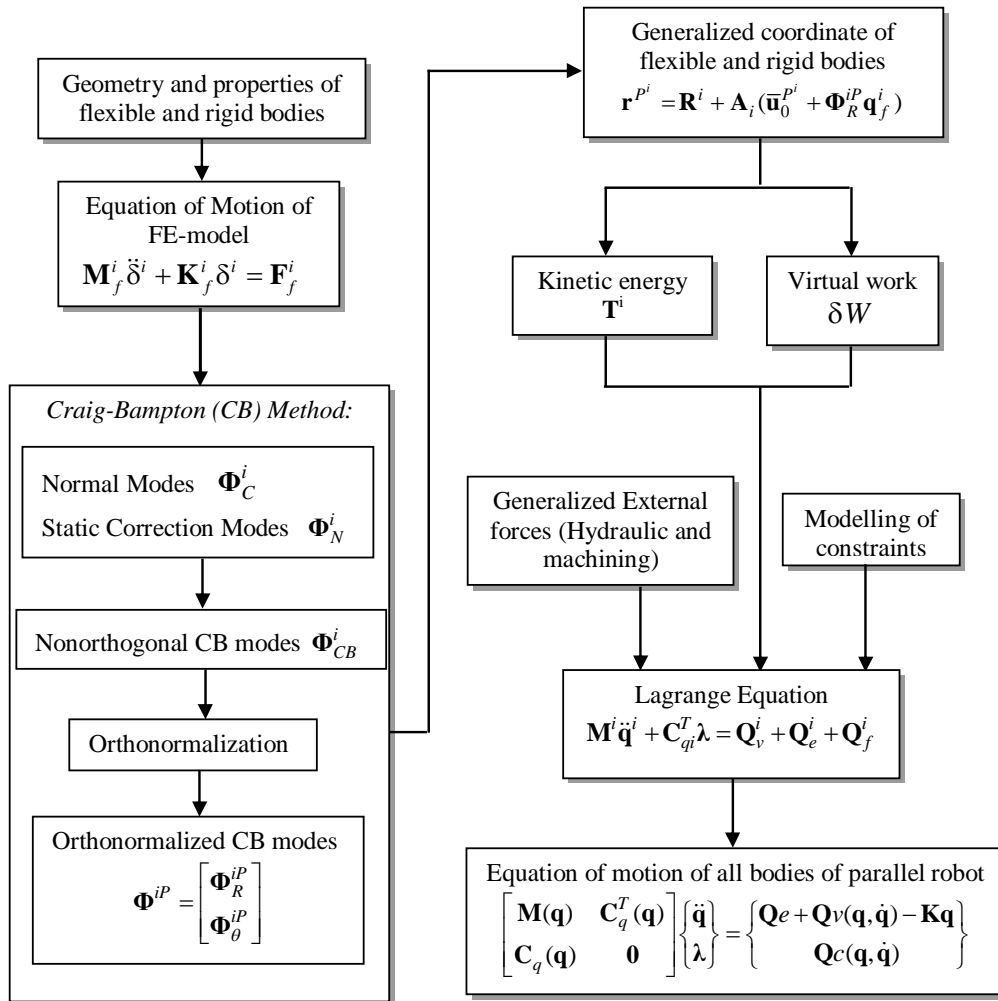


Figure 2.11: The flow chart of dynamic analysis of flexible 6UPS parallel mechanism.



## 2.7 Analysis of the serial part of the hybrid robot

The serial component of the hybrid robot can be analyzed using the equilibrium of reaction forces at the universal joint connections of the hexa-element (Figures. 2.12, 2.13, and 2.14).

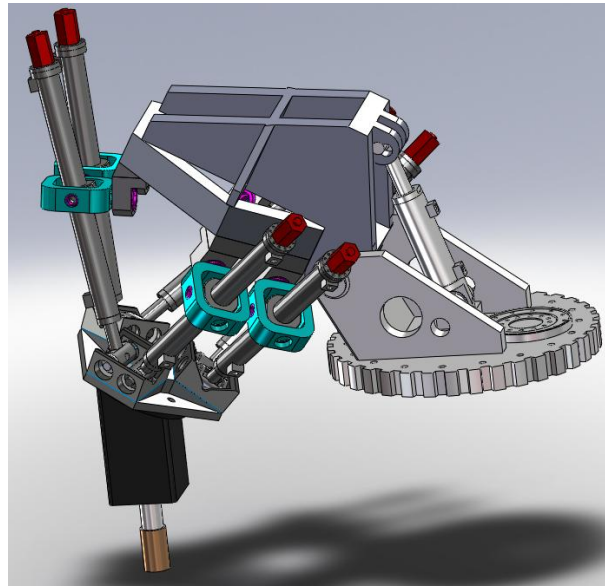


Figure 2.12: Interfacing between the serial mechanism and the parallel mechanism by the universal joints.

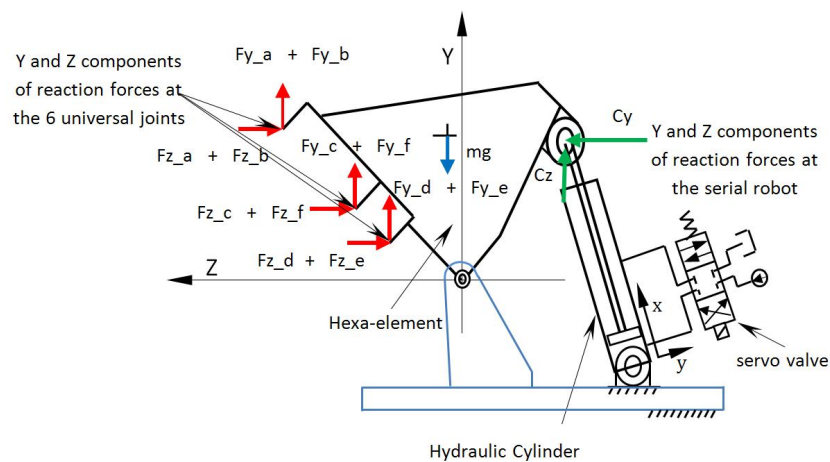


Figure 2.13: Side view of force components that affect the serial robot due to the universal joints and serial cylinder.

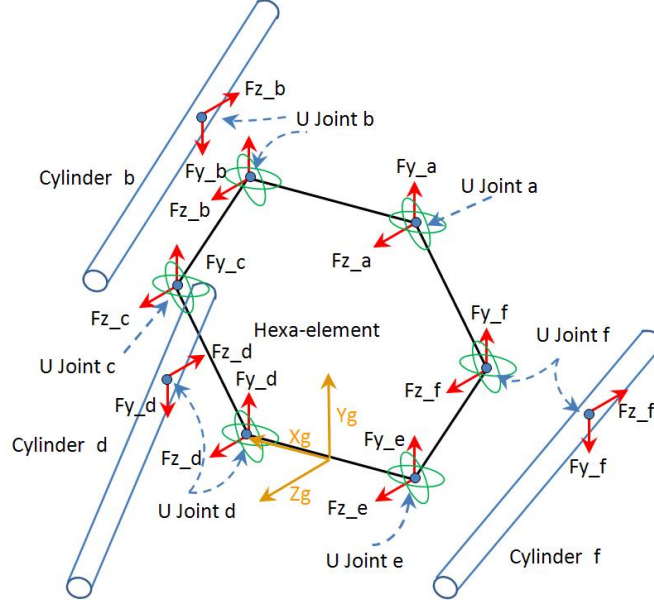


Figure 2.14: 3D view to the force components that affect the hexa-element due to the universal joints and.

The forces on the output side of the hexa-element are the result of the dynamic movement of the connected parallel linkages that lead to the end effector. The forces on the input side are the controlled driving impulses of the connected hydraulic cylinder. To achieve precise positional control of the end effector for maximum precision machining, the hydraulic cylinder should be controlled to hold the hexa-element in a fixed position with minimal positional error being transmitted to the parallel linkages (Al-saedi *et al.*, 2012). Using the multibody dynamics approach, the reaction forces of the parallel mechanism at every joint along every arm can be determined with the following equation (Shabana, 2005):

$$\mathbf{Q}_c = -\mathbf{C}_q^T \boldsymbol{\lambda} \quad (2.103)$$

Therefore, the reaction forces and torques along every arm can be found according to the non-zero elements of the sub-matrix of the Jacobian transpose, or:

$$\mathbf{C}_{q-Ai}^T = \left[ \mathbf{0} \dots \mathbf{C}_{q-Armi}^T \dots \mathbf{0} \quad \mathbf{C}_{q-mov-i}^T \right]^T, i = 1, \dots, 6 \quad (2.104)$$

Having found the components of the global reaction forces at the universal joints, the resultant of the forces in the local coordinate system of the serial robot cylinder can be found (Figure 2.14), and a PID control system can be designed to estimate the correct value of the effecting force on the serial part. The hydraulic servo valve of the serial part control is similar to that used in the parallel robot, i.e. Moog Type-30.

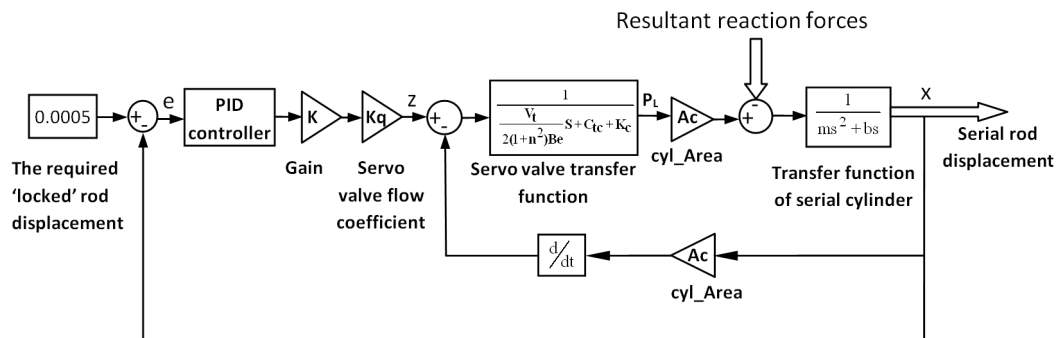


Figure 2.15: Block diagram of the control system of the serial robot.

Figure 2.15 illustrates the PID control of the serial robot where the input is the resultant reaction forces, and the output is the required locked position of the cylinder (0.5 mm).

## 2.8 Robot parameters

The actual values of the parameters of the hybrid robot of each element are tabulated in Table 2.1. The local position of the universal joint in the base plate and the local position of the spherical joint in the moving plate are given. Initially, the tip point of each rod is located 0.35 m from the cylinder outlet. Young's modulus is  $2.07 \times 10^{11} \text{ N/m}^2$ , the rod density  $\rho$  is  $7801 \text{ kg/m}^3$ , the rod radius is 0.015 m, and the length is 0.668 m. All six rods are considered as having a uniform mass distribution and cross-section. Each of the rods is divided into six elements.

Table 2.1: Mass and inertia properties of the parallel robot's elements.

element	Mass (Kg)	$I_{zz} = I_{yy}$ (Kg m <sup>2</sup> )	$I_{xx}$ (Kg m <sup>2</sup> )	$I_{xy}$ (Kg m <sup>2</sup> )
cylinder	4.589	0.2160	2.89683e-3	0
rod_piston	3.683	0.1372	4.14392e-4	0
moving plate	28.92	0.1867	0.3622	0

Base points (local):  $[0.1658\cos(120(1-i)+(90\pm 14.851)) \quad 0.1658\sin(120(1-i)+(90\pm 14.851)) \quad 0], i = 1, 2, 3$ . End effector points (local):  $[0.1296 \cos(120(1-i)+(90\pm 45.485)) \quad 0.1296 \sin(120(1-i)+(90\pm 45.485)) \quad 0], i = 1, 2, 3$ .

The moving plate (end effector) tracks a trajectory of  $x = 0$ ,  $y = -0.1t \cos(42.87)$ , and  $z = +0.1t \sin(42.87)$ , where  $t$  is the time.

A fourth order Runge-Kutta method with an integral interval time of 0.01 ms was used to solve the equations of motion. The initial values for generalized elastic deformation were  $\mathbf{q}_f^i = \mathbf{0}_{2 \times 1}$ , velocity  $\dot{\mathbf{q}}_f^i = \mathbf{0}_{2 \times 1}$ . Two non-rigid body modes and simple supports at point P<sup>B</sup> and changing point P<sup>A</sup> (Figure 2.6) were assumed. Increasing the number of modes used to describe the flexibility of each rod results in increased accuracy. However, the computational time also increases (Wang and Mills, 2004). For an actual physical system, there is internal material damping in the flexible rods, which is usually modeled proportional to stiffness (Vakil *et al.*, 2008). Because of this material damping, high frequency vibration damps out more quickly than low frequency vibration. Therefore, even if the higher modes are excited, the first few modes of vibration are dominant in the dynamic response.

In the simulations reported here, damping was not modeled, so any effect of high frequency vibration would be captured in the FEA. Using only two modes per rod in this approach may be seen as a limitation, but it offers the advantage of being fast and reasonably accurate.

## 2.9 Discussion

To verify the validity of the simulation, an ADAMS<sup>TM</sup> model of the parallel robot was developed, as previously shown in Figure 2.16. All cylinder rods were modeled as flexible bodies. The simulation model was loaded by hydraulic forces computed in the same way as forces used in the proposed method. In addition, the ADAMS<sup>TM</sup> model was controlled in the same way as the model presented in this chapter (see the Simulink model circuit in the Figures 2.21), so a direct comparison could be made between the models. The gain coefficients of the PID control (proportional gain only) for the flexible parallel robot were  $K_p = \text{diag}[0.25, 0.25, 0.25, 0.25, 0.25, 0.25]$ . Finally, the parallel robot should track the required path without machining forces at the end effector.

In Figures 2.17 and 2.18, the Y and Z trajectories of the moving plate (end effector) have been compared with the same trajectories obtained from the dynamic model developed using FFRF method. Furthermore, Figures 2.19 and 2.20 show that the y and z accelerations of the moving plate (end effector) obtained by the proposed method have been compared with the accelerations of the ADAMS<sup>TM</sup> model. The method proposed by this chapter is apparently comparatively more accurate than ADAMS<sup>TM</sup> in the overshoot and the steady state error values during the simulation, and equally accurate (in good agreement) for the remainder of the simulation period with respect to the acceleration. This result validates the modeling approach proposed in this chapter.

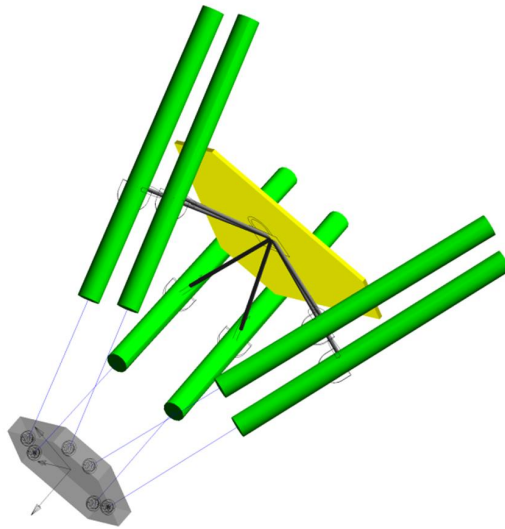


Figure 2.16: ADAMS model of the 6-UPS parallel robot.

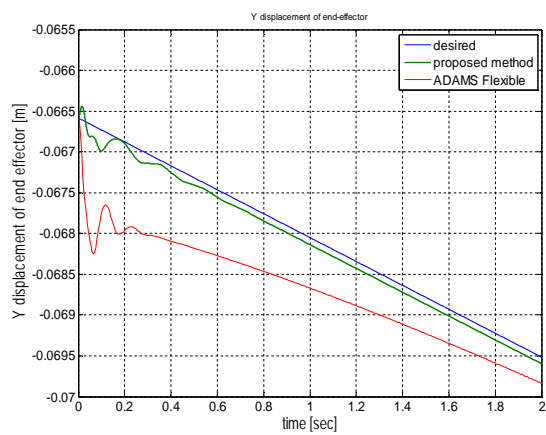


Figure 2.17: Y-displacement using the FFRF and ADAMS model.

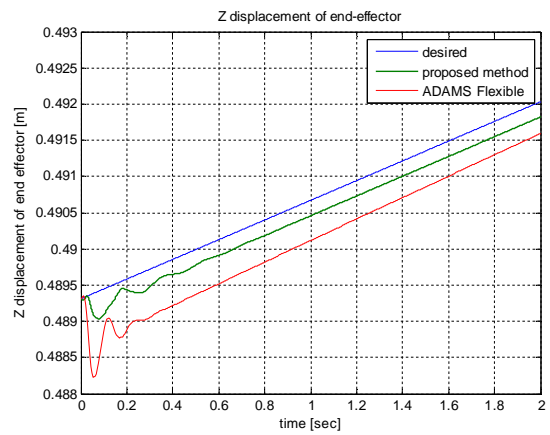


Figure 2.18: Z-displacement using the FFRF and ADAMS model.

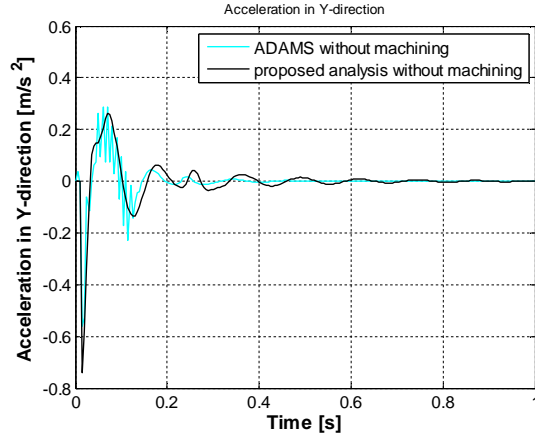


Figure 2.19: Y-acceleration using the FFRF and ADAMS model.

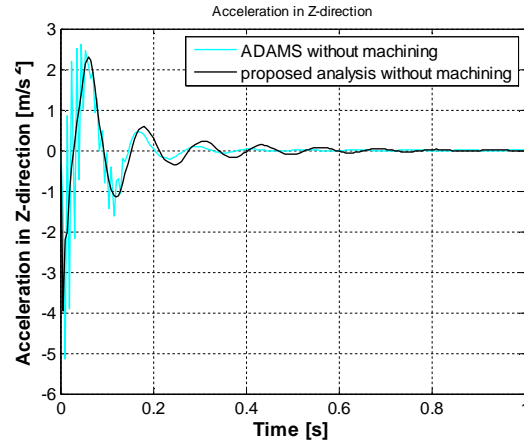


Figure 2.20: Z-acceleration using the FFRF and ADAMS model.

## 2.10 Simulation results

Two strategies were adopted to examine the effect of elastic deformation on the performance of the hybrid robot machine. First, the required path of the parallel robot with rigid rods and without machining forces was compared to the path for the same machine using flexible rods. In the second strategy, a comparison was made between the required path for the parallel robot with flexible rods with and without machining forces. The machining forces were,  $F_x = -1000\sin(2\pi ft)$ ,  $F_y = 700\sin(2\pi ft)$ , and  $F_z = -600\sin(2\pi ft)$ , with  $f = 20$  Hz.

The gain coefficients of the PID control for the flexible parallel robot with or without machining forces were  $K_p = \text{diag}[3.5, 3.5, 3.5, 3.5, 3.5, 3.5]$ ,  $K_d = \text{diag}[2000, 2000, 2000, 2000, 2000, 2000]$ , and  $K_i = \text{diag}[0.005, 0.005, 0.005, 0.005, 0.005, 0.005]$ . These coefficients were chosen to optimize the tracking of the end effector with respect to the required machining path. For the serial robot PID control, the gain coefficients were  $K_p = 60$ ,  $K_i = 0.01$  and  $K_d = 1.1$ . All these gain values were estimates made by trial and error separately for each cylinder. There are other methods to tune all these gain parameters, for instance, the Ziegler-Nichols method. This method depends on the tangent line to the response curve. However, because it is difficult to easily determine the tangent response curve for this simulation, the Ziegler-Nichols method could not be used here.

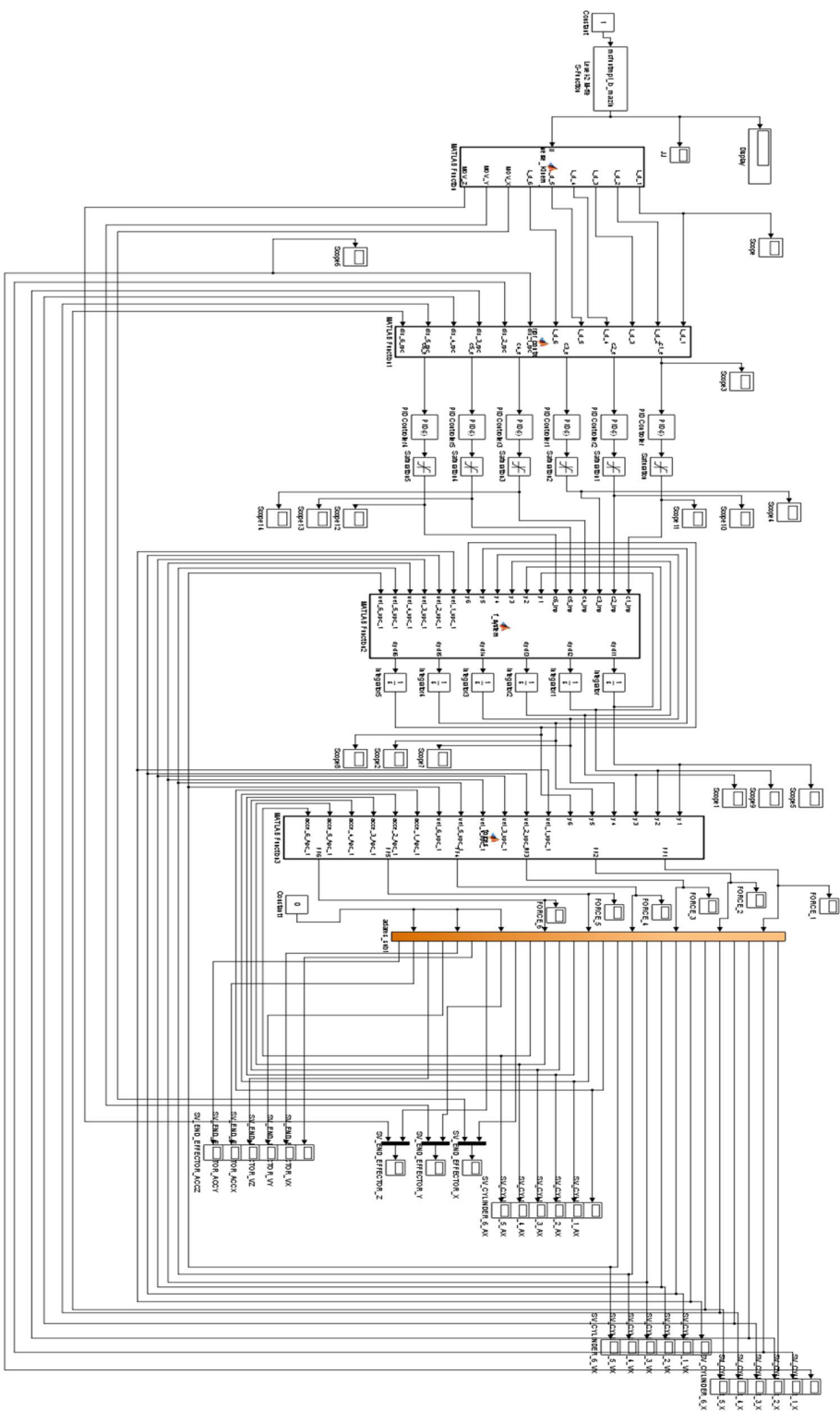


Figure 2.21 Simulink circuit for controlling the ADAMS model of the parallel robot.

The displacements presented in Figures 2.22-2.24 and 2.33-2.35 show that the hydraulic 6 DOF flexible parallel robot with PID leads the moving plate (end effector) to the desired trajectories promptly and steadily in either of the two strategies. Overshoot and steady state errors in both the y- and z-displacements were small. Like the examples presented by Vakil *et al.* (2008), end effector vibration was not obviously apparent from these displacement figures. However, the components of end effector acceleration in the y and z directions, shown in Figures 2.25 and 2.26 as well as Figures 2.36 and 2.37, clearly revealed rod vibration.

Although the influence of machining forces (variable external forces) during the simulation can be observed in all of the figures, the results indicate that the evolution of the differences in the pressures inside each cylinder (see Figures 2.27-2.32) in the case of a flexible robot are higher than the differences in the pressure in the case of a rigid robot. Similarly, Figures 2.38-2.43 indicate that the differences in the pressures inside each cylinder in the flexible robot with machining forces are higher than the differences in the pressure of the flexible robot without machining forces. This helps to select the appropriate servo valve properties for the actual robot.

Figures 2.44-2.49 present elastic deformations of the rods at their tip points. An obvious exchange of elastic strain exists between the rods. Flexibility coupling occurs between elastic deformations. This in turn indicates that deformation, as expected, is higher during machining due to the machining force effect. Moreover, it is clear from the relations of the moving plate displacement and Figures 2.44 through 2.49 that elastic deformations have a negligible effect on rigid body motion. This is because no structural damping is assumed on one side, and the introduction of a prismatic joint motion controller as a linear spring and damper has the potential to absorb the elastic strain energy on the other side (Wang and Mills, 2006, Wang and Mills, 2004). In other words, the vibration of the rods is suppressed by the PID controller due to the coupling effects of rigid body motions and elastic motions in the equation of motion.

However, the elastic motions lead to apparent changes in the velocity and acceleration of rigid body motion, illustrated in Figures 2.25 and 2.26 as well as in Figures 2.36 and 2.37. The changes will further impact the dynamic behaviors of the manipulator system (Zhang *et al.*, 2007).

Figure 2.50 shows the total force at the serial robot due to the reactions at the universal joints, which should be controlled by the serial hydraulic control system for the two cases with and without machining forces. Finally, Figure 2.51 reveals the required (locked) displacement of the rod of the serial robot. This value should be no greater than  $5 \times 10^{-5}$  m. Hence, Figure 2.51 indicates the proposed control system works accurately due to the correct selection of gains.



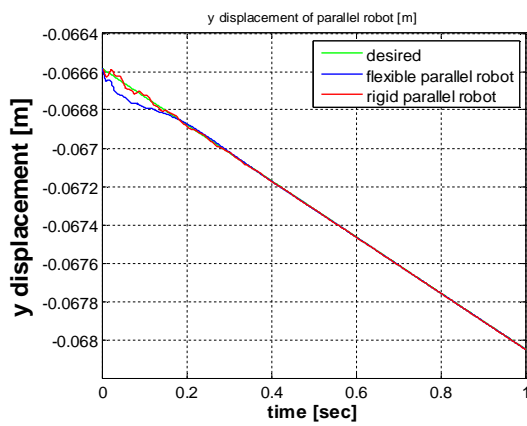


Figure 2.22: Y-displacement of a rigid and flexible parallel robot.

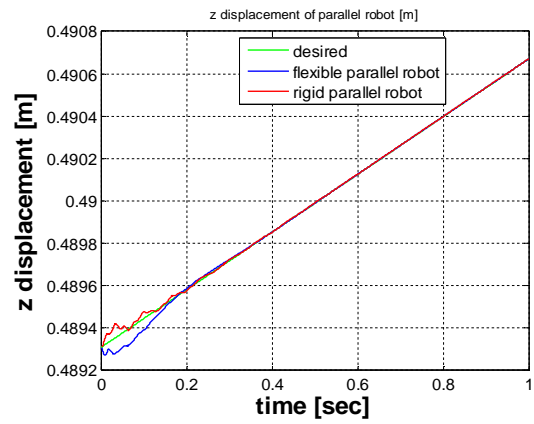


Figure 2.23: Z-displacement of a rigid and flexible parallel robot.

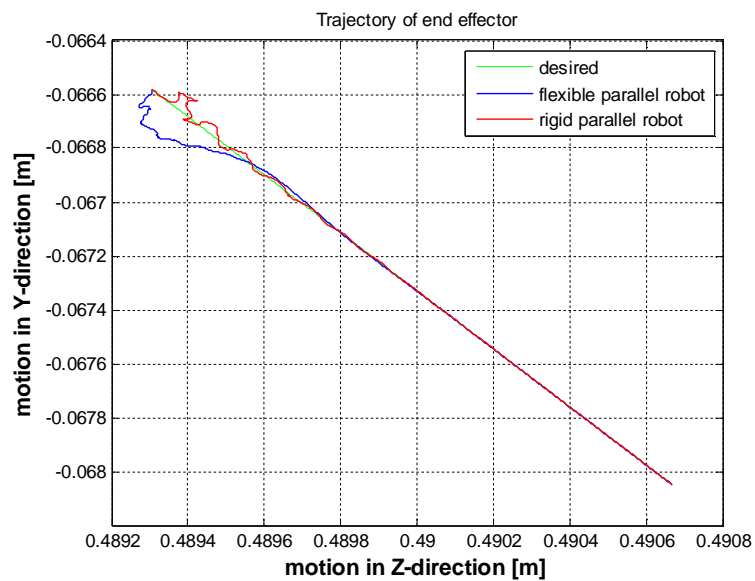


Figure 2.24: Y-Z displacement of a rigid and flexible parallel robot.

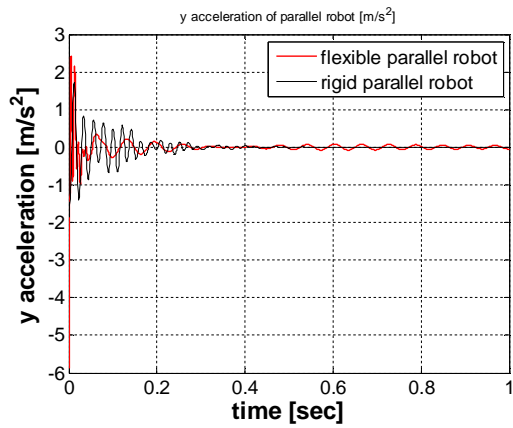


Figure 2.25: Y-acceleration of a rigid and flexible parallel robot.

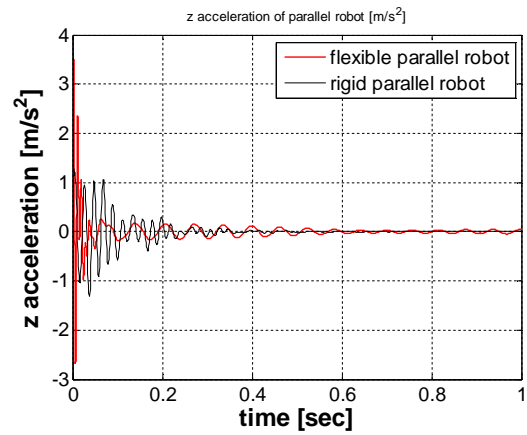


Figure 2.26: Z-acceleration of a rigid and flexible parallel robot.

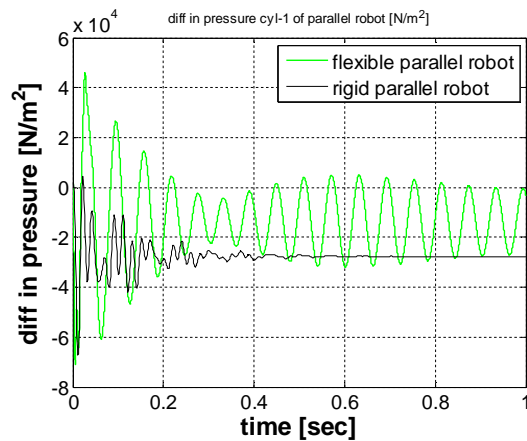


Figure 2.27: Difference in pressure in cylinder *a* of a rigid and flexible parallel robot.

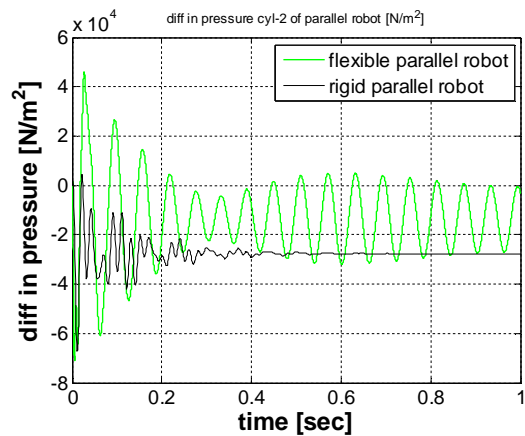


Figure 2.28: Difference in pressure in cylinder *b* of a rigid and flexible parallel robot.

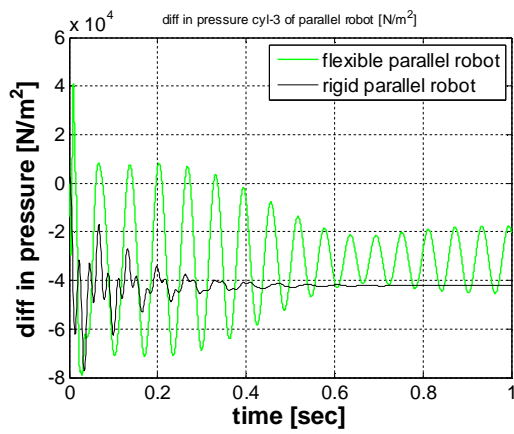


Figure 2.29: Difference in pressure in cylinder *c* of a rigid and flexible parallel robot.

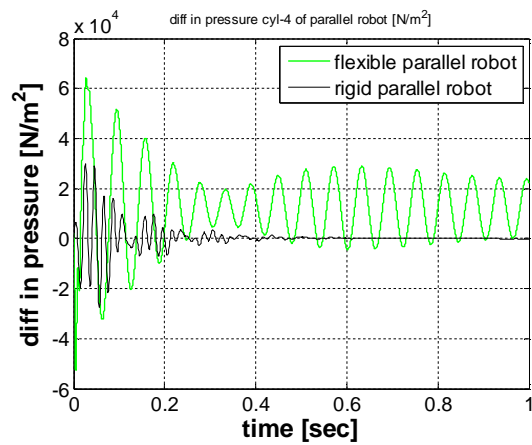


Figure 2.30: Difference in pressure in cylinder *d* of a rigid and flexible parallel robot.

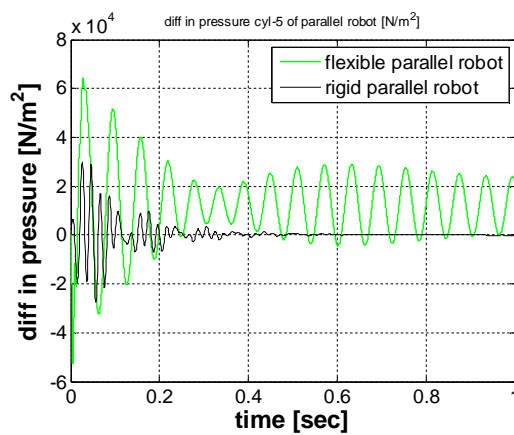


Figure 2.31: Difference in pressure in cylinder *e* of a rigid and flexible parallel robot.

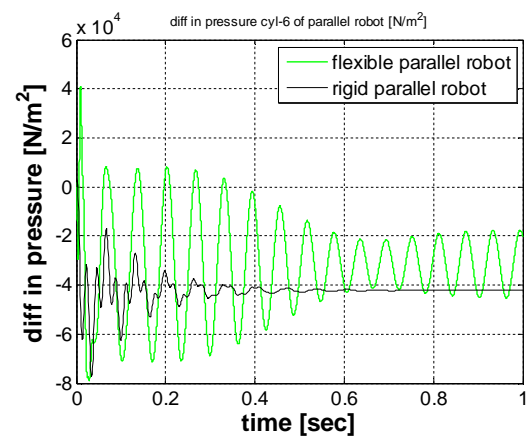


Figure 2.32: Difference in pressure in cylinder *f* of a rigid and flexible parallel robot.

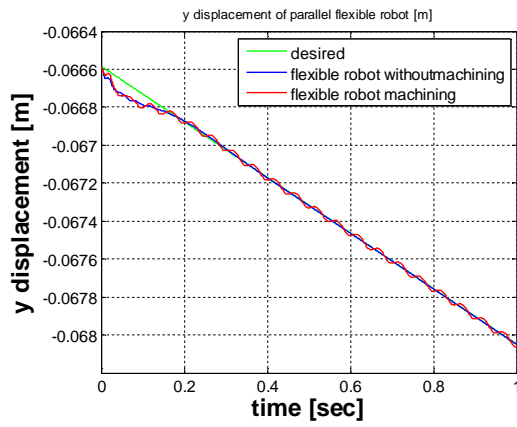


Figure 2.33: Y-displacement of a flexible parallel robot with and without machining forces.

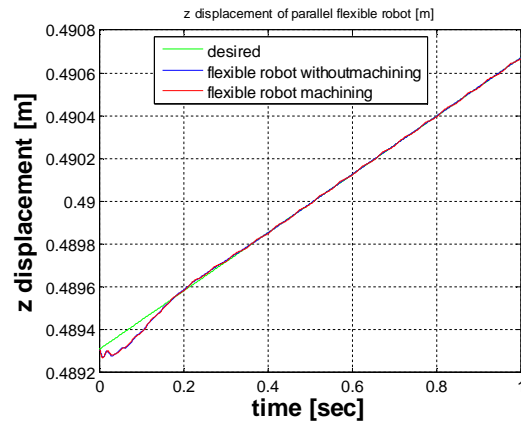


Figure 2.34: Z-displacement of flexible parallel robot with and without machining forces.

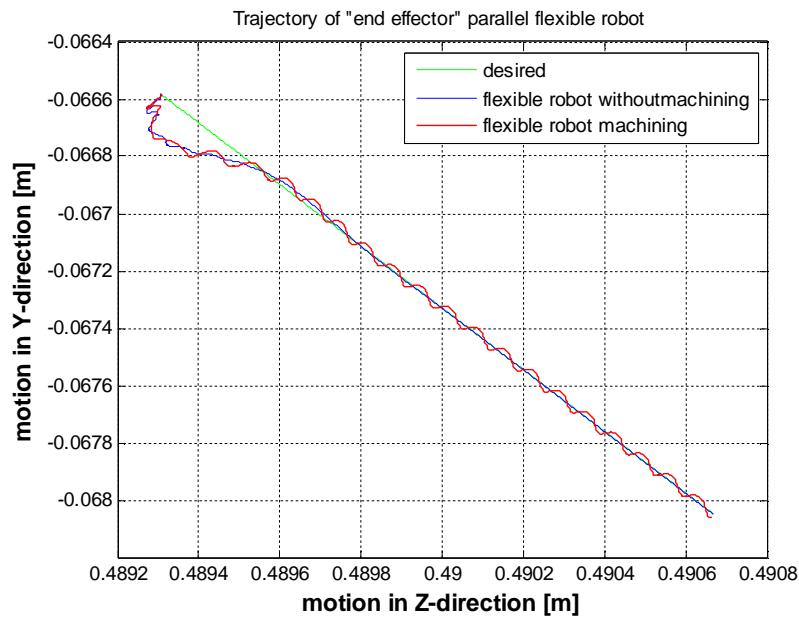


Figure 2.35: Y-X displacement (path) of a flexible parallel robot with and without machining forces.

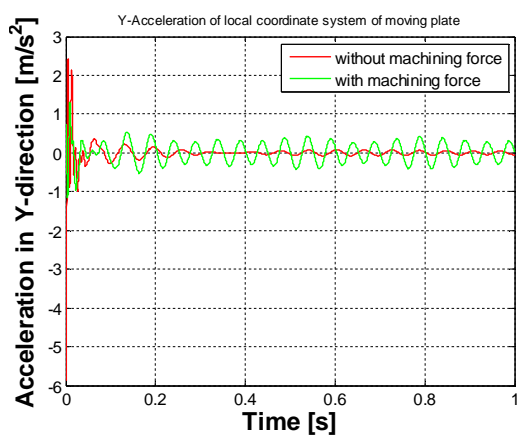


Figure 2.36: Y-acceleration of a flexible parallel robot with and without machining forces.

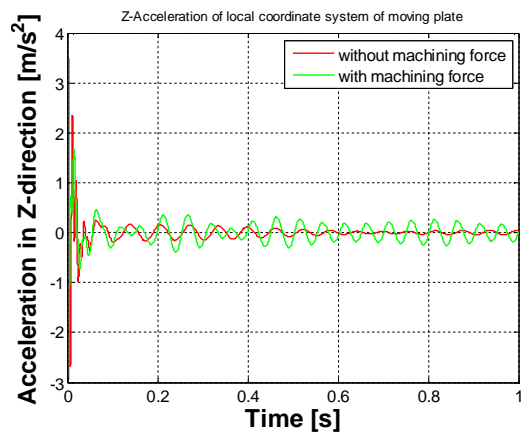


Figure 2.37: Z-acceleration of a flexible parallel robot with and without machining forces.

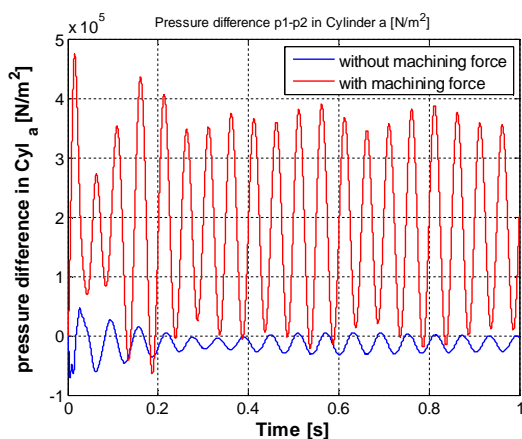


Figure 2.38: Difference in pressure in cylinder *a* of a flexible parallel robot with and without machining forces.

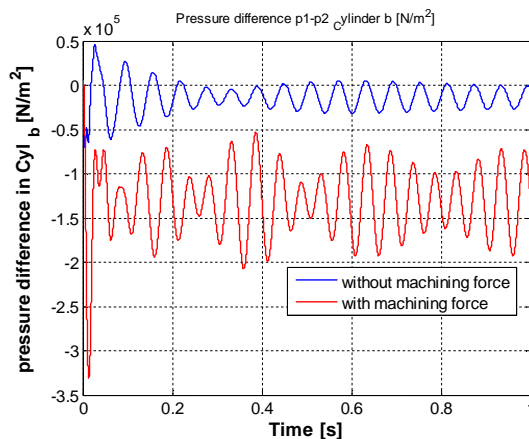


Figure 2.39: Difference in pressure in cylinder *b* of a flexible parallel robot with and without machining forces.

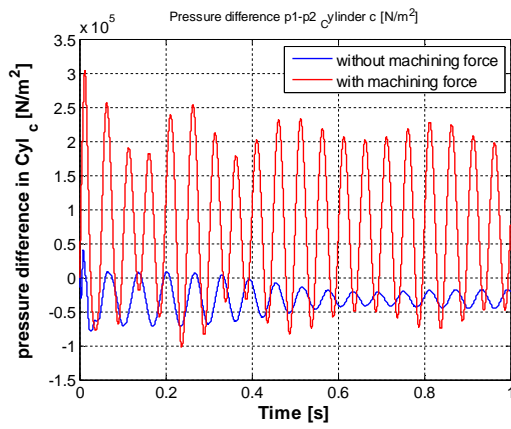


Figure 2.40: Difference in pressure in cylinder *c* of a flexible parallel robot with and without machining forces.

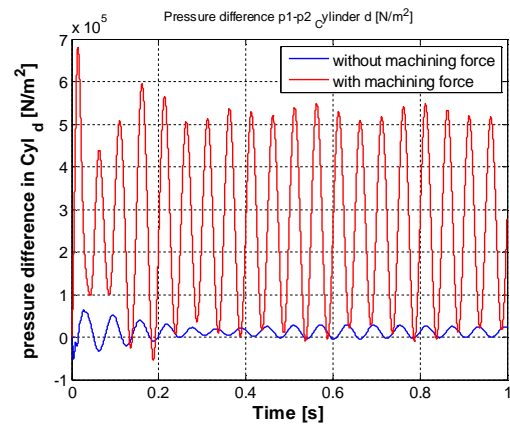


Figure 2.41: Difference in pressure in cylinder *d* of a flexible parallel robot with and without machining forces.

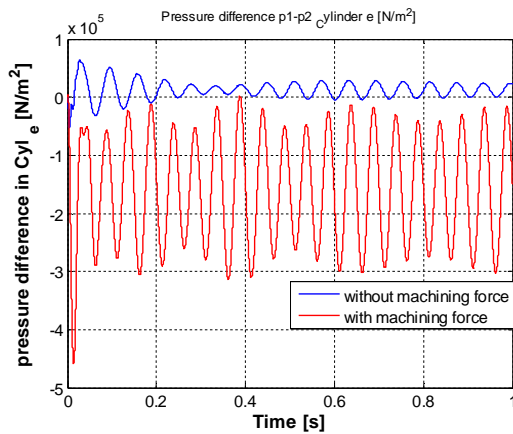


Figure 2.42: Difference in pressure in cylinder *e* of a flexible parallel robot with and without machining forces.

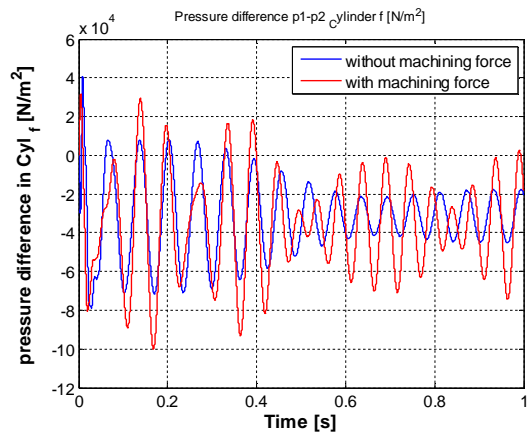


Figure 2.43: Difference in pressure in cylinder *f* of a flexible parallel robot with and without machining forces.

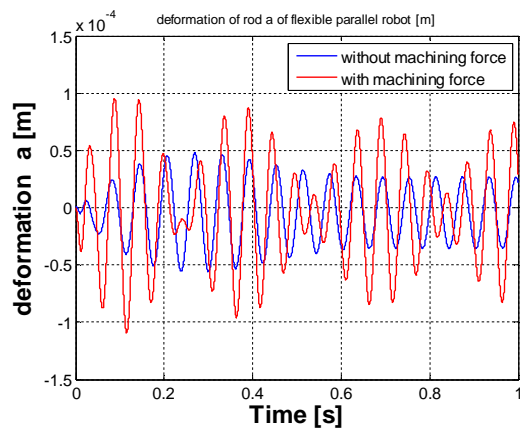


Figure 2.44: Deformation of a flexible rod in cylinder *a* of a flexible parallel robot with and without machining forces.

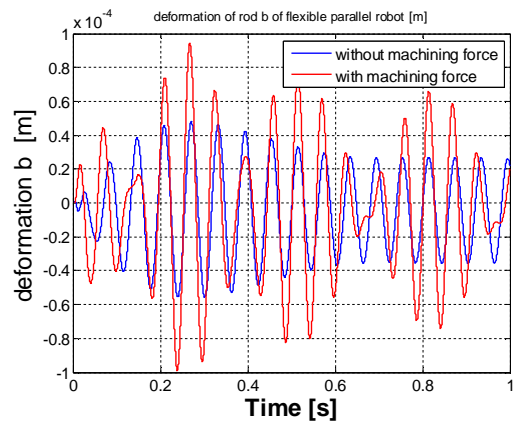


Figure 2.45: Deformation of a flexible rod in cylinder *b* of a flexible parallel robot with and without machining forces.

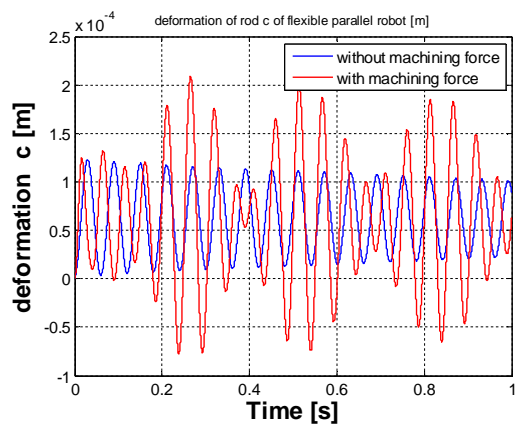


Figure 2.46: Deformation of a flexible rod in cylinder *c* of a flexible parallel robot with and without machining forces.

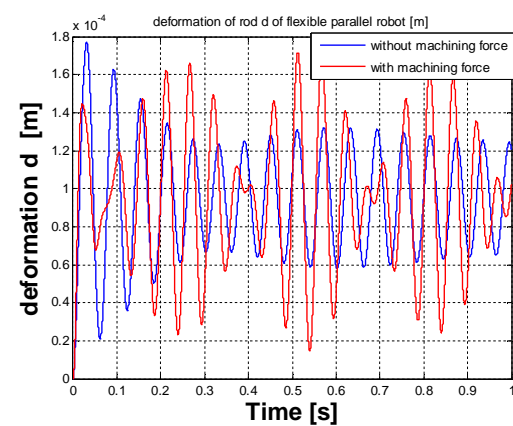


Figure 2.47: Deformation of a flexible rod in cylinder *d* of a flexible parallel robot with and without machining forces.

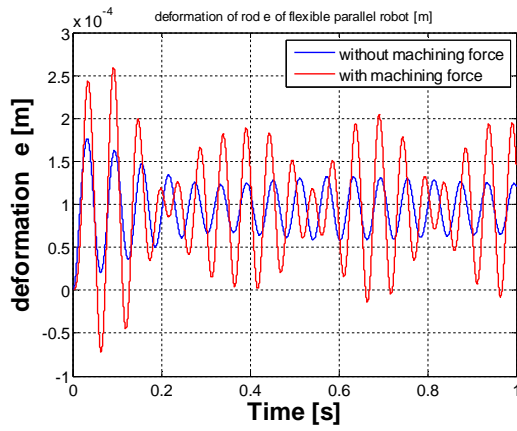


Figure 2.48: Deformation of a flexible rod in cylinder  $e$  of a flexible parallel robot with and without machining forces.

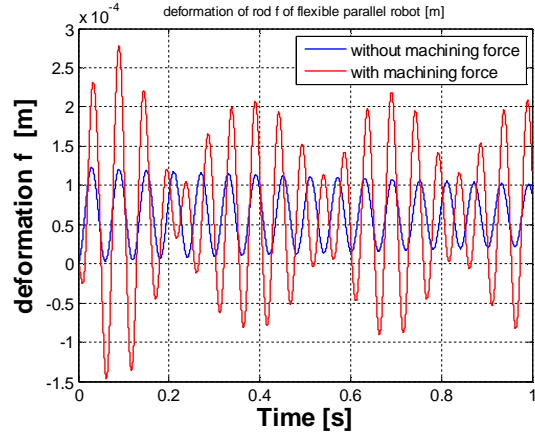


Figure 2.49: Deformation of a flexible rod in cylinder  $f$  of a flexible parallel robot with and without machining forces.

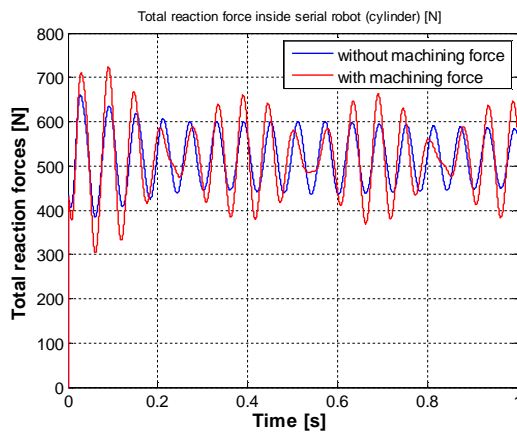


Figure 2.50: Total reaction force in a serial robot cylinder from a flexible parallel robot with and without machining forces.

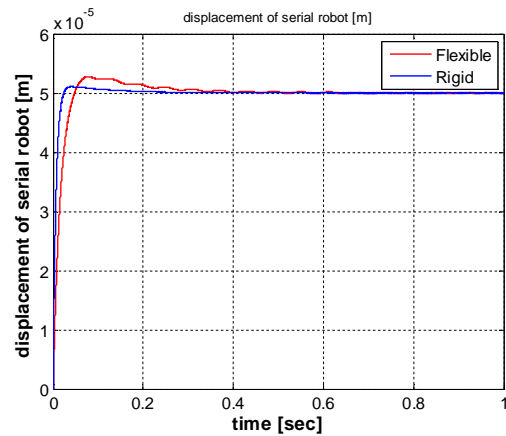


Figure 2.51: Required (locked) displacement of the rod of a serial robot cylinder from a flexible parallel robot with and without machining forces.



## **3 Intelligent methods for tuning the PID controller of a hybrid robot**

### **3.1 Introduction**

Control theory provides tools for designing and evaluating algorithms to realize desired motions or force application. The methods of linear control and those of local linearization and moving (successive) linearization are not well suited for the control problem of robotic manipulators. This is due to the fact that robotic manipulators constantly move among widely separated regions of their workspace such that no linearization valid for all regions can be found (Khoury *et al.*, 2004). On the other hand, nonlinear control methods are progressing and different classes can be identified. Nonlinear control methods used in robot system applications should however face the major difficulty resulting from the dynamic modeling of robots, i.e. the indeterminations of their parameters. The preferred methods are those which reduce or eliminate the undesired effects generated by this indetermination (Slotine and Li, 1990).

The term "fuzzy logic" was first introduced with the 1965 proposal of fuzzy set theory by Lotfi A. Zadeh (Zadeh, 1965). In Fuzzy control theory there are two contradictory requirements: interpretability versus accuracy. In practice, one of the two properties prevails. Fuzzy modeling research field is divided into two areas: linguistic fuzzy modeling that is focused on interpretability, mainly the Mamdani model (Mamdani, 1974); and precise fuzzy modeling that is focused on accuracy, mainly the Takagi-Sugeno-Kang (TSK) model (Takagi and Sugeno, 1985). Mamdani's method was among the first control systems built using fuzzy set theory. It was proposed in 1975 by Ebrahim Mamdani (Mamdani, 1974) as an attempt to control a steam engine and boiler combination by synthesizing a set of linguistic control rules obtained from experienced human operators. The main difference between Mamdani and Sugeno is that the Sugeno output membership functions are either linear or constant.

This chapter presents two methods used to tune the PID control gains of the parallel robot. The first is the fuzzy inference method and the second is the adaptive neural-fuzzy inference system (ANFIS). Using the flexible multibody dynamics results and the simulations of the hydraulic control system, the input and output to the suggested intelligent control systems can be studied as follows.

### 3.2 Fuzzy method for tuning the PID gains

Among the recent nonlinear control methods, current fuzzy control methods have drawn the attention of many researchers. In fact, these methods do not require knowledge of the dynamic model of the controlled system. This feature becomes of major importance when dealing with complex nonlinear systems. Moreover, the dynamic modeling of robot arms shows dependency on their dynamical parameters that vary with the performed task (e.g., centers of gravity of links affected by tool replacements). These considerations also give an advantage to fuzzy control methods over other nonlinear methods as a result of their robustness towards perturbations affecting the system (Khoury *et al.*, 2004).

Although control methods, especially nonlinear ones, have greatly evolved, the proportional-integral-derivative (PID) control method is still widely used in all domains (Khoury *et al.*, 2004). The success of the PID control is attributed to its simplicity (in terms of design and tuning) and to its good performance in a wide range of operating conditions. However, the necessity of retuning the PID controllers characterizes their major disadvantage when the controlled plant is subjected to disturbance or when it presents complexities (nonlinearities).

#### 3.2.1 Fuzzy controller and its membership function

The parallel robot is considered a closed mechanical chain that make the dynamics of the parallel manipulators highly complex and their dynamic models highly nonlinear. Because of these conditions, a conventional PID controller cannot reach satisfactory results. According to Tian (2004) and Feng (2009), a self-tuning parameter fuzzy PID controller provides control of the system with excellent reliability, stability, and accuracy. The basic approach is to try to detect when the controller is not properly tuned and then seek to adjust the PID gains to improve the performance. The schematic structure of the self-tuning-parameter fuzzy-PID controller is given in Figure 3.1.

The fuzzy controller is composed of the following four elements:

1. A *fuzzification interface*, which converts controller inputs into information that the inference mechanism can easily use to activate and apply rules.
2. A *rule base or knowledge base* (a set of **IF-THEN** rules), which contains a fuzzy logic quantification of the expert's linguistic description of how to achieve good control.
3. An *inference mechanism or decision making mechanism* (also called a "fuzzy inference" module), which emulates the expert's decision-making in interpreting and applying knowledge about how to best control the plant.

4. A *defuzzification interface*, which converts the conclusions of the inference mechanism into actual inputs for the process.

In this control step, the error and the change in error are selected as the inputs of the fuzzy logic control (FLC). For simplification and convenience, the actual (crisp) physical values of the inputs and outputs of the FLC are first mapped onto the predetermined normalized domain. This mapping is done by a normalization equation for the first set of inputs

$$\underline{x} = \frac{2}{\underline{x}_{\max} - \underline{x}_{\min}} (\underline{x} - \underline{x}_{\min}) - 1 \quad (3.1)$$

and for the second set of inputs

$$\underline{y} = \frac{2}{\underline{y}_{\max} - \underline{y}_{\min}} (\underline{y} - \underline{y}_{\min}) - 1 \quad (3.2)$$

where  $\underline{x}$  is the normalized input, and  $\underline{x}$  is the actual input value which is represented by error E and change in error EC, and  $\underline{x}_{\max}$  and  $\underline{x}_{\min}$  represent the maximum and minimum of the input values, respectively. In fuzzy set theory, the characteristic function for the crisp set is generalized to a partial membership function that assigns to every  $\underline{x} \in \mathbf{X}$  a value from the unit interval  $[-1, 1]$ . It is written as:

$$x : \underline{x} \rightarrow [-1, +1] \quad (3.3)$$

and

$$y : \underline{y} \rightarrow [-1, +1] \quad (3.4)$$

Thus, every element  $x$  has a membership degree  $\mu(x) \in [-1, +1]$ . The advantage of this operation is that fuzzification, rule firing (decision), and defuzzification can be designed independently of the actual physical domains. Usually, the normalized domain is defined in the range of  $[-1, +1]$ .

In Figure 3.1, the input is the reference value of the rod length and the output is the actual rod length. Inputs for the fuzzy block are rod length error E and the time derivative of a rod length error, EC. The PID controller parameters Kp and Kd are self-tuned according to the following logic rules by *fuzzy inference*. It was found that Ki for a suggested track has a constant value throughout the simulation period. Therefore, there is no need to tune it.

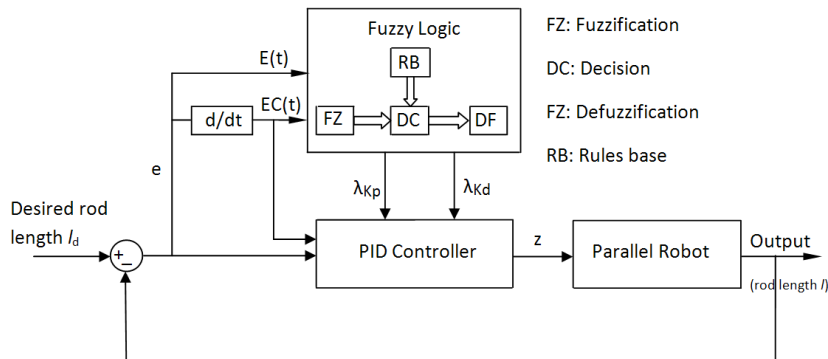


Figure 3.1: Self-tuning-parameter fuzzy PD controller structure.

After all of the inputs and outputs are defined for the fuzzy controller, the fuzzy control system can be specified. The linguistic description is provided by an expert on PID parameter tuning.

Tian (2004) states:

*Since  $K_p$  can speed up the control process, at the beginning of the control process,  $K_p$  should be larger in order to reduce the rising time and make the control process faster. In the middle of the control sequence,  $K_p$  should be adjusted to its middle value for the consideration of system stability and control accuracy. In the final period,  $K_p$  should be given a smaller value, compared with the beginning of the process, in order to reduce the steady-state error.*

*$K_d$  can suppress the overshoot of the control system and the change of the length error. Thus, when the change of the length error is large,  $K_d$  should be larger. While when the change of the length error is smaller,  $K_d$  should be given a smaller value.*

Subsequently, the linguistic quantification above specifies a set of rules (a rule base) that captures the expert's knowledge about how to control the rod length. The knowledge of the process, which is a fuzzy model, is always described using simple fuzzy linguistic rules instead of precise mathematical functions. The general expression of a rule for this control system is as follows:

$R_i$ : **IF**  $E$  is  $NE_m$  **and**  $EC$  is  $NEC_n$ , **THEN**  $\lambda_{Kp}$  is  $NK_1$ ,  $\lambda_{Kd}$  is  $NK_2$ ,

where  $\lambda_{Kp}$  and  $\lambda_{Kd}$  are the adjustment coefficients of the proportional and integral parameters, respectively (i.e. the output of the FLC), and if the normalized  $E$ ,  $EC$ , and  $NK$  are represented by  $NE$ ,  $NEC$ , and  $NK$ , respectively, then:  $NE_m \in NE$ ,  $NEC_n \in NEC$ ,  $NK_1, NK_2 \in NK$ .

The membership function is used to represent the magnitude of participation of each input graphically. It associates a weighting with each of the inputs, defines functional overlaps between inputs, and ultimately determines an output response. Figures 3.2 and 3.3 show the membership functions for inputs and outputs, respectively. Figure 3.2 shows two inputs: the rod position error  $E$  and the derivation of the error  $EC$ . Both  $E$  and  $EC$  are divided into the seven values  $\{NB, NM, NS, ZO, PS, PM, PB\}$ , where  $NB$  is Negative Big,  $NM$  is Negative Medium,  $NS$  is Negative Small,  $ZO$  is Zero,  $PS$  is Positive Small,  $PM$  is Positive Medium, and  $PB$  is Positive Big.

The fuzzy output variable  $NK$  is defined as  $NK=\{ZE, VS, S, SB, MB, B, VB\}$ , where  $ZE$  is zero,  $VS$  is very small,  $S$  is small,  $SB$  is small big,  $MB$  is medium big,  $B$  is big, and  $VB$  is very big.

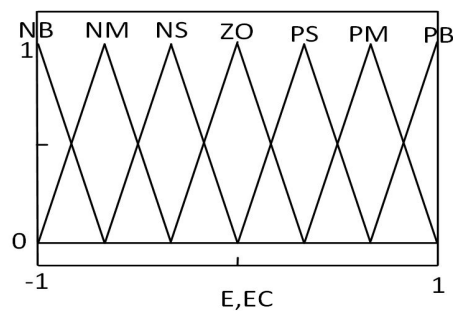


Figure 3.2: Membership function of inputs.

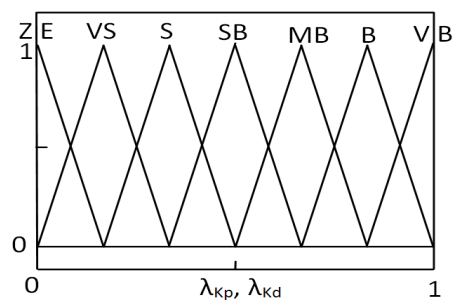


Figure 3.3: Membership function of outputs.

The horizontal axis in Figure 3.2 illustrates the scaling gain for a rod length error  $E$  and its time differential  $EC$ . Based on the input information ( $E, EC$ ), the triangle membership function is chosen as they are the most common and easy to implement in an embedded controller. Each of the triangles represents an area of the effect of rules.

Similar interpretations of linguistic values were made in the definition of the membership functions on the outputs.

By combining the fuzzy sets of inputs for the rod position error (7) and the differential of the rod position error (7), there are a total of  $7 \times 7 = 49$  rules for tuning one controller output. Because we have two outputs ( $K_p$  and  $K_d$ ), there are  $49 \times 2 = 98$  rules for each servo controller. The rule base for the tuning of the control system is shown in Table 3.1

Table 3.1: Fuzzy rule base for the tuning of the PD control system gains.

		Rod length error $E$						
		NB	NM	NS	ZO	PS	PM	PB
Differential of rod length error $EC$	NB	VB/VB	B/B	SB/MB	S/SB	SB/SB	MB/SB	B/B
	NM	B/B	MB/SB	SB/SB	S/VS	SB/S	MB/S	MB/MB
	NS	MB/SB	SB/S	S/S	VS/VS	S/VS	SB/VS	SB/S
	ZO	SB/VS	S/S	VS/VS	ZE/ZE	VS/VS	S/S	SB/VS
	PS	SB/S	SB/VS	S/VS	VS/VS	S/S	SB/S	MB/SB
	PM	MB/MB	MB/S	SB/S	S/SB	SB/SB	MB/SB	B/B
	PB	B/B	MB/SB	SB/SB	S/MB	SB/MB	B/B	VB/VB

Table 3.1 illustrates what rule is effective when a specific combination of the rod position error  $E$  and its time differential  $EC$  is presented. For instance, the rod position error  $E$  is “located” in the NS triangle, and the differential of error  $EC$  in the ZO triangle. The combination of this information tells us that the output for  $K_p$  follows the NS triangle rule, and  $K_d$  follows the PS triangle rule.

The *inference process or decision* generally involves two steps:

- (1) The premises of all of the rules are compared with the controller inputs to determine that rules apply to the current situation.
- (2) The conclusions (what control actions to take) are determined using the rules that have been determined to apply at the current time. The conclusions are characterized with a fuzzy set that represents the certainty that the input to the plant should take for various values (Passino and Yurkovich, 1997).

The “AND” operator is applied, and then the membership degree of the output in a rule can be calculated as:

$$\mu(z) = \min\{\mu(x); \mu(y)\} \quad (3.5)$$

where  $z = z(x, y)$

Figure 3.4 illustrates the process of implementation of the rules and the logical operator “AND”. The result  $\mu(z)$  should undergo a defuzzification process.

A *defuzzification interface* refers to the way a crisp value is extracted from a fuzzy set as a representative value by combining the results of the inference process and then computing the fuzzy centroid of the area (of the chopped off triangles as can be seen in Figure 3.4). The result is the  $\lambda(E;EC)$  weight coefficient (crisp value) which depends on E and EC and is used for calculating  $K_p$  and  $K_d$ , which can be summarized as follows:

$$\lambda^{COG} = \frac{\sum_{i=1}^N \mu(z_i) \cdot z_i}{\sum_{i=1}^N \mu(z_i)} \quad (3.6)$$

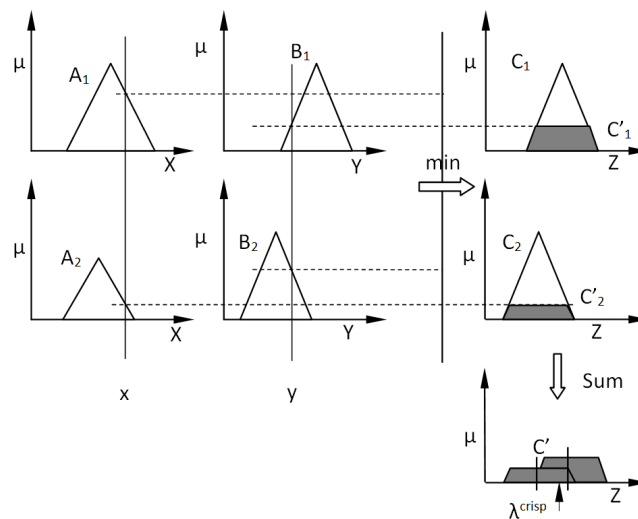


Figure 3.4: Graphical representation of fuzzy controller operations.

Now, the tuned parameters of the PID controller can be found as follows (Tian, 2004):

$$K_p = K_{p,Min} + \lambda_{Kp}(E_L, EC_L)(K_{p,Max} - K_{p,Min}) \quad (3.7)$$

$$K_d = K_{d,Min} + \lambda_{Kd}(E_L, EC_L)(K_{d,Max} - K_{d,Min}) \quad (3.8)$$

where  $\lambda$  is a weight coefficient, and  $K_{p,Max}$ ,  $K_{p,Min}$ ,  $K_{d,Max}$ , and  $K_{d,Min}$  are the maximum and minimum limits for the proportional gain and the integral gain, respectively. Figure 3.3 shows outputs  $\lambda_{Kp}$  and  $\lambda_{Kd}$ . The initial values for the self-tuning parameter of the fuzzy PD were chosen to be the same as those for a conventional PID controller. Six fuzzy controllers are used in a parallel structure and embedded into the control system. The error vector is computed for each fuzzy controller by using the difference between the actual rod length generated by the dynamic model of the manipulator and the desired rod length.

The control surface of fuzzy-PD controller representing the relation between inputs and output  $\lambda_{Kp}$  can be seen in Figure 3.5, while the control surface of fuzzy-PD controller representing the relation between inputs and output  $\lambda_{Kd}$  can be seen in Figure 3.6.

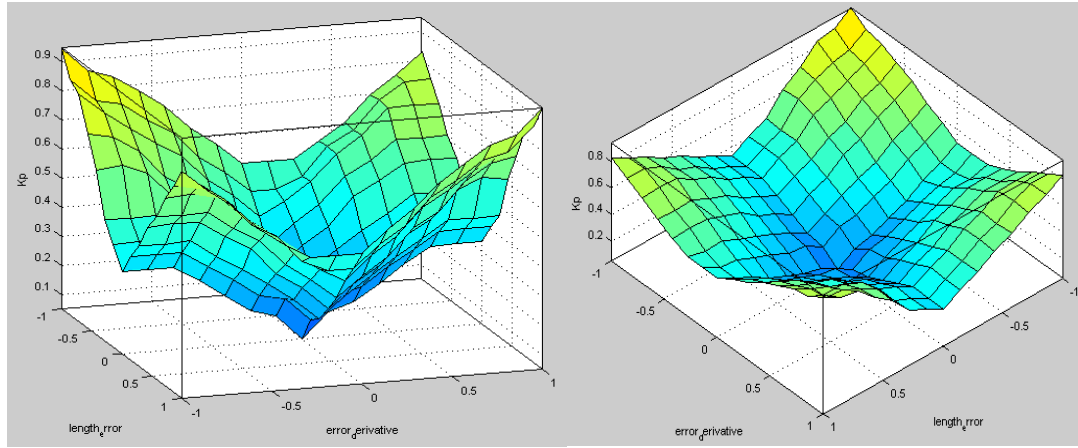


Figure 3.5: Control surface of fuzzy-PD controller representing the relation between inputs and output  $\lambda_{Kp}$ .



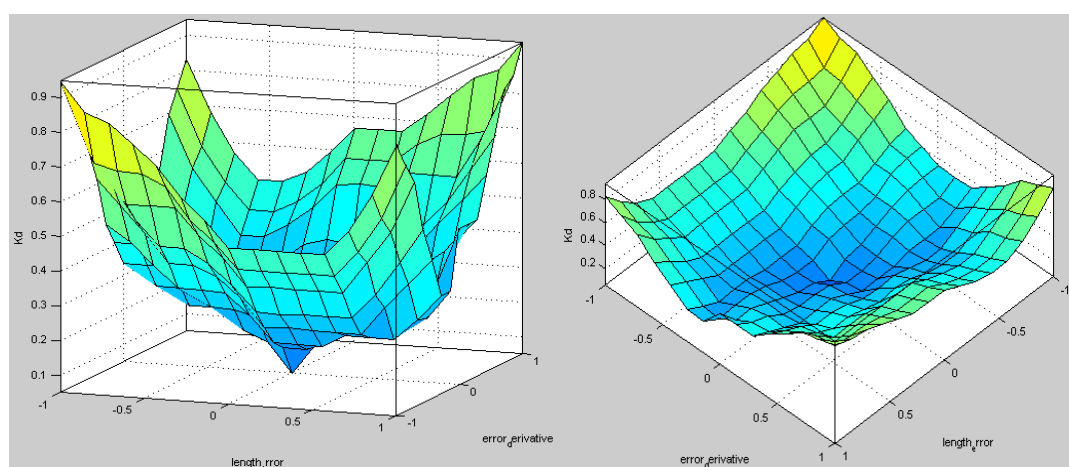


Figure 3.6: Control surface of fuzzy-PD controller representing the relation between inputs and output  $\lambda_{Kd}$ .

### 3.3 ANFIS controller

Generally speaking, There are two distinct methods for building controllers: fuzzy and neural. Often the choice of method is dictated by the data available on the plant involved. If the data are pairs of numbers, we may apply the neural method, and if the data are rules, fuzzy methods may be appropriate. Neural methods provide learning capability, whereas fuzzy methods provide flexible knowledge-representational capability (Nguyen *et al.*, 2003).

One of the limitations of fuzzy systems is the curse of dimensionality (Wesley, 1997). Furthermore, in the practical application, fuzzy control lacks an online self-study or self-adjustment ability for time-varying parameters and nonlinear systems, in order to obtain good control effects to these objectives, they must have better control rules. A neural network has a strong self-studying ability in a changing environment, but after learning, it cannot express the relationship of input and output data in an acceptable way. The Adaptive Neuro-Fuzzy Inference System combines these two theories and can achieve better control over complicated objectives (Wang *et al.*, 2009).

Integrating these two methodologies, in control in particular and in intelligent technologies in general, can lead to better technologies that take advantage of the strengths of each methodology and at the same time overcome some of the limitations of the individual techniques (Nguyen *et al.*, 2003).

An adaptive network, as the name indicates, is a network structure consisting of a number of nodes connected through directional links. Each node represents a process unit, and the links between nodes specify the causal relationship between the connected

nodes. All or part of the nodes are adaptive, which means the outputs of these nodes depend on modifiable parameters pertaining to these nodes (Jang *et al.*, 1997).

### 3.3.1 Learning and adaptation in fuzzy systems via a neural network

When experiential data exists, fuzzy systems can be trained to represent an input-output relationship. By using *gradient descent techniques*, fuzzy system parameters, such as identifying a rule's antecedent values (Left hand side) membership functions and identifying a rule's consequent values (right hand side) membership functions, and the connectives between layers in an adaptive network, can be optimized. The adaptation of fuzzy systems using neural network training methods has been proposed by various researchers (Wesley, 1997). Jang *et al.*, (1997) have introduced the adaptive network-based fuzzy inference system (ANFIS).

The ANFIS discriminates itself from normal fuzzy logic systems by the adaptive parameters, i.e. both *the premise parameters* and *consequent parameters* are adjustable. The most noteworthy feature of the ANFIS is its hybrid learning algorithm. The adaptation process of the parameters of the ANFIS is divided into two steps. For the first step of the consequent parameters training, the *least mean squares (LMS) method* is used because the output of the ANFIS is a linear combination of *the consequent parameters*. *The premise parameters* are fixed at this step. After the consequent parameters have been adjusted, the approximation error is back-propagated (BP) through every layer to update *the premise parameters* as the second step. This part of the adaptation procedure is based on *the gradient descent principle*, which is the same as in the training of the back propagation (BP) neural network (the back propagation algorithm is an optimization technique design to minimize an objective, e.g., squared error function). *The consequence parameters* identified by the LMS method are optimal in the sense of least squares under the condition that the premise parameters are fixed (Bachir and Zoubir, 2012). The training process stops whenever the designated epoch number is reached or the training error goal is achieved. A combination of such intelligent systems as ANFIS provides even better results than just neural networks or fuzzy control (Adhyaru *et al.*, 2010).

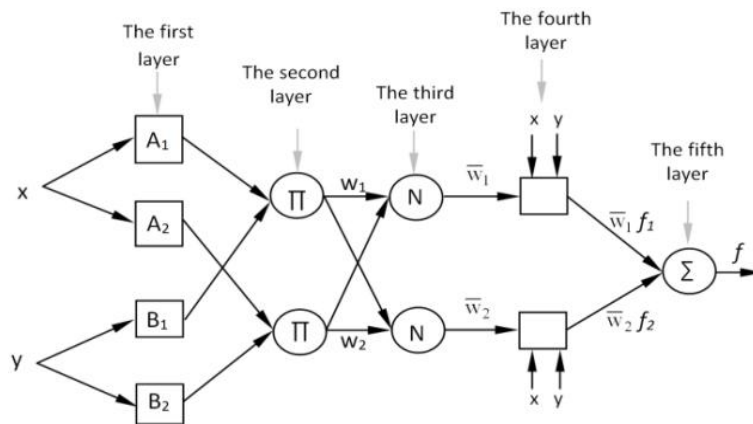


Figure 3.7: A typical architecture ANFIS structure.

To improve the reliability of the controller by the error minimization approach, twelve ANFIS networks are used in a parallel structure and embedded into the control system. In this implementation, after the off-line training, the output values of the gains  $K_p$  and  $K_d$  generated by the twelve ANFIS are applied to the inputs of the servo valves of each cylinder. The error vector is computed for each ANFIS by using the difference between the actual rod length generated by the dynamic model of the manipulator and the desired rod length. The results are evaluated to select the network generating the best result. The network is then assigned as the ANFIS controller for actual time steps, and its output is assigned as the servo valve input of the parallel-implemented ANFIS controller output driving the dynamic model of the manipulator as shown in Figure 3.8. Before the training of the network, the inputs and targets are scaled (normalized) so that they fall within a specified range, which can make the ANFIS training more efficient (Arpaci and Özgüven, 2011).

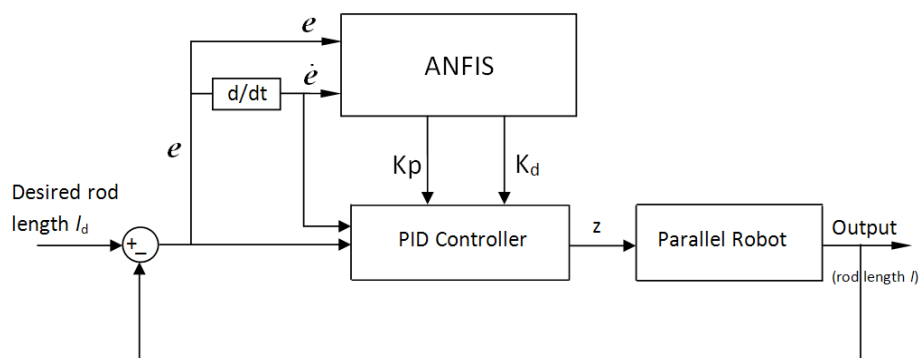


Figure 3.8: ANFIS PID controller implementation for parallel robot.

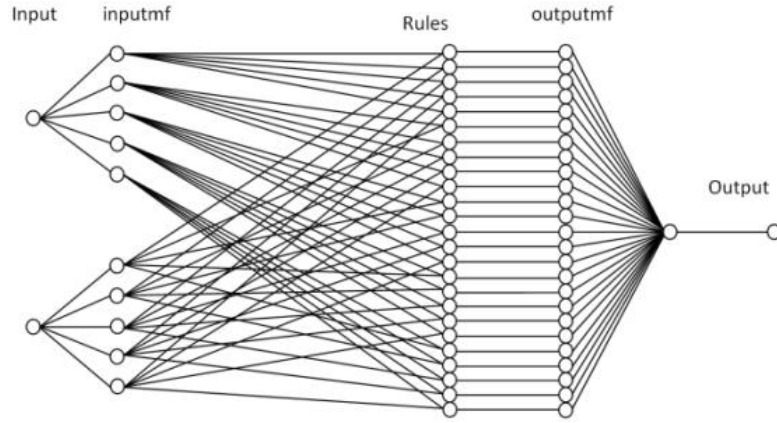


Figure 3.9: ANFIS structure for each cylinder controller.

The architecture of the ANFIS used in this chapter is shown in Figure 3.9. For simplicity, let us consider a typical architecture of ANFIS (Figure 3.7) with two inputs,  $x$  and  $y$ , and one output  $f$ . In the architecture, a circle indicates a fixed node, whereas a square indicates an adaptive node. Among the many FIS models, the Sugeno fuzzy model is the most widely applied one and the one used in this study due to its high interpretability, computational efficiency and built-in optimal and adaptive techniques. For each model, a common rule set with two fuzzy if-then rules can be expressed as (Jang *et al.*, 1997):

$$\text{Rule 1: If } x(=e) \text{ is } A_i \text{ and } y(=\dot{e}) \text{ is } B_i, \text{ then } f_i = p_i x + q_i y + r_i \quad (3.9)$$

where  $A_i$  and  $B_i$  are fuzzy sets in the antecedent and  $z = f(e, \dot{e})$  is a crisp function in the consequent.

The ANFIS controller generates continuous changes in the reference PID parameters  $K_p$  and  $K_d$  based on the  $i^{\text{th}}$  rod length error  $e$  and derivate of the error  $\dot{e}$ . The error is defined as  $e = l_d - l$ , where  $l_d$  and  $l$  are the reference and the actual length of the  $i^{\text{th}}$  rod of parallel robot, respectively. Each ANFIS consists of five layers as follows (Jang *et al.*, 1997):

**Layer 1:** Every node  $i$ , in this layer, is adaptive with a node function:

$$O_i^1 = \mu_{A_i}(e), i = 1, \dots, 5 \quad \text{or} \quad O_i^1 = \mu_{B_{i-5}}(\dot{e}), i = 6, \dots, 10 \quad (3.10)$$

$O_i^1$  is the output of the  $i^{\text{th}}$  node, i.e. the membership grade of a fuzzy set  $A(=A_i \text{ or } B_{i-5})$ . In this study, the node membership function is a generalized bell function:

$$\mu_{A_i}(x = e) = \frac{1}{1 + \left| \frac{x - c_i}{a_i} \right|^{2b_i}} \quad (3.11)$$

where  $x$  (or  $y$ ) is the input to the node  $i$ .  $\{ a_i, b_i, c_i \}$  is the *premise parameters* set.

**Layer 2:** The total number of rules is 25 in this layer. Each node output represents the activation level of a rule:

$$O_i^2 = w_i = \mu_{A_i}(e) \cdot \mu_{B_i}(\dot{e}), \quad i = 1, \dots, 5 \quad (3.12)$$

**Layer 3:** Fixed node  $i$ , in this layer, calculates the ratio of the  $i^{\text{th}}$  rule activation level (firing strengths) to the total of all activation levels; this layer is called normalized firing strengths:

$$O_i^3 = \bar{w}_i = \frac{w_i}{\sum_{i=1}^n w_i} \quad (3.13)$$

**Layer 4:** Adaptive node  $i$  in this layer calculates the contribution of the  $i^{\text{th}}$  rule towards the overall output, with the following node function:

$$O_i^4 = \bar{w}_i f_i = \bar{w}_i (p_i x + q_i y + r_i) = \bar{w}_i (p_i e + q_i \dot{e} + r_i) \quad (3.14)$$

where  $\bar{w}_i$  is the output of layer 3, and  $\{ p_i, q_i, r_i \}$  is the *consequent parameters* set.

**Layer 5:** The single node in this layer computes the overall output as the summation of all incoming signals, which is expressed as:

$$\text{overall output} = O_i^5 = \sum_{i=1}^n \bar{w}_i f_i = \frac{\sum_{i=1}^n w_i f_i}{\sum_{i=1}^n w_i} \quad (3.15)$$

The learning rule is the back propagation gradient descent, which calculates the error signals recursively from the output layer backward to the input nodes. The task of the learning algorithm for this architecture is to tune all the modifiable parameters to

make the ANFIS output match the training data. The overall output is a linear combination of the modifiable parameters.

The parameters to be trained are  $\{a_i, b_i, c_i\}$  of the premise parameters and  $\{p_i, q_i, r_i\}$  of the consequent parameters. The training algorithm requires a training set defined between inputs and outputs (Passino and Yurkovich, 1997). The input and output pattern sets have 50000 rows. Figure 3.14 shows the initial membership functions for the input error which are the same for each cylinder. Figure 3.15 (a, b, c, d, e and f) show final optimized membership functions (MF) for  $e$  and  $\dot{e}$  after training for each cylinder controller. Figure 3.9 shows the ANFIS model structure. The number of epochs was 100 for training. The number of MFs for both input variables  $e$  and  $\dot{e}$  is 5, respectively. The number of rules is then  $25(5 \times 5=25)$ . The generalized bell (Cauchy) MF is used for each input variable. It is clear from Equation (3.11) that the bell MF is specified by three parameters. Therefore, the ANFIS used here contains a total of 105 fitting parameters, of which 30 ( $5 \times 3 + 5 \times 3=30$ ) are the premise parameters and 75 ( $3 \times 25=75$ ) are the consequent parameters for each cylinder controller (AL-Saedi *et al.*, 2014).

### 3.3.2 ANFIS algorithm and structure:

In Fuzzy Control Toolbox, a useful command called *anfis* exists. This provides an optimization scheme to find the parameters in the fuzzy system that best fit the data. It is explained in the Toolbox manual that since some optimization algorithms require computation of the gradient, this is done with a neural network.

There are twelve data sets for the entire parallel robot, and therefore, we have twelve ANFIS networks. In order to predict the gains, the networks have to be trained with a set of input-output data. Consequently, there are two sets of training data for each arm. In the first set, the inputs are [the error ( $e$ ), the error derivative is ( $\dot{e}$ )], and the output is the derivative gain, while in the second set, the inputs are [the error ( $e$ ), the error derivative is ( $\dot{e}$ )], and the output is the proportional gain.

It is not clear at the beginning what the initial fuzzy system should be, that is, the type and number of membership functions. In such cases, the command *genfis1* can be used. This command will go over the data in a crude way and find a good starting system. In summary, *genfis1* is used to generate an initial fuzzy inference system FIS, and *anfis* to generate the best FIS system. ANFIS uses the result from *genfis1* to start optimization, as can be seen in Figure 3.10, and the most important MATLAB<sup>TM</sup> commands which have been used are shown in Figures 3.11, 3.12, and 3.13.

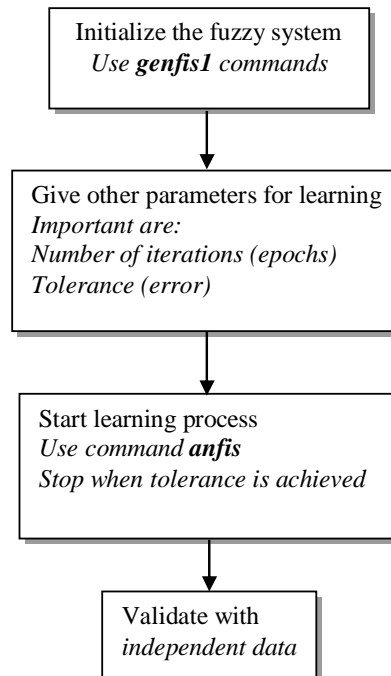


Figure 3.10: Basic flow diagram of computation in ANFIS.

Finally, the output (or the trained data after the checking process) should be sent to the PID controller so as to simulate the dynamic model of the parallel robot with these optimized gains ( $K_{p\_ANFIS-PD}$  and  $K_{d\_ANFIS-PD}$ ) rather than the old gains ( $K_p$  and  $K_d$ ).

```

data1=[e_1 e_dot_1 Kp_1];
data2=[e_2 e_dot_2 Kp_2];
data3=[e_3 e_dot_3 Kp_3];
data4=[e_4 e_dot_4 Kp_4];
data5=[e_5 e_dot_5 Kp_5];
data6=[e_6 e_dot_6 Kp_6];

% The fuzzy system is initialized with the command genfis1
nu=5; mftype='gbellmf';
% fismat=genfis1(trndata, nu, mftype);
fismat1=genfis1(data1, nu, mftype);
fismat2=genfis1(data2, nu, mftype);
fismat3=genfis1(data3, nu, mftype);
fismat4=genfis1(data4, nu, mftype);
fismat5=genfis1(data5, nu, mftype);
fismat6=genfis1(data6, nu, mftype);

```

Figure 3.11: Implementation of the **genfis1** function in MATLAB for the ANFIS technique for a parallel robot.

```

% Next apply anfis-command to find the best FIS system- max number of
% iterations = 100
numep=100;
% [parab, trnerr, ss, parabcheck, chkerr] = anfis(trndata, fismat, numep,[],chkdata);
[parab1, trnerr1, ss1] = anfis(data1, fismat1, numep, []);
[parab2, trnerr2, ss2] = anfis(data2, fismat2, numep, []);
[parab3, trnerr3, ss3] = anfis(data3, fismat3, numep, []);
[parab4, trnerr4, ss4] = anfis(data4, fismat4, numep, []);
[parab5, trnerr5, ss5] = anfis(data5, fismat5, numep, []);
[parab6, trnerr6, ss6] = anfis(data6, fismat6, numep, []);

```

Figure 3.12: Implementation of the **anfis** function in MATLAB for the ANFIS technique for a parallel robot.



```

xzh1=[e_1 e_dot_1];
xzh2=[e_2 e_dot_2];
xzh3=[e_3 e_dot_3];
xzh4=[e_4 e_dot_4];
xzh5=[e_5 e_dot_5];
xzh6=[e_6 e_dot_6];

anfi1=evalfis(xzh1,parab1);
anfi2=evalfis(xzh2,parab2);
anfi3=evalfis(xzh3,parab3);
anfi4=evalfis(xzh4,parab4);
anfi5=evalfis(xzh5,parab5);
anfi6=evalfis(xzh6,parab6);

```

Figure 3.13: Implementation of the **evalfis** function in MATLAB for the ANFIS technique for a parallel robot.

### 3.4 Robot parameters, simulation results and discussion

The actual values of the system parameters of the hybrid robot of each element are tabulated in Table 3.2. The local position of the universal joint in the base plate and the local position of the spherical joint in the moving plate are given. Initially, the tip of each rod is located 0.35 m from the cylinder outlet. Young's modulus is  $2.07 \times 10^{11} \text{ N/m}^2$ , rod density  $\rho$  is  $7801 \text{ kg/m}^3$ , the rod radius is 0.015 m, and the length is 0.668 m. All six rods are considered as having a uniform mass distribution and cross-section. Each of the rods is divided into six elements.

Table 3.2: Mass and Inertia properties of parallel Robot's elements.

element	Mass (Kg)	Izz =Iyy (Kg m <sup>2</sup> )	Ixx (Kg m <sup>2</sup> )	Ixy (Kg m <sup>2</sup> )
cylinder	4.589	0.2160	2.89683e-3	0
rod_piston	3.683	0.1372	4.14392e-4	0
moving plate	28.92	0.1867	0.3622	0

Base points (local):  $[0.1658\cos(120(1-i)+(90\pm 14.851)) \quad 0.1658\sin(120(1-i)+(90\pm 14.851)) \quad 0]$ ,  $i = 1, 2, 3$ . End effector points (local):  $[0.1296 \cos(120(1-i)+(90\pm 45.485)) \quad 0.1296 \sin(120(1-i)+(90\pm 45.485)) \quad 0]$ ,  $i = 1, 2, 3$ .

The moving plate (end effector) tracks a trajectory of  $x = 0$ ,  $y = -0.1t \cos(42.87)$ , and  $z = +0.1t \sin(42.87)$  with machining forces. The machining forces were  $F_x = -1000\sin(2\pi ft)$ ,  $F_y = 700\sin(2\pi ft)$ , and  $F_z = -600\sin(2\pi ft)$ , with  $f = 20 \text{ Hz}$ .

Three different controllers are implemented for computer simulation. The first one is the PID controller. The second is the fuzzy logic for tuning the gains of the PID controller (to find the optimal values) based on the expert's experience, where  $K_{d_{Max}} = \text{diag}(3000, 3000, 3000, 3000, 3000, 3000)$ ,  $K_{d_{Min}} = \text{diag}(1000, 1000, 1000, 1000, 1000, 1000)$ ,  $K_{p_{Max}} = \text{diag}(2.5, 2.5, 2.5, 2.5, 2.5, 2.5)$ , and  $K_{p_{Min}} = \text{diag}(0.5, 0.5, 0.5, 0.5, 0.5, 0.5)$ . In the third, the parallel-implemented ANFIS technique is used for tuning the PID gains using the input-output data from the fuzzy-PID as training data for each actuator for tracking the trajectory. For the simulations, a sampling period of 0.05 ms is chosen. Consequently, 50000 steps are included in every control simulation.

Figure 3.14 represents the initial membership functions for the error  $e$  for each cylinder by the ANFIS method. Figure 3.15 (a, b, c, d, e and f) represents the final (post-training) membership functions for the error  $e$  for cylinders a, b, c, d, e and f by the ANFIS method, respectively. In Figures 3.16, and 3.17, it can be shown that the PID gains ( $K_p$  and  $K_d$ ) in both cases of ANFIS and fuzzy tuning are not constant during the simulation, as in the case of only the PID controller. The differences in the pressures between the two chambers of each cylinder, which can be seen in Figure 3.18, are drawn to compare the PID controller method and the ANFIS PD tuning method, indicating that the actual values for pressure differences both remain within the pressure difference limit. It can be inferred from Figures 3.19 and 3.20 that the end effector tracks the desired trajectory in both directions  $y$  and  $z$  comparatively better with the ANFIS-PID controller since the control parameters  $K_p$  and  $K_d$  can be adjusted precisely through the ANFIS network's learning. All of the results demonstrate that the ANFIS-PD control is better than fuzzy-PD and more effective than the conventional PID controller.

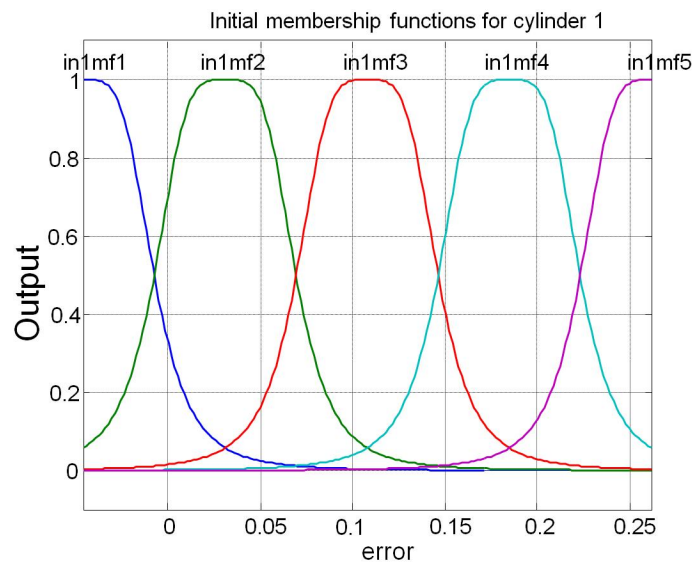


Figure 3.14: Initial membership function MFs for the input error for each cylinder.

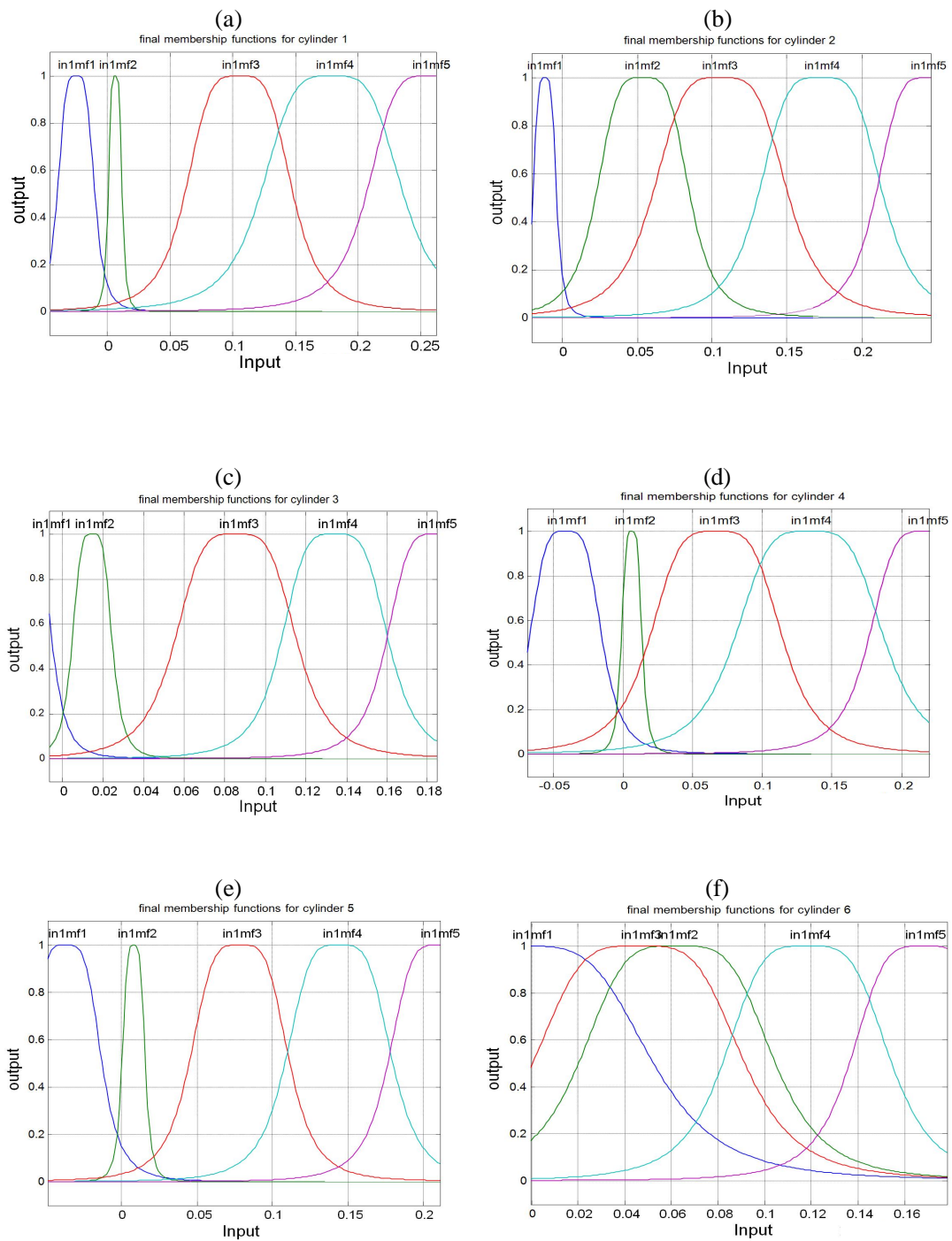


Figure 3.15: Final (post-training) membership function MFs for the input error of cylinders (a), (b), (c), (d), (e), (f).

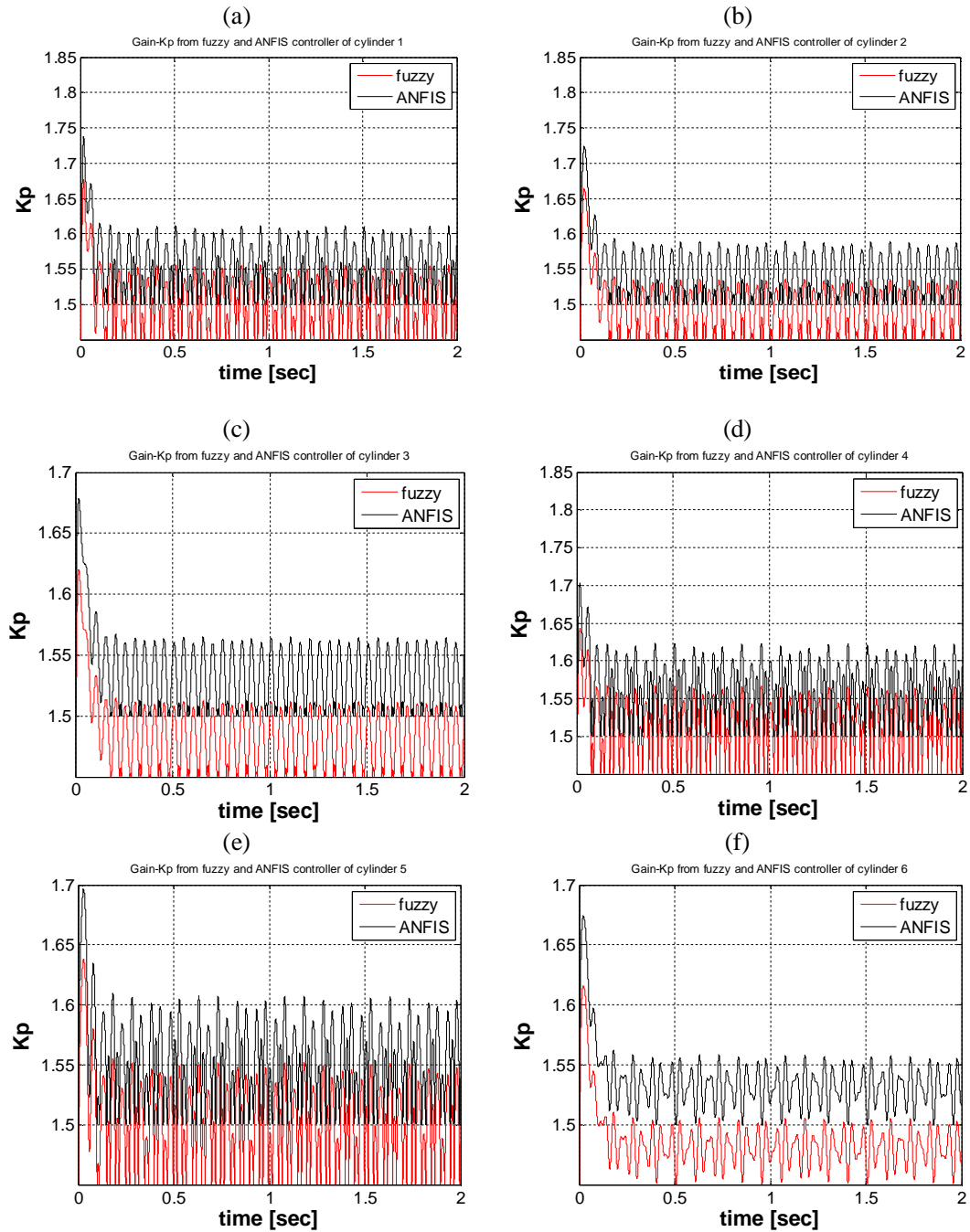


Figure 3.16: Comparison between  $K_p$  gains for a PID controller with the fuzzy and ANFIS tuning methods: (a)  $K_p$  of cylinder a, (b)  $K_p$  of cylinder b, (c)  $K_p$  of cylinder c, (d)  $K_p$  of cylinder d, (e)  $K_p$  of cylinder e, and (f)  $K_p$  of cylinder f.

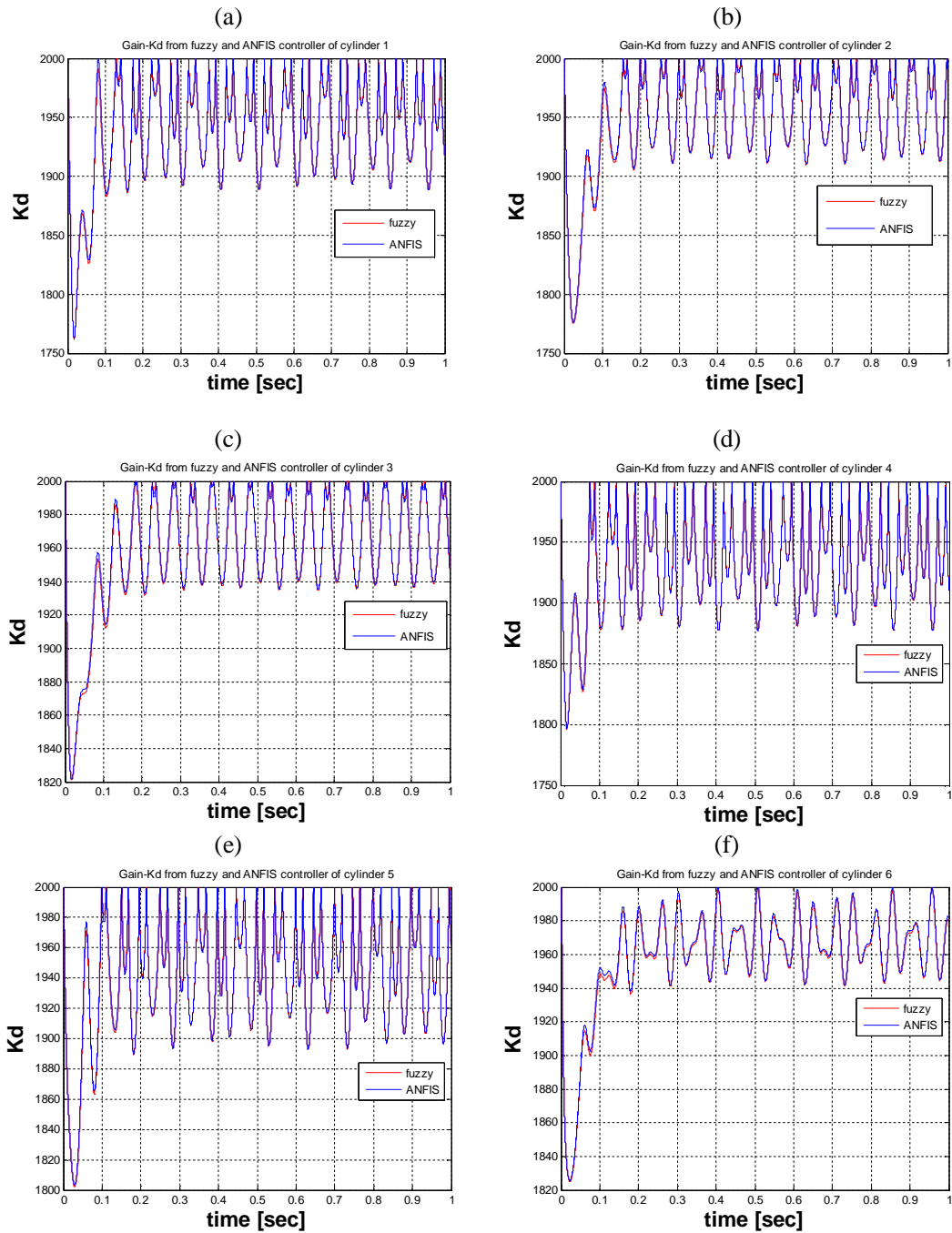


Figure 3.17: Comparison between the  $K_d$  gain for a PID controller with the fuzzy and ANFIS tuning methods: (a)  $K_d$  of cylinder a, (b)  $K_d$  of cylinder b, (c)  $K_d$  of cylinder c, (d)  $K_d$  of cylinder d, (e)  $K_d$  of cylinder e and (f)  $K_d$  of cylinder f.

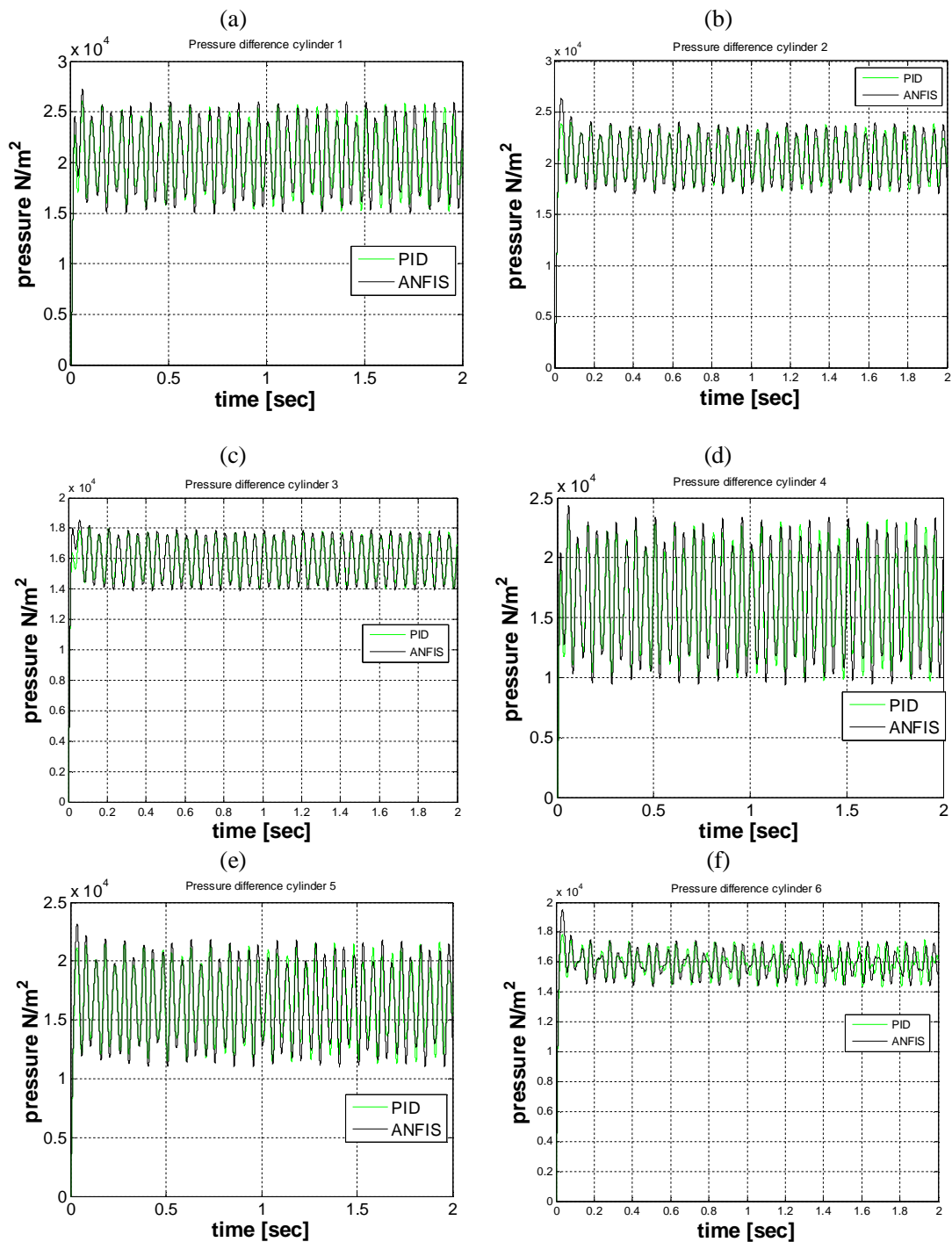


Figure 3.18: Comparison between the difference in the pressures resulting from a conventional PID controller and the ANFIS tuning method in the cylinders (a), (b), (c), (d), (e), and (f).

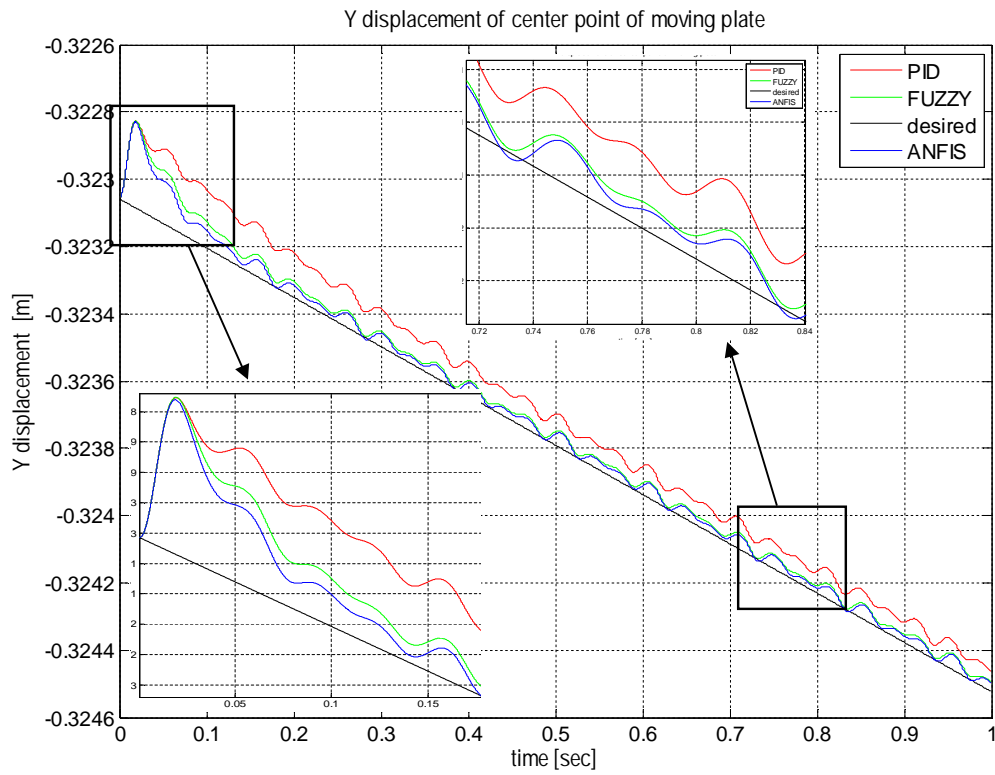


Figure 3.19: Y-displacement of moving plate (end effector) under the effect of machining forces.

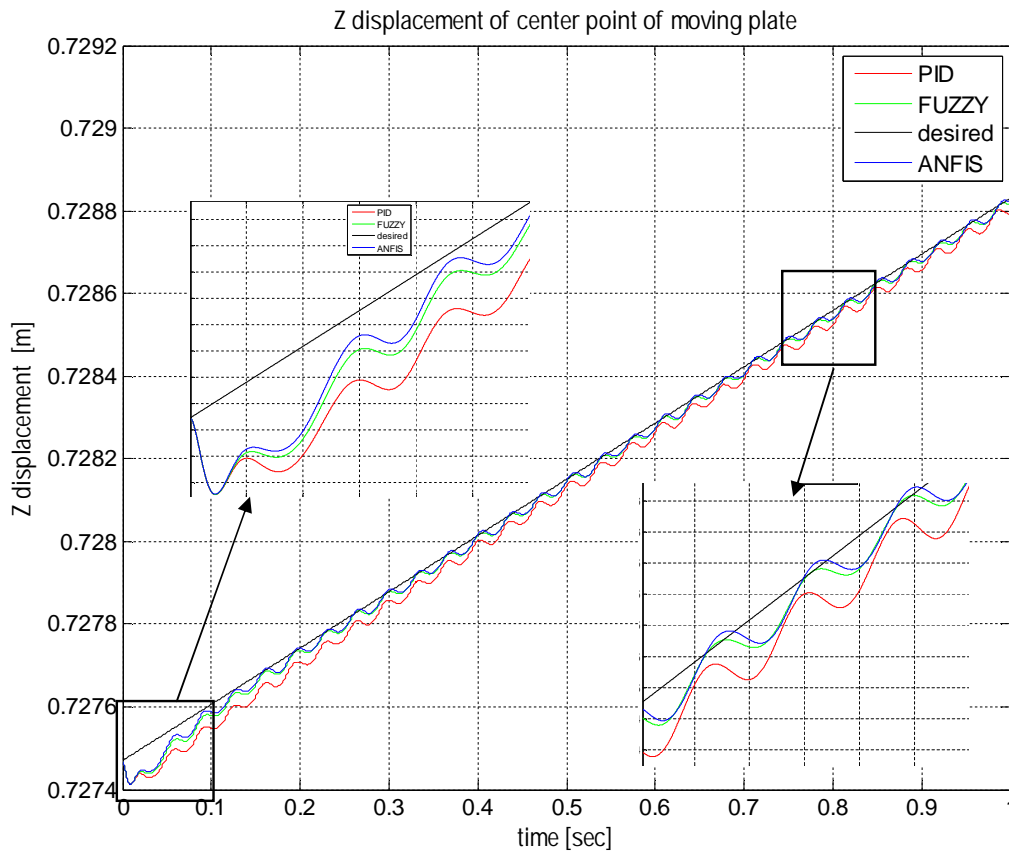


Figure 3.20: Z-displacement of moving plate (end effector) under the effect of machining forces.

### 3.5 Analysis of the serial part of the hybrid robot

The analysis of the serial component of the hybrid robot in chapter 2 using the equilibrium of reaction forces at the universal joint connections of the hexa-element (Figures 2.13 and 2.14) can be repeated here using the results achieved by both proposed controllers, Fuzzy-PD and ANFIS-PD. Having found the components of the global reaction forces at the universal joints, the resultant of the forces in the local coordinate system of the serial robot cylinder can be found (Figures 2.13 and 2.14), and



a PID control system can be designed to estimate the correct value of the effecting force on the serial part. The hydraulic servo valve of the serial part control is similar to that used in the parallel robot, i.e. Moog Type-30.

Figure 2.15 illustrates the PID control of the serial robot where the input is the resultant reaction forces, and the output is the required locked position of the cylinder.

It can be seen in Figure 3.21 that the serial mechanism can be locked at  $5 \times 10^{-5}$  m with less overshoot and a faster rise time due to resultant forces. This is achieved by ANFIS-PD self-tuning method instead of the fuzzy-PD self-tuning method. At the same time, the displacements with forces which can be achieved by the fuzzy-PD self-tuning method are better than the displacement which can be achieved due to the forces by the normal PID control method only. Clearly exam to the resultant forces in Figure 3.22 which is achieved by ANFIS-PD self-tuning method is less comparatively and therefore better than the other methods, meanwhile, the resultant forces which is achieved by Fuzzy-PD self-tuning method is less comparatively to PID control method therefore it is better.

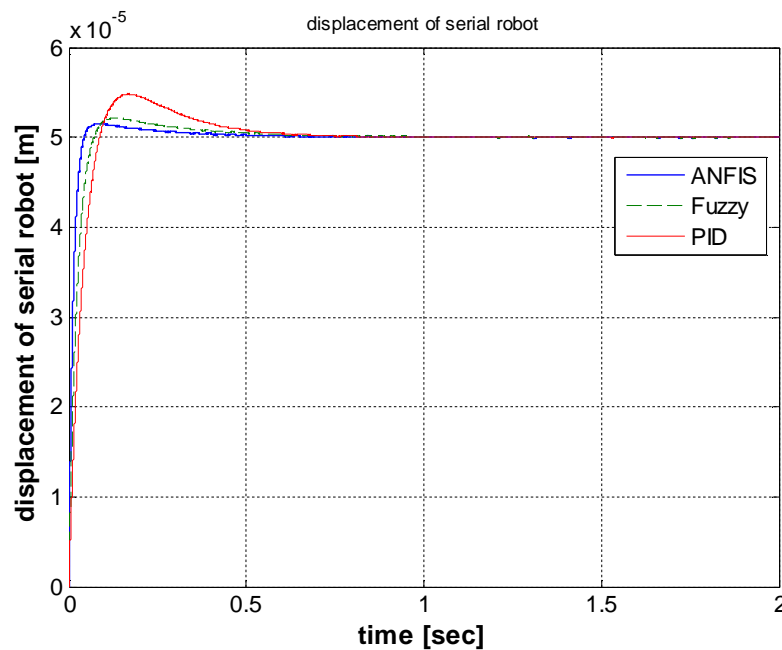


Figure 3.21: Required (locked) displacement of the rod of a serial robot cylinder.

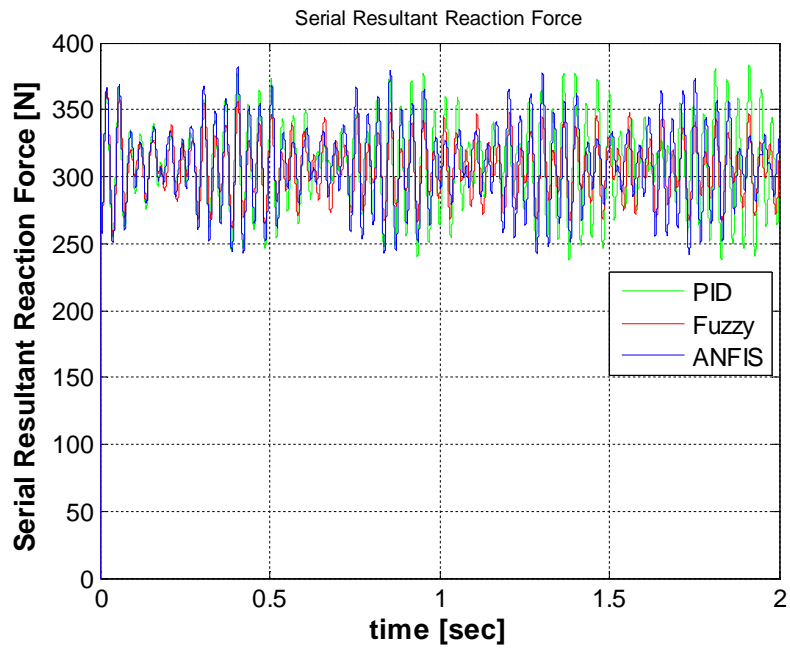


Figure 3.22: Total force at the serial cylinder of the rod of a serial robot cylinder.

## 4 Special Euclidean group for flexible multibody dynamics of a hydraulically driven parallel mechanism

### 4.1 Fundamentals of the Special Euclidean group, $SE(3)$

The concepts introduced in this work are extensively based on Lie group literature (see e.g. Murray *et al.*, 1994, Boothby, 1986, Spivak, 1999, Sonnevile and Brüls, 2014, Park and Chung, 2008, Arnold, 1989). A group  $G$  is a set of elements with a composition rule that associates an element of the group to two element of the group: if  $q_1, q_2 \in G$ , then  $q_1 \circ q_2 \in G$ . In a matrix Lie group, the elements are matrices and the composition rule is the matrix product written as  $q_1 q_2 = q_3$ , and the identity matrix  $e$  ( $\forall q \in G : qe = eq = q$ , and  $qq^{-1} = q^{-1}q = e$ ).

The matrix Lie group  $SE(3)$  is the group of homogenous transformations  $\mathbf{H} = H(\mathbf{R}, \mathbf{x})$  combining a rotation matrix  $\mathbf{R} \in SO(3)$  (the Special Orthogonal which is defined as the set of  $3 \times 3$  matrices such that  $\mathbf{R}^T \mathbf{R} = \mathbf{I}_{3 \times 3}$ ,  $\det(\mathbf{R}) = +1$ ), and a position vector  $\mathbf{x} \in \mathbb{R}^3$ . Considering that  $\mathbf{x}$  is a position or displacement vector and  $\mathbf{R}$  that a rotation matrix  $\mathbf{R}$  defines an orientation,  $SE(3)$  elements represent frames. Similarly to the Special Orthogonal group  $SO(3)$ ,  $SE(3)$  is not a vector space.

Elements of the special Euclidean group  $SE(3)$  can be represented by  $4 \times 4$  matrices

$$\mathbf{H} = \begin{bmatrix} \mathbf{R} & \mathbf{x} \\ \mathbf{0}_{1 \times 3} & 1 \end{bmatrix} \quad (4.1)$$

The composition rule, namely the matrix product of two such  $4 \times 4$  matrices, reads

$$\mathbf{H}_3 = H(\mathbf{R}_3, \mathbf{x}_3) = \mathbf{H}_1 \mathbf{H}_2 = H(\mathbf{R}_1 \mathbf{R}_2, \mathbf{R}_1 \mathbf{x}_2 + \mathbf{x}_1) \quad (4.2)$$

where it is interesting to notice that  $\mathbf{x}_3$  involves  $\mathbf{R}_1$  as well as  $\mathbf{x}_1$  and  $\mathbf{x}_2$ . Geometrically speaking,  $\mathbf{H}_3$  is thus interpreted as the result of the frame transformation  $\mathbf{H}_2$  from a frame defined by  $\mathbf{H}_1$ . The neutral element for this matrix product is the  $4 \times 4$  identity matrix  $\mathbf{I}_{4 \times 4}$  and the inverse of  $\mathbf{H} \in SE(3)$ ,  $\mathbf{H}^{-1} \in SE(3)$ , is given by  $\mathbf{H}^{-1} = H(\mathbf{R}^T, -\mathbf{R}^T \mathbf{x})$ , i.e.

$$\mathbf{H}^{-1} = \begin{bmatrix} \mathbf{R}^T & -\mathbf{R}^T \mathbf{x} \\ \mathbf{0}_{1 \times 3} & 1 \end{bmatrix} \quad (4.3)$$

Derivatives of  $SE(3)$  can be introduced by left invariant vector fields

$$d(\mathbf{H}) = \mathbf{H}\tilde{\mathbf{h}} \quad (4.4)$$

where the  $4 \times 4$  matrix  $\tilde{\mathbf{h}}$  belongs to  $\mathfrak{se}(3)$ , the Lie algebra of  $SE(3)$ .  $\mathfrak{se}(3)$  is  $\mathbb{R}^6$ , which means that  $\tilde{\cdot}$  is an invertible linear map from  $\mathbb{R}^6$  to  $\mathfrak{se}(3)$  such that

$$\mathbf{h} = \begin{bmatrix} \mathbf{h}_U \\ \mathbf{h}_\Omega \end{bmatrix} \in \mathbb{R}^6 \quad \text{and} \quad \tilde{\mathbf{h}} = \begin{bmatrix} \tilde{\mathbf{h}}_\Omega & \mathbf{h}_U \\ \mathbf{0}_{1 \times 3} & 0 \end{bmatrix} \in \mathfrak{se}(3) \quad (4.5)$$

where  $\mathbf{h}_U \in \mathbb{R}^3$  and  $\tilde{\mathbf{h}}_\Omega \in \mathfrak{so}(3)$ , the Lie algebra of the Special Orthogonal group  $SO(3)$ , which is the set of skew-symmetric matrices built upon the three components of  $\mathbf{h}_\Omega \in \mathbb{R}^3$ .

$$\tilde{\mathbf{h}}_\Omega = \begin{bmatrix} 0 & -\mathbf{h}_{\Omega 3} & \mathbf{h}_{\Omega 2} \\ \mathbf{h}_{\Omega 3} & 0 & -\mathbf{h}_{\Omega 1} \\ -\mathbf{h}_{\Omega 2} & \mathbf{h}_{\Omega 1} & 0 \end{bmatrix} \in \mathfrak{so}(3) \quad (4.6)$$

It is clear from the argument whether the tilde operator denotes the mapping to  $\mathfrak{so}(3)$  or  $\mathfrak{se}(3)$ . From Equation (4.4), we have

$$d(\mathbf{x}) = \mathbf{R}\mathbf{h}_U \quad \text{and} \quad d(\mathbf{R}) = \mathbf{R}\tilde{\mathbf{h}}_\Omega \quad (4.7)$$

where it is important to notice that both derivatives involve a rotation matrix of the frame. Hence, the derivatives are interpreted as taking place in the frame described by  $\mathbf{H}$ .

### The exponential map

The exponential map defines a mapping between the Lie algebra  $\mathfrak{g}$  (the tangent space at the identity) and the Lie group  $G$ , which induces a valid local parameterization around the identity or around any point  $q_n$  (see Figure 4.1). Thus, an equivalent update procedure is furnished by

$$q_{n+1}(\xi) = q_n \exp(\tilde{\xi}_{n+1}) \quad (4.8)$$

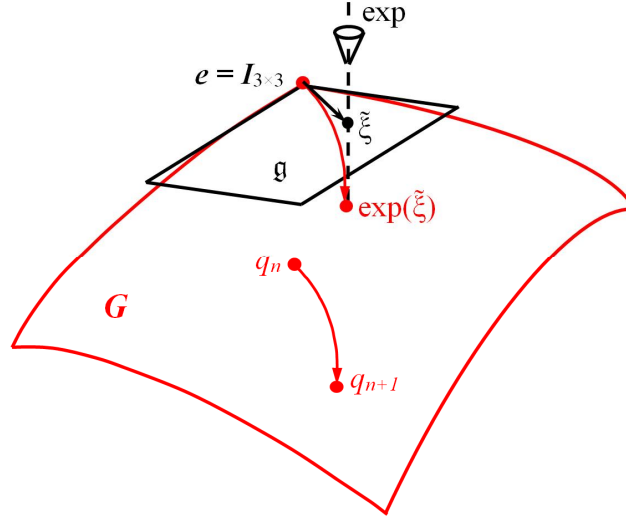


Figure 4.1: Geometric interpretation of the exponential map.

Starting from a given six-dimensional vector  $\mathbf{n} = [\mathbf{n}_U^T \quad \mathbf{n}_\Omega^T]^T$ , an  $SE(3)$  element can be built using the so-called exponential map which is defined as

$$\exp_{SE(3)}(\mathbf{n}) = \sum_{i=0}^{\infty} \frac{\tilde{\mathbf{n}}^i}{i!} \quad (4.9)$$

The exponential map may be seen as a local parameterization in the sense that the argument of the exponential map belongs to a linear space while  $SE(3)$  is a non-linear space. In practice, this means that standard vector calculus applies to the argument of the exponential map, such as the multiplication by a scalar or the addition of another six-dimensional vector and that its effect can be projected onto the group. Exploiting the Lie algebra structure, it can be expressed in a closed form as

$$\exp_{SE(3)}(\mathbf{n}) = \begin{bmatrix} \exp_{SO(3)}(\mathbf{n}_\Omega) & \mathbf{T}_{SO(3)}^T(\mathbf{n}_\Omega) \mathbf{n}_U \\ \mathbf{0}_{3 \times 1} & 1 \end{bmatrix} \quad (4.10)$$

where, using  $a = \sin(\|\mathbf{n}_\Omega\|) / \|\mathbf{n}_\Omega\|$  and  $b = 2(1 - \cos(\|\mathbf{n}_\Omega\|)) / \|\mathbf{n}_\Omega\|^2$ ,

$$\exp_{SO(3)}(\mathbf{n}_\Omega) = \mathbf{I}_{3 \times 3} + a \tilde{\mathbf{n}}_\Omega + \frac{b}{2} \tilde{\mathbf{n}}_\Omega^2 \quad (4.11)$$

and

$$\mathbf{T}_{SO(3)}(\mathbf{n}_\Omega) = \mathbf{I}_{3 \times 3} - \frac{b}{2} \tilde{\mathbf{n}}_\Omega + \frac{1-a}{\|\mathbf{n}_\Omega\|^2} \tilde{\mathbf{n}}_\Omega^2 \quad (4.12)$$

where  $\exp_{SO(3)}$  is the exponential map of the Special Orthogonal group, and  $\mathbf{T}_{SO(3)}$  is the tangent operator of the special Orthogonal group.

The inverse map of the exponential map is called the logarithmic map. It returns a  $se(3)$  element from a given  $SE(3)$  element. It is explicitly given as

$$\log_{SE(3)}(H(\mathbf{R}, \mathbf{x})) = \begin{bmatrix} \tilde{\omega}(\mathbf{R}) & \mathbf{T}_{SO(3)}^{-T}(\omega) \mathbf{x} \\ \mathbf{0}_{1 \times 3} & 0 \end{bmatrix} \quad (4.13)$$

where the skew-symmetric matrix  $\tilde{\omega} \in se(3)$  is defined as

$$\tilde{\omega} = \log_{SO(3)}(\mathbf{R}) = \frac{\theta}{2\sin(\theta)} (\mathbf{R} - \mathbf{R}^T) \quad (4.14)$$

with  $\theta = \arccos\left(\frac{1}{2}(\text{trace}(\mathbf{R}) - 1)\right)$ ,  $|\theta| < \pi$ .

The derivative of the exponential map introduces the so-called tangent operator  $\mathbf{T}_{SE(3)}$ . Consider the transformation from  $\mathbf{H}_0$  to  $\mathbf{H}$  as

$$\mathbf{H} = \mathbf{H}_0 \exp_{SE(3)}(\mathbf{n}) \quad (4.15)$$

The derivative of  $\mathbf{H}$  leads to

$$d(\mathbf{H}) = \mathbf{H}_0 D\exp(\mathbf{n})d(\tilde{\mathbf{n}}) = \mathbf{H} \exp_{SE(3)}^{-1}(\mathbf{n}) D\exp(\mathbf{n})d(\tilde{\mathbf{n}}) \quad (4.16)$$

where  $D\exp$  is the derivative of the exponential map, and this can be written as

$$d(\mathbf{H}) = \mathbf{H} (\mathbf{T}_{SE(3)}(\mathbf{n})d(\mathbf{n})) \quad (4.17)$$

and  $\mathbf{T}_{SE(3)}$  can be written as

$$\mathbf{T}_{SE(3)}(\mathbf{n}) = \begin{bmatrix} \mathbf{T}_{SO(3)}(\mathbf{n}_\Omega) & \mathbf{T}_{U\Omega^+}(\mathbf{n}_U, \mathbf{n}_\Omega) \\ \mathbf{0}_{3 \times 3} & \mathbf{T}_{SO(3)}(\mathbf{n}_\Omega) \end{bmatrix} \quad (4.18)$$

where  $\mathbf{T}_{SO(3)}$ , the derivative of the exponential map on  $SO(3)$ , was given in Equation (4.12) and  $\mathbf{T}_{U\Omega^+}(\mathbf{n}_U, \mathbf{n}_\Omega)$  reads

$$\frac{-b}{2} \tilde{\mathbf{n}}_U + \frac{1-a}{\|\mathbf{n}_\Omega\|^2} (\tilde{\mathbf{n}}_U \tilde{\mathbf{n}}_\Omega + \tilde{\mathbf{n}}_\Omega \tilde{\mathbf{n}}_U) + \frac{\mathbf{n}_\Omega^T \mathbf{n}_U}{\|\mathbf{n}_\Omega\|^2} ((b-a) \tilde{\mathbf{n}}_\Omega + (\frac{b}{2} - \frac{3(1-a)}{\|\mathbf{n}_\Omega\|^2}) \tilde{\mathbf{n}}_\Omega^2) \quad (4.19)$$

with  $a$  and  $b$  defined for Equation (4.11). Notice that  $\mathbf{T}_{U\Omega^+}(\mathbf{n}_U, \mathbf{0}) = -\tilde{\mathbf{n}}_U/2$ . Using the notation  $d(\mathbf{H}) = \mathbf{H}\tilde{\mathbf{h}}$ , one has

$$\mathbf{h} = \mathbf{T}_{SE(3)}(\mathbf{n}) d(\mathbf{n}) \quad (4.20)$$

which relates the derivatives of  $\mathbf{H}$ , namely  $\mathbf{h}$ , and the derivative of  $\mathbf{n}$  which is used in the representation of  $\mathbf{H}$  as  $\mathbf{H} = \mathbf{H}_0 \exp_{SE(3)}(\mathbf{n})$ .

## 4.2 General description of multibody systems

In the present formulation, multibody systems are modeled using nodal absolute variables and kinematic joint relative transformations. Nodes at the mass center of each rigid body of the system are identified as A, A', A'' in Figure 4.2. Using the rigid body assumption, the inertia forces of each body are expressed as a function of the nodal variables located at the mass center of the body. Then, additional nodes are introduced to allow the description of the multibody system by specifying further constraints. For instance, in Figure 4.2, nodes B and B' are used for boundary conditions and nodes C and C' are used to formulate a kinematic joint between the two related bodies. The additional nodes are also linked to the mass center of the body by rigid constraints. In order to describe the restricted relative motion allowed by the kinematic joints, kinematic joint transformations are introduced in addition to the nodal variables (Sonneville and Bruls 2014).

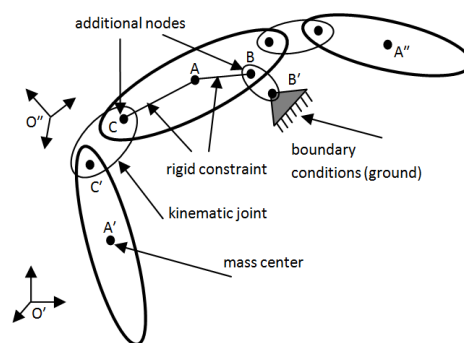


Figure 4.2: Representation of the nodes and the relationships involved in the finite element approach of multibody systems.

### 4.3 Modeling of constraints

The following constraints are derived in this chapter for the modeling of the parallel robot. Each cylinder is constrained to the fixed plate using a universal joint. The flexible rod is constrained to slide inside a rigid hydraulic cylinder using two changing contact points  $P^A$  and  $P^B$  (see Figure 4.3). Consequently, this mechanism can be modeled using one flexible sliding joint at the location of each node at  $P^A$ , and a translational joint at the location of each node at  $P^B$  along the sliding axle. The contact point  $P^A$  can be found by interpolating between the neighboring nodes of each flexible rod for each time step. A spherical joint constraint connects the final tip of each flexible rod to the rigid moving plate (end effector).

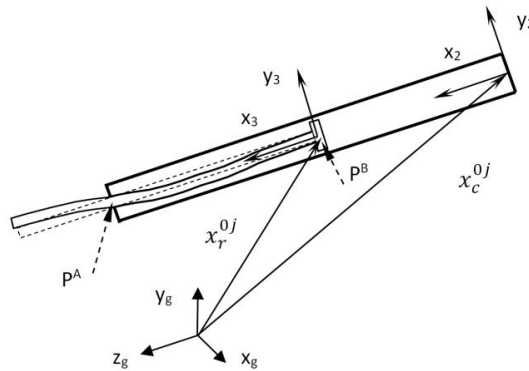


Figure 4.3: Deflection of a flexible rod sliding inside a rigid cylinder

#### 4.3.1 Kinematic of joint description

In the present work, multibody systems are modeled using nodal absolute variables and kinematic joint relative transformations, leading to a mixed coordinate formulation. This framework thus relies on redundant variables which are related by algebraic constraints. Although the number of variables is higher than in a minimal coordinate formulation, the equilibrium equations are obtained straightforwardly due to the systematic finite element assembly procedure.

The nodal variables and the kinematic joint transformations are material frames which belong to the Special Euclidean group  $SE(3)$  and can be represented as  $4 \times 4$  homogenous transformation matrices  $\mathbf{H}$ . For the nodal values, denoted as  $\mathbf{H}_I$  for the node of index  $I$ , the rotation matrix and the position vector describe the orientation and position of the node with respect to the inertia frame while for kinematic joint transformations, denoted as  $\mathbf{H}_{J,I}$  for the joint of index  $I$ , they represent the relative rotation and relative displacement inside the joint.



The derivatives on the Lie group  $SE(3)$  are related to the Lie algebra  $se(3)$ , which is a six-dimensional vector space. Accordingly, velocities can be introduced as (Sonneville and Brüls, 2014)

$$(\mathbf{H}_I)^\dot{=} = \mathbf{H}_I \tilde{\mathbf{v}}_I \quad (4.21)$$

where  $\tilde{\cdot}$  is a linear mapping of the six-dimensional vector  $\mathbf{v}_I = \begin{bmatrix} \mathbf{v}_{I,U}^T & \mathbf{v}_{I,\Omega}^T \end{bmatrix}$  as

$$\tilde{\mathbf{v}}_I = \begin{bmatrix} \tilde{\mathbf{v}}_{I,\Omega} & \mathbf{v}_{I,U} \\ \mathbf{0}_{1 \times 3} & 0 \end{bmatrix} \quad (4.22)$$

where  $\tilde{\mathbf{v}}_{I,\Omega}$  is the skew-symmetric matrix formed by the three components of  $\mathbf{v}_{I,\Omega}$ . One may say that the  $3 \times 1$  vector  $\mathbf{v}_{I,U}$  and  $3 \times 1$  vector  $\mathbf{v}_{I,\Omega}$  are the translation and the rotation part of  $\mathbf{v}_I$ , respectively.

Due to the restricted relative motion that the joints impose, the kinematic joint transformation usually belongs to a subgroup of  $SE(3)$ . Hence, for a joint  $I$ , its time derivative takes the form  $(\mathbf{H}_{J,I})^\dot{=} = \mathbf{H}_{J,I} \tilde{\mathbf{v}}_{J,I}$ , where the following relationship holds:

$$\mathbf{v}_{J,I} = \mathbf{A}_I \mathbf{v}_{j,I} \quad (4.23)$$

In these equations,  $\mathbf{v}_{J,I}$  is a  $6 \times 1$  vector related to the time derivative of the transformation matrix  $\mathbf{H}_{J,I}$ , while  $\mathbf{v}_{j,I}$  is a  $k_I \times 1$  vector representing the relative degrees of freedom.  $\mathbf{A}_I$  is a  $6 \times k_I$  full-rank matrix whose columns have the  $6 \times 1$   $\mathbf{e}_i$ , with  $i=1 \dots k_I$  and vectors spanning the allowed motions. Each  $\mathbf{e}_i$  can be seen as  $\mathbf{e}_i = [\mathbf{e}_{i,U}^T \ \mathbf{e}_{i,\Omega}^T]^T$ , where the  $3 \times 1$  unit vectors  $\mathbf{e}_{i,U}$  and  $\mathbf{e}_{i,\Omega}$  are related to the displacement and rotation parts of the relative motions, respectively, as follows

$$\mathbf{A}_I = \begin{bmatrix} \mathbf{e}_{1,U} & \dots & \mathbf{e}_{k_I,U} \\ \mathbf{e}_{1,\Omega} & \dots & \mathbf{e}_{k_I,\Omega} \end{bmatrix} \quad (4.24)$$

Since they are brought by local frame elements, their components are constant so that matrix  $\mathbf{A}_I$  is also constant. In Table 4.1, some examples of usual joints are given, but others, such as the hinge joint, the planar joint or the screw joint, can be easily formulated in this framework, as well (Sonneville and Brüls, 2014).

#### Example: kinematics of revolute joint

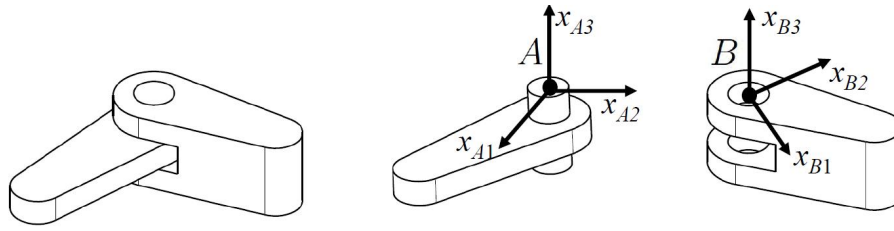


Figure 4.4: Revolute joint and its two set of axis.

rotation axis is the 3<sup>rd</sup> axis of the body-attached frame (Figure 4.4), then

$$\mathbf{H}_I = \begin{matrix} \mathbf{R}_{JI} \\ \left[ \begin{array}{ccc|c} \cos\theta & -\sin\theta & 0 & 0 \\ \sin\theta & \cos\theta & 0 & 0 \\ 0 & 0 & 1 & 0 \\ 0 & 0 & 0 & 1 \end{array} \right] \mathbf{x}_{JI} \end{matrix}$$

then

$$\tilde{\mathbf{v}}_{j,I} = \begin{bmatrix} 0 & -\dot{\theta} & 0 \\ \dot{\theta} & 0 & 0 \\ 0 & 0 & 0 \end{bmatrix}, \mathbf{v}_{j,I} = \dot{\theta}$$

$$\tilde{\mathbf{v}}_{J,I} = \begin{bmatrix} 0 & 0 & \dot{\theta} & 0 \\ 0 & 0 & 0 & 0 \\ -\dot{\theta} & 0 & 0 & 0 \\ 0 & 0 & 0 & 0 \end{bmatrix}, \mathbf{v}_{J,I} = \begin{bmatrix} 0 \\ 0 \\ 0 \\ \dot{\theta} \end{bmatrix} \Rightarrow \mathbf{A}_I = \begin{bmatrix} 0 \\ 0 \\ 0 \\ 0 \\ 0 \\ 1 \end{bmatrix} \begin{matrix} \mathbf{e}_{I1,U} \\ \mathbf{e}_{I1,\Omega} \end{matrix}$$

### 4.3.2 Kinematics of a multibody system

It is convenient to introduce a unified matrix notation to treat both the nodal and kinematic joints at the same time. Considering  $M$  nodes and  $m$  kinematic joints at the system level, a unified matrix notation can be introduced such that the state of the system is described using the invertible block-diagonal square matrix

$$\mathbf{H} = \text{diag}(\mathbf{H}_1, \dots, \mathbf{H}_M, \mathbf{H}_{J,1}, \dots, \mathbf{H}_{J,m}) \quad (4.25)$$

The time derivative of  $\mathbf{H}$  can be expressed as  $\dot{(\mathbf{H})} = \mathbf{H}\tilde{\mathbf{v}}^*$ , where

$$\tilde{\mathbf{v}}^* = \text{diag}(\tilde{\mathbf{v}}_1, \dots, \tilde{\mathbf{v}}_M, \tilde{\mathbf{v}}_{J,1}, \dots, \tilde{\mathbf{v}}_{J,m}) \quad (4.26)$$

The  $(6M+6m)$ -dimensional vector  $\mathbf{v}^*$  relates to a  $(6M+k_J+\dots+k_m)$ -dimensional vector  $\mathbf{v}$  as

$$\mathbf{v}^* = \mathbf{A}\mathbf{v} \quad (4.27)$$

where  $\mathbf{A} = \text{diag}(\mathbf{I}_{6 \times 6}, \dots, \mathbf{I}_{6 \times 6}, \mathbf{A}_1, \dots, \mathbf{A}_m)$  and  $\mathbf{v} = [\mathbf{v}_1^T \dots \mathbf{v}_M^T \mathbf{v}_{j,1}^T \dots \mathbf{v}_{j,m}^T]^T$ . In the same fashion, the variation of  $\mathbf{H}$  is given by  $\delta(\mathbf{H}) = \mathbf{H}\tilde{\delta\mathbf{h}}^*$ , where  $\tilde{\delta\mathbf{h}}^* = [\delta\mathbf{h}_1^T \dots \delta\mathbf{h}_M^T \delta\mathbf{h}_{j,1}^T \dots \delta\mathbf{h}_{j,m}^T]^T$ , and the  $(6M+6m)$ -dimensional vector  $\mathbf{h}^*$  relates to a  $(6M+k_J+\dots+k_m)$ -dimensional vector  $\mathbf{h}$  as

$$\mathbf{h}^* = \mathbf{A}\mathbf{h} \quad (4.28)$$

This mapping also holds for the variation, that is  $\delta\mathbf{h}^* = \mathbf{A}\delta\mathbf{h}$ , where  $\delta\mathbf{h} = [\delta\mathbf{h}_1^T \dots \delta\mathbf{h}_M^T \delta\mathbf{h}_{j,1}^T \dots \delta\mathbf{h}_{j,m}^T]^T$ .

In some cases, such as in the prismatic joint, the formulation enables the use of relative coordinates. Indeed, in such a joint I,  $\mathbf{v}_{j,I}$  can be interpreted as the time derivative coordinate  $\alpha_I$ , which is thus denoted as  $\mathbf{v}_{j,I} = \dot{\alpha}_I$ . Therefore, flexibility in the joint (local spring-damper elements), control law or actuators in such joints are conveniently introduced as functions of relative coordinates  $\alpha_I$ , which are simply obtained by time integration of  $\dot{\alpha}_I$ .

### 4.3.3 Constraint equations

In the  $SE(3)$  formalism, the relationship between nodes A and B which are connected by a rigid constraint or by a kinematic joint I can be conveniently expressed as

$$\mathbf{H}_B = \mathbf{H}_A \mathbf{H}_{J,I} \quad (4.29)$$

where  $\mathbf{H}_A$  and  $\mathbf{H}_B$  are the nodal homogeneous matrices of nodes A and B, respectively, and  $\mathbf{H}_{J,I}$  is a homogeneous matrix that describes the relative motion between the two nodes due to the joint I. In order to obtain vector equations from the matrix equations in Equation (4.29), a vectorial map is introduced and the constraint equations at system level take the form

$$\Psi(\mathbf{H}) = [\Psi_1 \quad \dots \quad \Psi_m]^T \quad (4.30)$$

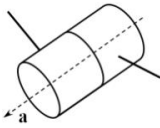
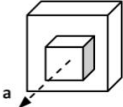
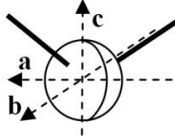
where, for each joint I, one has six constraints given by

$$\Psi_1(\mathbf{H}_A, \mathbf{H}_B, \mathbf{H}_{J,I}) = \text{vect}_{\text{SE}(3)}(\mathbf{H}_B^{-1} \mathbf{H}_A \mathbf{H}_{J,I}) = \mathbf{0}_{6 \times 1} \quad (4.31)$$

where the vectorial map is defined as

$$\text{vect}_{\text{SE}(3)}(H(\mathbf{R}, \mathbf{x})) = \begin{bmatrix} \mathbf{x} \\ \psi(\mathbf{R}) \end{bmatrix} \quad (4.32)$$

Table 4.1:  $A_J$  matrix of rigid constraint and some kinematic joints.

Joints	k-th column of $A_J$	$\mathbf{e}_U$	$\mathbf{e}_\Omega$
Rigid constraint	$\mathbf{0}$	-	-
Revolute joint 	1	$\mathbf{0}_{3 \times 1}$	$\mathbf{a}$
Prismatic joint 	1	$\mathbf{a}$	$\mathbf{0}_{3 \times 1}$
Spherical joint 	1 2 3	$\mathbf{0}_{3 \times 1}$ $\mathbf{0}_{3 \times 1}$ $\mathbf{0}_{3 \times 1}$	$\mathbf{a}$ $\mathbf{b}$ $\mathbf{c}$

such that  $\tilde{\psi}(\mathbf{R}) = (\mathbf{R} - \mathbf{R}^T)/2$ . This vectorial map introduces systematically six constraints for a kinematic joint or a rigid constraint. The vectorial map imposes that the relative displacements and relative rotations contained in  $\mathbf{H}_{J,I}$  are exactly the relative configuration between node A and B by imposing three constraints at the position level and three constraints at the rotation level. The systematic use of six constraint equations is related to the mixed coordinate formulation. Indeed, for a joint I that has  $k_I$  degrees of freedom, the vectorial map provides  $k_I$  equations for the degrees of freedom and  $6 - k_I$  equations to prevent some relative motions between nodes A and B. The resulting constraint equations are invariant under rigid body motions, making them particularly appropriate to catch and enforce restricted relative motions in multibody systems.

#### 4.3.4 Constraint gradient

Constraint contributions to the equations of motion in Equation (4.80) are achieved using the directional derivative as follows (Sonneville and Bruls, 2014):

$$(D\Psi(\mathbf{H}) \cdot \delta\mathbf{h}^*) = \Psi_q^*(\mathbf{H})\delta\mathbf{h}^* = \Psi_q(\mathbf{H})\delta\mathbf{h} \quad (4.33)$$

where  $\Psi_q(\mathbf{H}) = \Psi_q^*(\mathbf{H})\mathbf{A}$ . When the constraint equations in Equation (4.31) are satisfied, their directional derivative is given by

$$(D\Psi_I \cdot \delta\mathbf{h}_{ABI}^*) \Big|_{\Psi_I=0} = \text{vect}_{\text{SE}(3)}(\mathbf{H}_{J,I}^{-1} \tilde{\delta}\mathbf{h}_A \mathbf{H}_{J,I} - \tilde{\delta}\mathbf{h}_B + \tilde{\delta}\mathbf{h}_{J,I}) \quad (4.34)$$

where  $\delta\mathbf{h}_{ABI}^* = [\delta\mathbf{h}_A^T \delta\mathbf{h}_B^T \delta\mathbf{h}_{J,I}^T]^T$ ,  $\mathbf{H}_{J,I} = H(\mathbf{R}_{J,I}, \mathbf{x}_{J,I})$ , and  $\delta\mathbf{H}_B^{-1} = -\tilde{\delta}\mathbf{h}_B \mathbf{H}_B^{-1}$ . Since the vectorial map is linear, each contribution can be considered separately. Hence, the constraint gradient can be obtained from  $(D\Psi_I \cdot \delta\mathbf{h}_{ABI}^*) \Big|_{\Psi_I=0} = (\Psi_{Iq}^* \cdot \delta\mathbf{h}_{ABI}^*) \Big|_{\Psi_I=0}$ . A variation of Equation (4.28) is introduced in order to obtain  $\Psi_q$ , namely

$$(\Psi_{Iq}) \Big|_{\Psi_I=0} = \begin{bmatrix} Ad_{\mathbf{H}_{J,I}^{-1}} & -\mathbf{I}_{6 \times 6} & \mathbf{A}_I \end{bmatrix} \quad (4.35)$$

where  $\mathbf{A}_I$  is given in Equation (4.23) and Table 4.1,  $Ad$  is the adjoint mapping matrix,

$$Ad_{\mathbf{H}_{J,I}^{-1}} = \begin{bmatrix} \mathbf{R}_{J,I}^T & -\mathbf{R}_{J,I}^T \tilde{\mathbf{x}}_{J,I} \\ \mathbf{0}_{3 \times 3} & \mathbf{R}_{J,I}^T \end{bmatrix} \quad (4.36)$$

It is remarkable that the constraint gradient at equilibrium only depends on the relative configuration ( $\mathbf{x}_{J,I}$  and  $\mathbf{R}_{J,I}$ ), and not on the global motion of nodes A and B. This shows that the nonlinearity of the formulation is only related to the local motion.

This expression of the gradient can be straightforwardly extended to multiple constraints by considering a finite element-like assembly procedure. Every six lines of the resulting  $\Psi_q$  matrix refers to corresponding six lines of the constraint in  $\Psi$  and the columns corresponding to the nodes and the degrees of the freedom of the kinematic joints are properly placed.

## 4.4 Flexible beam

In this section, the flexible beam formulation is briefly introduced based on the Special Euclidean group  $SE(3)$  formalism. Details of the formulation have been presented by Sonnevile *et al.* (2014).

### 4.4.1 Beam kinematics

Defining  $s \in [0, L]$  as the spatial parameter along the neutral axis of a beam of length  $L$ , and  $t$  and  $u$  as the cross-section parameters. In the  $SE(3)$  formalism, a material frame is attached to any material point, and any point of the neutral axis of the beam is described by the mapping  $\mathbb{R} \rightarrow SE(3) : s \rightarrow \mathbf{H}(s) = H(\mathbf{R}(s), \mathbf{x}(s))$ , that is

$$\mathbf{H}(s) = \begin{bmatrix} \mathbf{R}(s) & \mathbf{x}(s) \\ \mathbf{0}_{1 \times 3} & 1 \end{bmatrix} \quad (4.37)$$

where  $\mathbf{x}(s)$  is the position vector of the neutral axis and  $\mathbf{R}(s)$  characterizes the orientation of the cross-section. The description is illustrated in Figure 4.5.

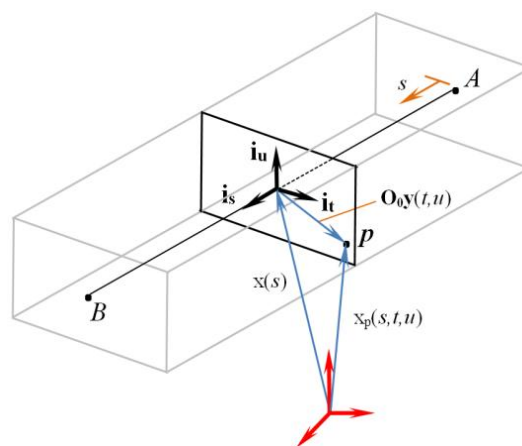


Figure 4.5: Description of the beam kinematics.

Accordingly, the material frame  $\mathbf{H}_p(s, t, u) = H(\mathbf{R}_p(s), \mathbf{x}_p(s, t, u))$  at any beam point  $p$  of coordinates  $(s, t, u)$  is related to the material frame attached to the neutral axis by the frame transformation

$$\mathbf{H}_p(s, t, u) = \mathbf{H}(s) \begin{bmatrix} \mathbf{I}_{3 \times 3} & \mathbf{O}_0 \mathbf{y}(t, u) \\ \mathbf{0}_{1 \times 3} & 1 \end{bmatrix} = \mathbf{H}(s) \mathbf{H}_y(t, u) \quad (4.38)$$

in which  $\mathbf{y}(t, u) = [0 \ t \ u]^T$  and  $\mathbf{O}_0 = [\mathbf{i}_s \ \mathbf{i}_t \ \mathbf{i}_u]$  is a constant rotation matrix built on the unit vectors along the neutral axis and the cross-sections that account for the orientation of the beam in the reference configuration with respect to the inertial frame. The assumption that the cross-sections remain straight is made and implies that  $\mathbf{R}_p(s) = \mathbf{R}(s)$ . From Equation (4.38), the position at any point of the beam is thus described as

$$\mathbf{x}_p(s, t, u) = \mathbf{x}(s) + \mathbf{R}(s) \mathbf{O}_0 \mathbf{y}(t, u) \quad (4.39)$$

#### 4.4.2 Kinetic and strain energies

According to the present formalism, the spatial and time derivatives of the frames representing the neutral axis of the beam can be introduced as

$$\mathbf{H}' = \mathbf{H}(\tilde{\mathbf{f}}^0 + \tilde{\boldsymbol{\varepsilon}}) \quad \text{and} \quad \dot{\mathbf{H}} = \mathbf{H}\tilde{\mathbf{v}} \quad (4.40)$$

where  $\tilde{\mathbf{f}}^0$  is interpreted as a deformation gradient in the reference configuration,  $\boldsymbol{\varepsilon}$  as a deformation and  $\tilde{\mathbf{v}}$  as a velocity. These vectorial fields are interpreted as being measured in the local frame, and are thus invariant under rigid body motions. From these deformation and velocity measures, the kinetic energy and the strain energy for a linear elastic material can be defined, respectively, as (Sonneville *et al.*, 2014)

$$W = \frac{1}{2} \int_0^L \boldsymbol{\varepsilon}^T \mathbf{K} \boldsymbol{\varepsilon} ds \quad (4.41)$$

and

$$K = \frac{1}{2} \int_0^L \tilde{\mathbf{v}}^T \mathbf{M}_C \tilde{\mathbf{v}} ds \quad (4.42)$$

where  $\mathbf{K}$  and  $\mathbf{M}_C$  are the stiffness and mass matrices of the cross-sections. For simple cross-section geometries, the stiffness matrix has the classical form  $\mathbf{K} = \text{diag}(\mathbf{K}_U, \mathbf{K}_\Omega)$ , where  $\mathbf{K}_U = \text{diag}(EA, GA_t, GA_u)$  contains the axial and shear stiffnesses, whereas  $\mathbf{K}_\Omega = \text{diag}(GJ, EI, EI_u)$  contains the torsional and bending stiffnesses, and the mass matrix

has the classical form  $\mathbf{M}_C = \text{diag}(\rho A \mathbf{I}_{3 \times 3}, \mathbf{J})$ , where  $\mathbf{J}$  is the second moment of inertia and is diagonal. These matrices are evaluated in the local frame and are therefore invariant under rigid body motions. Furthermore, due to the assumption that the cross-sections do not deform, they do not depend on the deformation state.

Since the rotation matrices are initially identity matrices, the inertia tensors must be provided with respect to the inertial frame in the initial configuration. If we denote as  $\mathbf{R}_{0I}$  the rotation matrix built using the principal axes of the body  $I$  in the initial configuration, then the inertia tensor  $\mathbf{J}'_I$  computed in the principal axes leads to  $\mathbf{J}_I = \mathbf{R}_{0I} \mathbf{J}'_I \mathbf{R}_{0I}^T$ .

#### 4.4.3 Finite element discretization

##### 4.4.3.1 Nodal interpolation

The spatial discretization along the neutral axis of the beam is introduced by an interpolation with the variable  $s \in [0, L]$  between two end nodes A at  $s = 0$  and B at  $s = L$ , where the nodal frames  $\mathbf{H}_A$  and  $\mathbf{H}_B$  are located (Figure 4.6).

The proposed interpolation formula reads

$$\mathbf{H}(s) = \mathbf{H}_A \exp_{SE(3)}\left(\frac{s}{L} \mathbf{d}\right) \quad (4.43)$$

where  $\mathbf{d} = [\mathbf{d}_U^T \quad \mathbf{d}_\Omega^T]^T$  is the relative configuration vector and is defined as

$$\mathbf{d} = \log_{SE(3)}(\mathbf{H}_A^{-1} \mathbf{H}_B) \quad (4.44)$$

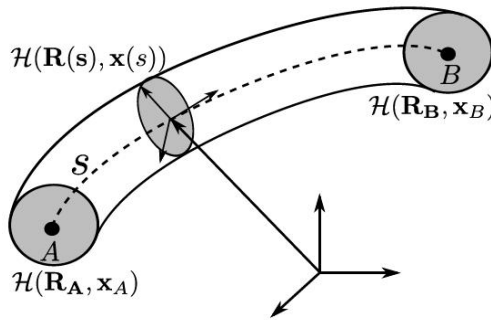


Figure 4.6: Flexible beam model.



This formula can be seen as a straightforward extension of the classical interpolation formula to  $SE(3)$ , which is a non-linear space. An important feature of the relative configuration vector is that it does not depend on the global motion and is thus invariant under rigid body motions and is particularly suitable for local deformation measurements.

#### 4.4.3.2 Discretized deformation and velocity fields

The derivative of Equation (4.43) with respect to the spatial coordinate provides the definition of the discretized deformation as

$$\varepsilon = \frac{\mathbf{d} - \mathbf{d}^0}{\mathbf{L}} \quad (4.45)$$

where  $\mathbf{d}^0$  is the relative configuration vector in the reference configuration. Hence, the deformation measure is constant over the element, which appears as an important numerical advantage. As an important consequence of the framework, the deformation measure depends on the relative configuration vector  $\mathbf{d}$  only, which means that it is invariant under rigid body motions.

Deriving Equation (4.43) with respect to time leads to a consistent spatial interpolation formula for the velocities. Denoting the nodal velocities evaluated in the local frames as  $\dot{\mathbf{H}}_A = \mathbf{H}_A \tilde{\mathbf{v}}_A$  and  $\dot{\mathbf{H}}_B = \mathbf{H}_B \tilde{\mathbf{v}}_B$ , we have

$$\mathbf{v} = \mathbf{Q}(s, \mathbf{d}) \mathbf{v}_{AB} \quad (4.46)$$

where a  $12 \times 1$  velocity vector  $\mathbf{v}_{AB} = [\mathbf{v}_A^T \quad \mathbf{v}_B^T]^T$ , and denoting  $\mathbf{T}^* = \begin{pmatrix} \mathbf{s} \\ \mathbf{L} \end{pmatrix} \mathbf{T}_{SE(3)} \begin{pmatrix} \mathbf{s} \\ \mathbf{L} \end{pmatrix} \mathbf{d} \mathbf{T}_{SE(3)}^{-1}(\mathbf{d})$ , thus it can be derived that

$$\mathbf{Q}(s, \mathbf{d}) = \begin{bmatrix} \mathbf{I}_{6 \times 6} & -\mathbf{T}^*(s, \mathbf{d}) \\ \mathbf{0} & \mathbf{T}^*(s, \mathbf{d}) \end{bmatrix} \quad (4.47)$$

This velocity interpolation formula depends on  $\mathbf{d}$  only, and exhibits also independence with respect to rigid body motions.

#### 4.4.4 Discretized beam equations

Using the interpolation fields discussed in section 4.4.3.2 in Hamilton's principle, it can be shown that dynamic equilibrium equations for a beam element take the form of ordinary differential equations on the Lie group (Sonneville *et al.*, 2014)

$$\dot{\mathbf{H}}_A = \mathbf{H}_A \tilde{\mathbf{v}}_A \quad (4.48)$$

$$\dot{\mathbf{H}}_B = \mathbf{H}_B \tilde{\mathbf{v}}_B \quad (4.49)$$

$$\mathbf{M}(\mathbf{d}) \dot{\mathbf{v}}_{AB} + \mathbf{C}(\mathbf{d}, \mathbf{v}_{AB}) \mathbf{v}_{AB} + \mathbf{P}(\mathbf{d})^T \mathbf{K} \boldsymbol{\varepsilon} = \int_0^L \mathbf{Q}(s, \mathbf{d})^T \mathbf{g}_{ext} ds \quad (4.50)$$

where  $\mathbf{g}_{ext}$  are the external forces,  $\mathbf{P}(\mathbf{d}) = \begin{bmatrix} -\mathbf{T}_{SE(3)}^{-1}(-\mathbf{d}) & \mathbf{T}_{SE(3)}(\mathbf{d}) \end{bmatrix}$ , and denoting  $\mathbf{Q} = \mathbf{Q}(s, \mathbf{d})$  (see Equation (4.47)), the  $12 \times 12$  mass matrix is defined as

$$\mathbf{M}(\mathbf{d}) = \int_0^L \mathbf{Q}^T \mathbf{M}_c \mathbf{Q} ds \quad (4.51)$$

where  $\mathbf{M}_c$  matrix has introduced in Equation (4.42), and the  $12 \times 12$  matrix

$$\mathbf{C}(\mathbf{d}, \mathbf{v}_{AB}) = \int_0^L \mathbf{Q}^T (\mathbf{M}_c \dot{\mathbf{Q}} - \widehat{\mathbf{Qv}}_{AB}^T \mathbf{M}_c \mathbf{Q}) ds \quad (4.52)$$

where  $\mathbf{M}(\mathbf{d}) \dot{\mathbf{v}}_{AB}$  are the inertia forces,  $\mathbf{C}(\mathbf{d}, \mathbf{v}_{AB}) \mathbf{v}_{AB}$  the gyroscopic forces and  $\mathbf{P}(\mathbf{d})^T \mathbf{K} \boldsymbol{\varepsilon}$  the internal forces. Notice how Equation (4.50) only depends on local frame information, and therefore does not depend on the global motion of the beam element.

#### 4.5 Flexible sliding joint

In this section, a flexible sliding joint based on the beam element described in section 4.4 is developed. Consider two bodies denoted with  $k$  and  $l$ , respectively, linked together by a sliding joint, as depicted in Figure 4.7.

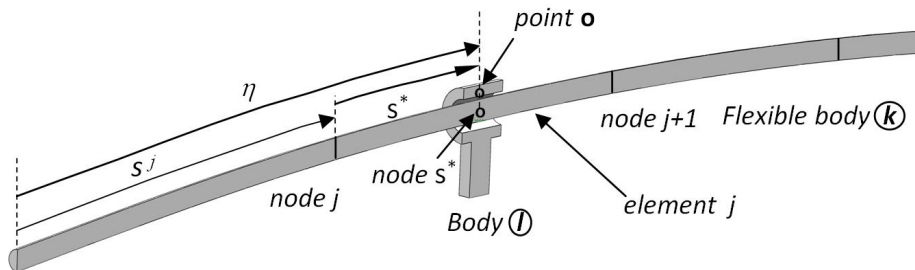


Figure 4.7: A body sliding along a flexible body with a sliding joint.

Body l is a rigid body and body k is a flexible beam which is discretized according to the method presented in section 4.4. Body k is described by  $N$  nodes. According to the longitudinal nature of the flexible beam, the  $N$  beam elements are numbered with an index  $j \in [0, N]$  from an origin chosen at an extremity of body k. The nodes related to element  $j$  are then numbered  $j$  and  $j+1$ . A coordinate  $s_j$  is assigned to node  $j$ , corresponding to a coordinate from an origin chosen at an extremity of the flexible beam. Define  $\eta$  as a coordinate for the position of body l along the flexible body such that  $\eta=0$  at  $s_0$ . When body l slides along the flexible beam element  $j$ , a non-dimensional parameter  $s^* \in [0,1]$  indicating the location of a body l along a particular element of the flexible beam can be expressed as a function of the nodal coordinates  $s_j$  and  $s_{j+1}$  as

$$s^* = \frac{\eta - s_j}{s_{j+1} - s_j} \quad (4.53)$$

According to the beam formulation presented in section 4.4, the material frame at  $s^*$  is given as

$$\mathbf{H}^* = \mathbf{H}_j \exp_{SE(3)}(s^* \mathbf{d}_j) \quad (4.54)$$

where  $\mathbf{d}_j = \log_{SE(3)}(\mathbf{H}_j^{-1} \mathbf{H}_{j+1})$ ,  $\mathbf{H}_j$  and  $\mathbf{H}_{j+1}$  are nodal material frames at nodes  $s_j$  and  $s_{j+1}$  respectively. When modeling a flexible sliding joint, the coincidence of node 0 associated with body l and the center line of the flexible joint (node  $s^*$ ), temporarily, must be imposed, meaning that this equality is verified:

$$\mathbf{H}_0 = \mathbf{H}^* \Leftrightarrow \Psi = \text{vect}_{SE(3)}(\mathbf{H}_0^{-1} \mathbf{H}^*) = \mathbf{0}_{6 \times 1} \quad (4.55)$$

which stands thus as a constraint equation. When the constraint is satisfied, its directional derivative is given by

$$D\Psi \cdot \delta \mathbf{h} = \Psi_q \delta \mathbf{h} = \begin{bmatrix} -\mathbf{I}_{6 \times 6} & \mathbf{I}_{6 \times 6} \end{bmatrix} \begin{bmatrix} \delta \mathbf{h}_0 \\ \delta \mathbf{h}^* \end{bmatrix} \quad (4.56)$$

Using the variation of Equation (4.54), and after simplifications,  $\delta \mathbf{h}^*$  can be related to the variation of  $s^*$ ,  $\mathbf{h}_j$  and  $\mathbf{h}_{j+1}$  by

$$\delta \mathbf{h}^* = \begin{bmatrix} \mathbf{Q}(s^*, \mathbf{d}_j) & \mathbf{d}_j \end{bmatrix} \begin{bmatrix} \delta \mathbf{h}_{j,j+1} \\ \delta s^* \end{bmatrix} \quad (4.57)$$

where  $\mathbf{Q}$  was defined in Equation (4.47). Hence, the constraint gradient takes the form

$$\Psi_q = \begin{bmatrix} -\mathbf{I}_{6 \times 6} & \mathbf{Q}(s^*, \mathbf{d}_j) & \mathbf{d}_j \end{bmatrix} \quad (4.58)$$

## 4.6 Hydraulic control

### 4.6.1 Derivation of the hydraulic forces

Similarly to section 2.5.2, the hydraulic system can be analyzed, but with a simple difference. There is no need here to derive for relative kinematics at the joint level because the formulation of the constraint here is relatively per se. The pressures and flow rates in the system can be derived as follows.

Assuming that  $P_1$  and  $P_2$  are the pressures of the infill and return water cavity, respectively (Pa),  $A_1$  and  $A_2$  are the effective action area of the infill and the return water, respectively ( $\text{m}^2$ ), and  $Q_1$  and  $Q_2$  are the flow of the infill and the return water ( $\text{m}^3/\text{s}$ ), respectively (see Figure 2.8), then

$$P_L = F / A_1 = P_1 - P_2 (A_2 / A_1) \quad (4.59)$$

$$Q_L = Q_1 + n Q_2 / (1 + n^2) \quad (4.60)$$

In this formula,  $n = A_2 / A_1$ .  $P_L$  is the load pressure (difference in the pressure),  $Q_L$  is the load flow rate. The modeling of the valve openings is proportional to the spool position  $x_v$ , with  $\rho$  density, and the flow can be described by the following:

$$Q_1 = C_v x_v \sqrt{2(p_s - p_1) / \rho} \quad (4.61)$$

$$Q_2 = C_v x_v \sqrt{2p_2 / \rho} \quad (4.62)$$

where  $C_v$  is the flow rate coefficient. When the piston moves at a constant velocity, it can be seen that

$$Q_1 = A_1 \dot{\alpha} \quad \text{and} \quad Q_2 = A_2 \dot{\alpha} \quad (4.63)$$

where  $\dot{\alpha}$  is the relative piston velocity. Using the linearization to Equations (4.61) and (4.62) give

$$K_q = \partial Q_L / \partial x_v \quad \text{and} \quad K_c = \partial Q_L / \partial p_L \quad (4.64)$$

The linearization of the flow equation is

$$Q_L = K_q x_v - K_c p_L \quad (4.65)$$

When considering the flow continuity equation, the pressures inside chamber 1 and chamber 2 of the cylinder can be solved from the following equations:

$$\dot{p}_1 = \frac{Be}{A_1 \alpha + V_1} (Q_1 - A_1 \dot{\alpha} - C_{ic} (p_1 - p_2)) \quad (4.66)$$

$$\dot{p}_2 = \frac{Be}{A_2 (L - \alpha) + V_2} (-Q_2 + A_2 \dot{\alpha} + C_{ic} (p_1 - p_2)) \quad (4.67)$$

where  $\alpha$  is the relative displacement of a piston,  $L$  is the stroke,  $Be$  is the water bulk modulus,  $V_1$  and  $V_2$  are the volumes, and  $C_{ic}$  is internal leakage ((m<sup>3</sup>/s)/Pa). The hydraulic force produced inside the cylinder ( $F_h$ ) can be derived from the pressures acting on the piston as follows:

$$F_h = A_1 p_L - m \ddot{\alpha} - b \dot{\alpha} \quad (4.68)$$

where  $b$  is the coefficient of friction (impedance coefficient, N.s/m). Substitution in Equation (4.60) results in Equation (4.69):

$$Q_L = A_1 \dot{\alpha} - \frac{V_t}{2(1+n^2)Be} \dot{P}_L + C_{ic} P_L \quad (4.69)$$

where  $V_t$  is total volume, and  $C_{tc} = ((1+n)/(1+n^3))C_{ic} = 1.5628e-9$  (m<sup>3</sup>/s)/Pa. Using the Laplace transformation to Equations (4.66), (4.67), (4.68) and (4.69) gives (Dan *et al.*, 2010, Al-saedi *et al.*, 2012):

$$Q_L = K_q x_v - K_c p_L \quad (4.70)$$

$$Q_L = A_1 s \alpha - \frac{V_t}{2(1+n^2)Be} s P_L + C_{ic} P_L \quad (4.71)$$

$$A_1 p_L = (m s^2 + b s) \alpha + F_h \quad (4.72)$$

Using Equations (4.70), (4.71) and (4.72), we obtain the transfer function of the actuating unit of the valve controlled cylinder. Errors between the predicted and presented lengths are used to determine the required force of the six actuators. The controller is proposed as

$$u(k+1) = l_d(k+1) - l(k) \tag{4.73}$$

where  $l_d$  is the desired local displacement of a rod.

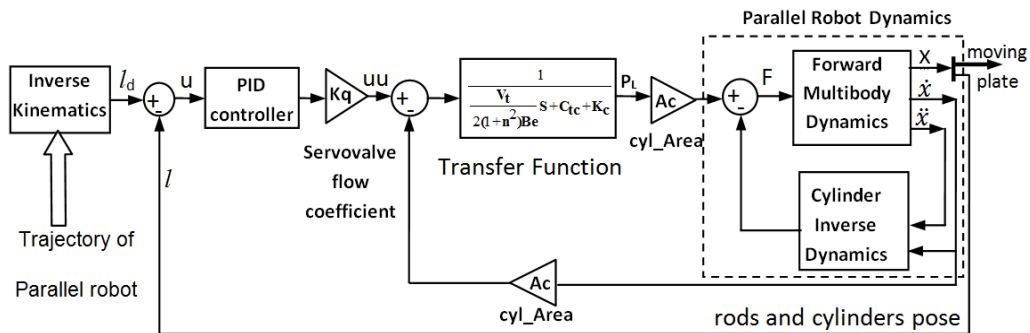


Figure 4.8: Block diagram of the control system of the parallel robot.

#### 4.6.2 PID control of the parallel robot

The popularity of PID controllers can be attributed partly to their robust performance in a wide range of operating conditions and partly to their functional simplicity, which allows simple and straightforward operation (Dorf and Bishop, 2005). To implement such a controller, three parameters must be determined for the given process: the proportional coefficient  $K_p$ , with integral coefficient  $K_i=K_p/T_i$ , and the derived coefficient  $K_d$ .

The PID controller has the following transfer function:

$$W(s) = K_p \left( 1 + \frac{1}{T_i s} + K_d s \right) \tag{4.74}$$

Figure 4.8 shows the block diagram of the control system for each cylinder.

## 4.7 Dynamic equations of mechatronic systems

### 4.7.1 Dynamic equations

According to Brüls (2005) and Brüls and Arnold (2008), and considering the present Lie group setting (Sonneville and Brüls, 2014), the dynamic equilibrium equations of the mechatronic system can be formulated using variational principles as

$$\dot{\mathbf{H}} = \mathbf{H}\dot{\mathbf{v}}^* \quad (4.75)$$

$$\mathbf{M}\dot{\mathbf{v}} + \mathbf{g}(\mathbf{H}, \mathbf{v}) + \Psi_q^T(\mathbf{H})\boldsymbol{\lambda} = \mathbf{L}\mathbf{y} \quad (4.76)$$

$$\Psi(\mathbf{H}) = \mathbf{0} \quad (4.77)$$

$$\dot{\mathbf{z}} = \mathbf{f}(\mathbf{H}, \mathbf{v}, \dot{\mathbf{v}}, \boldsymbol{\lambda}, \mathbf{z}, \mathbf{y}, t) \quad (4.78)$$

$$\mathbf{y} = \mathbf{h}(\mathbf{H}, \mathbf{v}, \dot{\mathbf{v}}, \boldsymbol{\lambda}, \mathbf{z}, \mathbf{y}, t) \quad (4.79)$$

where  $\mathbf{H}$  is the state of the mechanical system, containing the nodal and kinematic joint transformation matrices, and  $\mathbf{v}$  and  $\dot{\mathbf{v}}$  are the velocities and the accelerations. Following Equation (4.21) and Equation (4.23),  $\mathbf{v}$  stands for the collection of the  $\mathbf{v}_I$ 's and the  $\mathbf{v}_{j,I}$ 's while  $\mathbf{v}^*$  stands for the collection of the  $\mathbf{v}_I$ 's and the  $\mathbf{v}_{j,I}$ 's,  $\boldsymbol{\lambda}$  is the Lagrange multipliers,  $\mathbf{z}$  the first-order variables which for the parallel robot case study are the vector of pressure differences inside each cylinder, i.e.  $\mathbf{z}=[p_{L1}, \dots, p_{L6}]$ , and  $\mathbf{y}$  the control output variables. Equations (4.75-4.76) describe the dynamics of the mechanical system, Equation (4.77) the kinematic constraints, Equation (4.78) the first-order control state dynamics, and Equation (4.79) the control output equation.

In Equation (4.76),  $\mathbf{M}\dot{\mathbf{v}}$  are the inertia forces, where the mass matrix  $\mathbf{M}$  is constant, and  $\mathbf{g}$  represents the external, internal and gyroscopic forces. For instance, the external forces are the gravity forces acting on the rigid bodies and the internal forces are the elastic and dissipation forces in the kinematic joints.  $\Psi_q$  is the constraint gradient and  $\Psi_q^T(\mathbf{H})\boldsymbol{\lambda}$  are the reaction forces due to the kinematic joints. The controllers, described by Equation (4.78), are influenced by input measurements from the mechanical system, whereas the mechanical system is driven by control forces  $\mathbf{L}\mathbf{y}$ , where  $\mathbf{L}$  is a constant Boolean matrix.

The equations of motion can be estimated as an index-3 DAE on a Lie group. Following Brüls and Arnold (2008), these equations of motion can be solved monolithically using a suitable version of the generalized- $\alpha$  scheme. Due to the Lie group setting, the mechanical part of the equations of motion must be treated consistently as proposed, for instance, by Brüls *et al.* (2012).

#### 4.7.2 Description of the integration algorithm

The system equations can be solved using the generalized-alpha method presented by Sonnevile and Brüls (2014), in which the Lie group structure of the equations of motion is handled as by Brüls and Cardona (2010). Denoting  $n$  as the time step and  $h$  as the time step size, this method relies on

- the discretized equations of motions in Equations (4.75 - 4.79) :

$$\mathbf{H}_{n+1} = \mathbf{H}_n \exp(\mathbf{n}_{n+1}) \quad (4.80)$$

$$\mathbf{M}\dot{\mathbf{v}}_{n+1} - \hat{\mathbf{v}}_{n+1}^T \mathbf{M}\mathbf{v}_{n+1} + \mathbf{g}_{\text{ext}}(\mathbf{H}_{n+1}) + \mathbf{g}_{\text{int}}(\mathbf{H}_{n+1}) + \Psi_{\mathbf{q}}^T(\mathbf{H}_{n+1})\lambda_{n+1} = \mathbf{0} \quad (4.81)$$

$$\Psi(\mathbf{H}_{n+1}) = \mathbf{0} \quad (4.82)$$

$$\dot{\mathbf{z}}_{n+1} - \mathbf{f}(\mathbf{H}_{n+1}, \mathbf{v}_{n+1}, \dot{\mathbf{v}}_{n+1}, \lambda_{n+1}, \mathbf{z}_{n+1}, \mathbf{y}_{n+1}, \mathbf{t}_{n+1}) = \mathbf{0} \quad (4.83)$$

$$\mathbf{y}_{n+1} - \mathbf{h}(\mathbf{H}_{n+1}, \mathbf{v}_{n+1}, \dot{\mathbf{v}}_{n+1}, \lambda_{n+1}, \mathbf{z}_{n+1}, \mathbf{y}_{n+1}, \mathbf{t}_{n+1}) = \mathbf{0} \quad (4.84)$$

- the time integration formulae for the motion variables

$$\mathbf{n}_{n+1} = h\mathbf{v}_n + (0.5 - \underline{\beta})h^2\mathbf{a}_n + \underline{\beta}h^2\mathbf{a}_{n+1} \quad (4.85)$$

$$\mathbf{v}_{n+1} = \mathbf{v}_n + (1 - \underline{\gamma})h\mathbf{a}_n + \underline{\gamma}h\mathbf{a}_{n+1} \quad (4.86)$$

$$\mathbf{a}_{n+1} = \frac{1}{(1 - \alpha_m)} ((1 - \alpha_f)\dot{\mathbf{v}}_{n+1} + \alpha_f\dot{\mathbf{v}}_n - \alpha_m\mathbf{a}_n) \quad (4.87)$$

- the time integration formulae for the state variables (Brüls and Arnold, 2008)

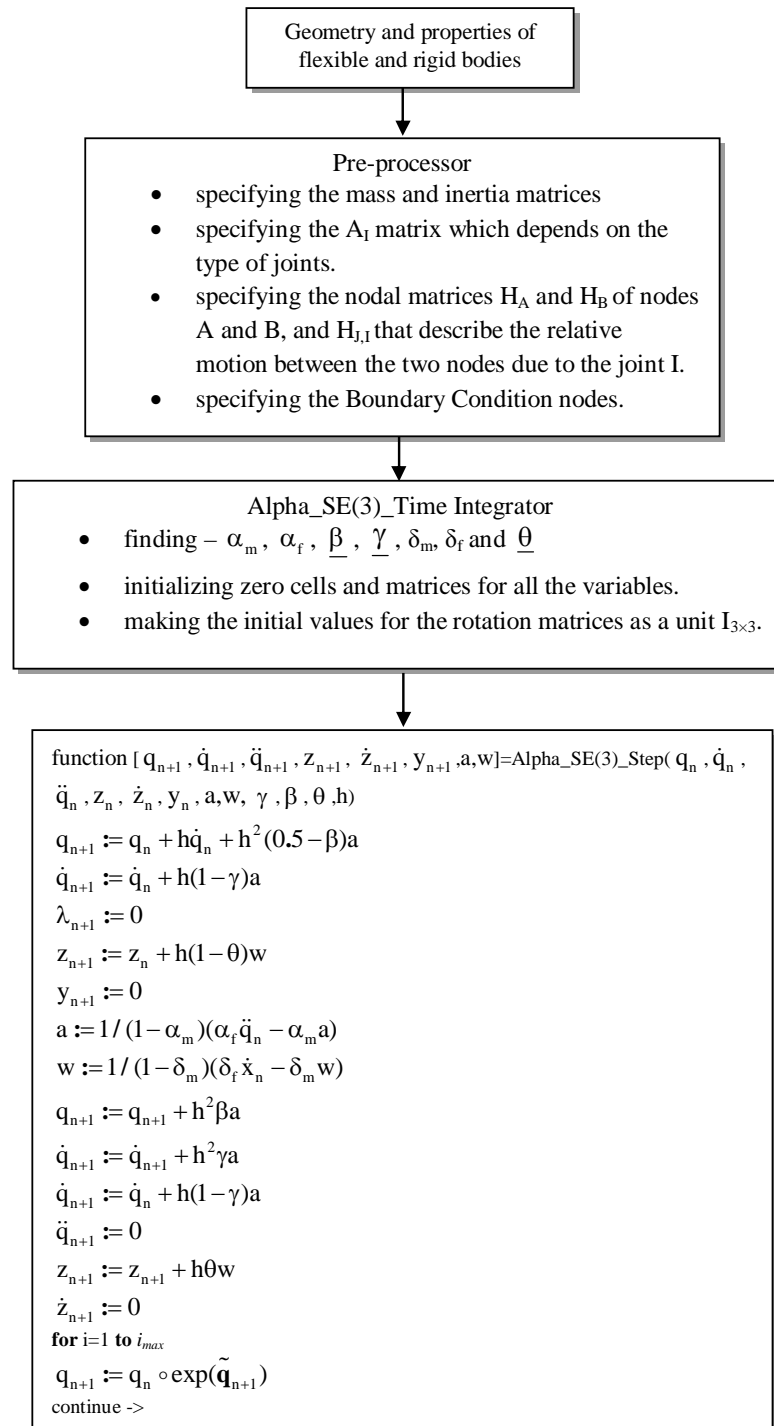
$$\mathbf{z}_{n+1} = \mathbf{z}_n + h(1 - \underline{\theta})\mathbf{w}_n + h\underline{\theta}\mathbf{w}_{n+1} \quad (4.88)$$

$$\mathbf{w}_{n+1} = \frac{1}{(1 - \delta_m)} ((1 - \delta_f)\dot{\mathbf{z}}_{n+1} + \delta_f\dot{\mathbf{z}}_n - \delta_m\mathbf{w}_n) \quad (4.89)$$

where  $\mathbf{a}$  and  $\mathbf{w}$  are auxiliary variables. The seven algorithmic parameters –  $\alpha_m$ ,  $\alpha_f$ ,  $\underline{\beta}$ ,  $\underline{\gamma}$ ,  $\delta_m$ ,  $\delta_f$  and  $\underline{\theta}$  – should be selected in order to obtain suitable accuracy and numerical stability properties.

Equations (4.80-4.84) are nonlinear and are solved at each time step for the unknowns  $\mathbf{n}_{n+1}$ ,  $\mathbf{v}_{n+1}$ ,  $\dot{\mathbf{v}}_{n+1}$ ,  $\mathbf{a}_{n+1}$ ,  $\mathbf{z}_{n+1}$ ,  $\dot{\mathbf{z}}_{n+1}$ ,  $\mathbf{w}_{n+1}$  and  $\mathbf{y}_{n+1}$  by a Newton iteration procedure.





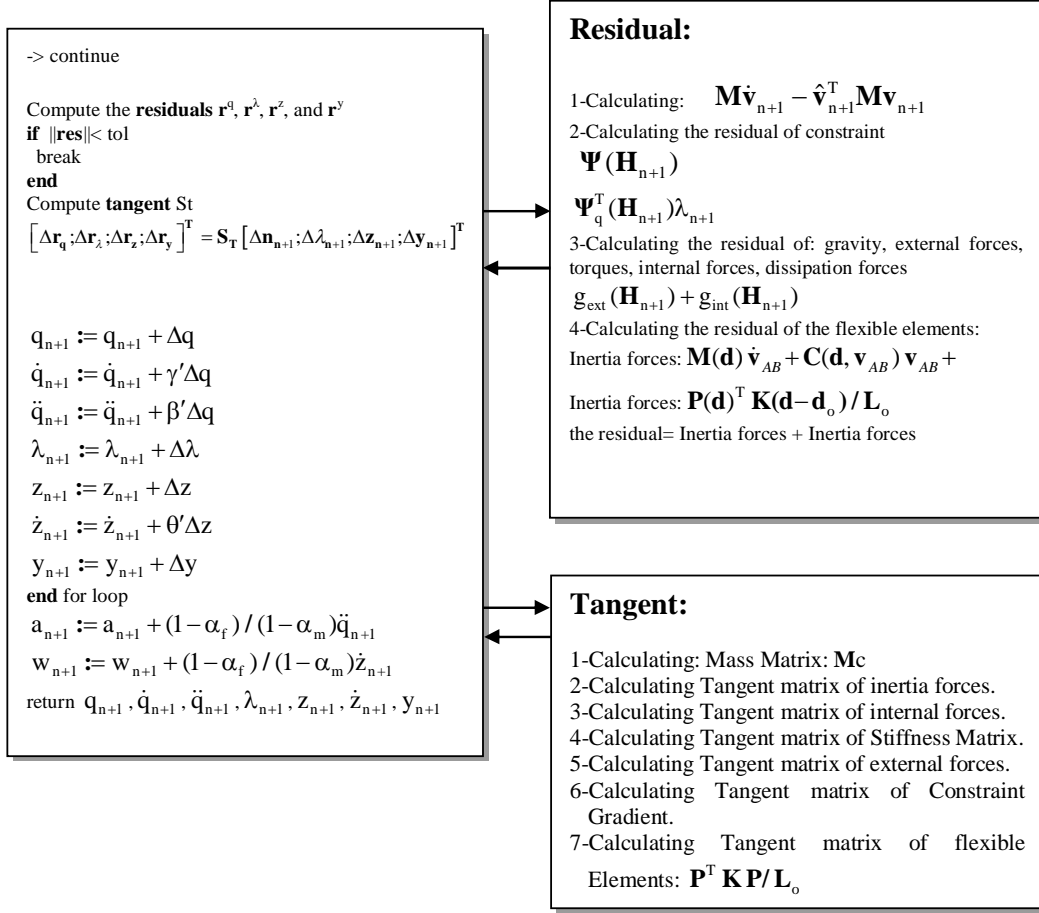


Figure 4.9: Flow-chart and algorithm diagram of the Special Euclidean  $SE(3)$  method of the parallel robot.

Eventually, Equations (4.80-4.84) can be denoted as  $[\mathbf{r}_q; \mathbf{r}_\lambda; \mathbf{r}_z; \mathbf{r}_y] = \mathbf{0}$  (i.e. the residuals), and the linearized form of Equations (4.80-4.84) is

$$[\Delta \mathbf{r}_q; \Delta \mathbf{r}_\lambda; \Delta \mathbf{r}_z; \Delta \mathbf{r}_y]^T = \mathbf{S}_T [\Delta \mathbf{n}_{n+1}; \Delta \lambda_{n+1}; \Delta \mathbf{z}_{n+1}; \Delta \mathbf{y}_{n+1}]^T \quad (4.90)$$

where  $\mathbf{S}_T$  is the iteration matrix (Brüls *et al.*, 2012). For small time steps  $h$ , the matrix  $\mathbf{S}_T$  becomes severely ill conditioned. This difficulty can be eliminated by implementation of a suitable scaling strategy (see e.g. Brüls *et al.*, 2011, Geradin, 1993).

Figure 4.9 is the flow-chart and algorithm diagram of the Special Euclidean  $SE(3)$  method and the Lie group integrator which is implemented to the parallel robot under study and also it can be used for dynamic simulation of any mechanism.

## 4.8 Robot parameters

The actual values of the system parameters of the parallel robot of each element are tabulated in Table 4.2. The local position of the universal joint in the base plate and the local position of the spherical joint in the moving plate are given. Initially, the tip point of each rod is located 0.35 m from the cylinder outlet. Young's modulus is  $2.07 \times 10^{11}$  N/m<sup>2</sup>, rod density  $\rho$  is 7801 kg/m<sup>3</sup>, the rod radius is 0.015 m, and the length is 0.668 m. All six rods are considered as having a uniform mass distribution and cross-section. Each of the rods is divided into six elements.

Table 4.2: Mass and inertia properties of parallel robot elements.

Element	Mass (Kg)	Izz =Iyy (Kg m <sup>2</sup> )	Ixx (Kg m <sup>2</sup> )	Ixy (Kg m <sup>2</sup> )
Cylinder	4.589	0.2160	2.89683e-3	0
Rod_piston	3.683	0.1372	4.14392e-4	0
Moving plate	28.92	0.1867	0.3622	0

Base points (local):  $[0.1658 \cdot \cos(120(1-i) + (90 \pm 14.851)) \quad 0.1658 \cdot \sin(120(1-i) + (90 \pm 14.851)) \quad 0]$   $i = 1, 2, 3$ . End effector points (local):  $[0.1296 \cdot \cos(120(1-i) + (90 \pm 45.485)) \quad 0.1296 \cdot \sin(120(1-i) + (90 \pm 45.485)) \quad 0]$   $i = 1, 2, 3$ .

The moving plate (end effector) tracks a trajectory of  $x = 0$ ,  $y = -0.1t \cos(42.87)$ , and  $z = +0.1t \sin(42.87)$ . In the simulations reported here, damping was not modeled, so any effect of high frequency vibration would be captured in the FEA.

## 4.9 Discussion

To verify the validity of the simulation, an ADAMS<sup>TM</sup> model of the parallel robot was developed, as previously shown in Figure 4.10. All cylinder rods were modeled as flexible bodies. The simulation model was loaded by hydraulic forces computed in the same way as forces used in the proposed method. In addition, the ADAMS<sup>TM</sup> model was controlled in the same hydraulic way as the model presented in this paper, so a direct comparison could be made between the models. The gain coefficients of the PID control for the flexible parallel robot without machining were  $K_p = 100$ , and  $K_d = 10$  for each cylinder. Finally, the parallel robot should track the required path without machining forces at the end effector.

In Figures 4.11 and 4.12, the y and z trajectories of the moving plate (end effector) have been compared with the same trajectories obtained from the dynamic model developed using the  $SE(3)$  method. The method proposed by this chapter is apparently more accurate than ADAMS<sup>TM</sup> model because the overshoot and the steady state error values during the simulation are reduced over time such that the error with respect to the desired path is reduced for the remainder of the simulation period. This result validates the modeling approach proposed in this chapter.

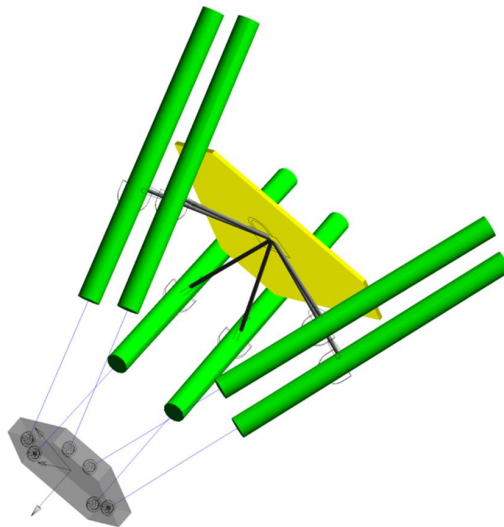


Figure 4.10: ADAMS model of the 6-UPS parallel robot.

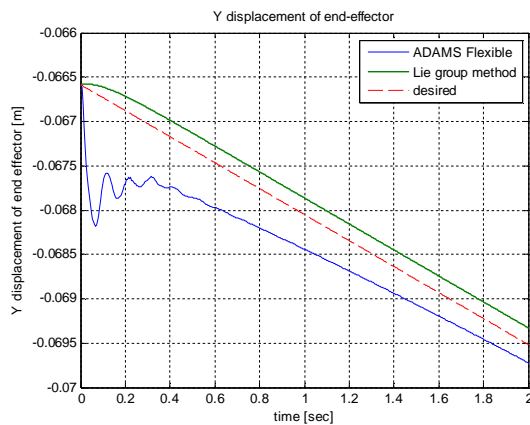


Figure 4.11: Y-displacement of the end effector using the flexible Lie group method and ADAMS<sup>TM</sup> model.

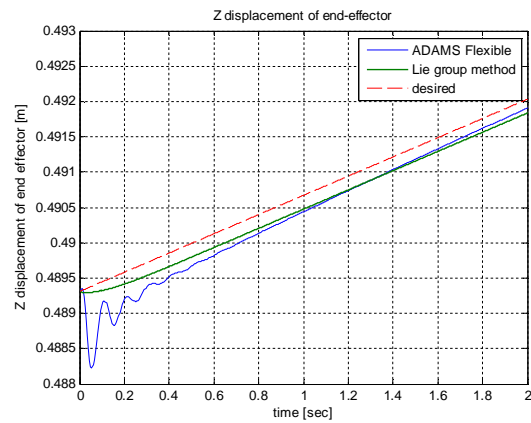


Figure 4.12: Z-displacement of the end effector using the flexible Lie group method and ADAMS<sup>TM</sup> model.

## 4.10 Simulation results

To examine the effect of elastic deformation on the performance of the parallel robot machine, a comparison was made between the required path for the parallel robot with flexible rods with and without machining forces. The machining forces were  $F_x = -1000 \sin(2\pi ft)$ ,  $F_y = 700 \sin(2\pi ft)$ , and  $F_z = -600 \sin(2\pi ft)$ , with  $f = 20$  Hz.

The gain coefficients of the PID control for the flexible parallel robot with or without machining forces were  $K_p = 200$ ,  $K_i = 200$ , and  $K_d = 10$  for each cylinder. These coefficients were chosen to optimize the tracking of the end effector with respect to the required machining path. All these gain values were estimates made by trial and error separately for each cylinder.

The displacements presented in Figures 4.13 and 4.14 show that the hydraulic 6 DOF flexible parallel robot with PID controller leads the moving plate (end effector) to the desired trajectories promptly and steadily in either of the two strategies. Overshoot and steady state errors in both the  $y$ - and  $z$ -displacements were small. Like the examples presented by Vakil *et al.* (2008), end effector vibration was not obviously apparent from these displacements figures. However, the components of end effector velocity and acceleration in the  $y$  and  $z$  directions, shown in Figures 4.15 and 4.16 as well as Figures 4.17 and 4.18, clearly revealed rod vibration.

Although the influence of machining forces (variable external forces) during the simulation can be observed in all of the figures, the results indicate that the evolution of the differences in the pressures inside each cylinder (see Figures 4.19-4.24) in the flexible robot with machining forces are higher than the differences in the pressure of the flexible robot without machining forces. This helps to select the appropriate servo valve properties for the actual robot.

Figures 4.25-4.30 present elastic deformations of the rods at their tip points. An obvious exchange of elastic strain exists between the rods. Flexibility coupling occurs between elastic deformations. This in turn indicates that deformation, as expected, is higher during machining due to the machining force effect. Moreover, it is clear from the relations of the moving plate displacement and Figures 4.25 through 4.30 that elastic deformations have a negligible effect on rigid body motion. This is because there is no structural damping assumed on one side, and the introduction of a prismatic joint motion controller as a linear spring and damper has the potential to absorb the elastic strain energy on the other side (Wang and Mills, 2006). In other words, the vibration of the rods is suppressed by the PID controller due to the mixed nodal coordinate formulation effects of rigid body motions and elastic motions in the  $SE(3)$  formulation for the equation of motion.

However, the elastic motions lead to apparent changes in the velocity and acceleration of rigid body motion, which is illustrated in Figures 4.15 and 4.16 as well as in

Figures 4.17 and 4.18. The changes will further impact the dynamic behaviors of the manipulator system (Zhang *et al.*, 2007).

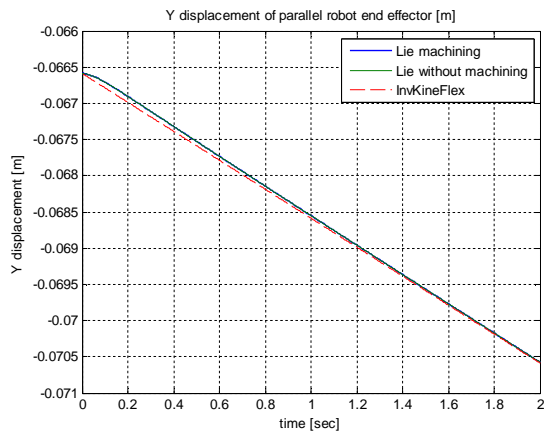


Figure 4.13: Y-displacement of the end effector of a flexible parallel robot using the flexible Lie group method with and without machining forces.

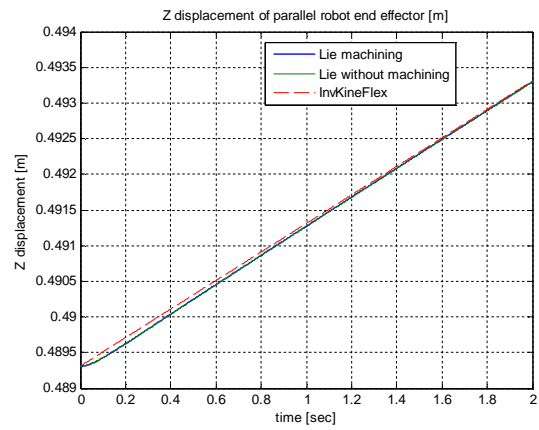


Figure 4.14: Z-displacement of the end effector of flexible parallel robot using the flexible Lie group method with and without machining forces.

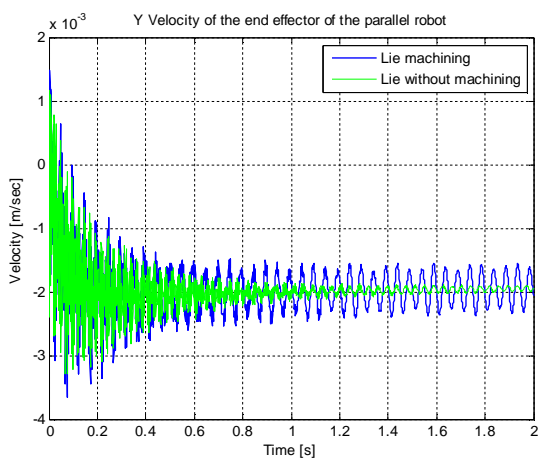


Figure 4.15: Y-velocity of the end effector of a flexible parallel robot using the flexible Lie group method with and without machining forces.

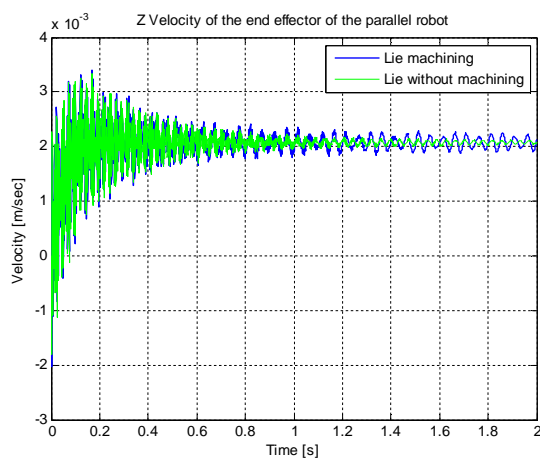


Figure 4.16: Z-velocity of the end effector of a flexible parallel robot using the flexible Lie group method with and without machining forces.

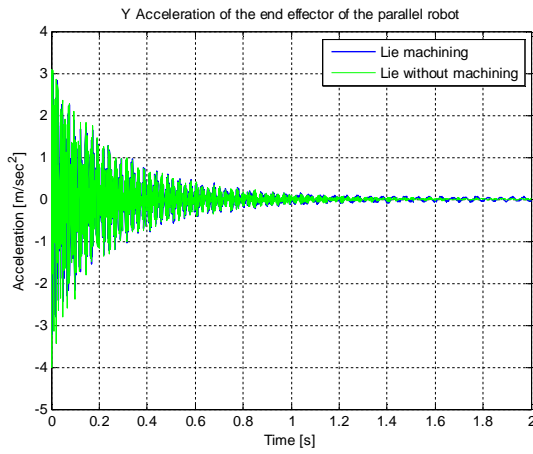


Figure 4.17: Y-acceleration of the end effector of a flexible parallel robot using the flexible Lie group method with and without machining forces.

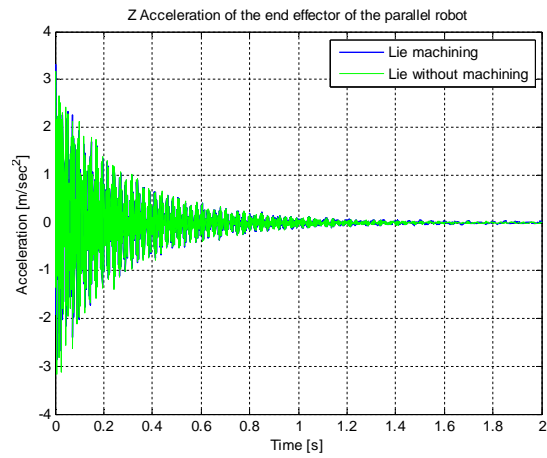


Figure 4.18: Z-acceleration of the end effector of a flexible parallel robot using the flexible Lie group method with and without machining forces.

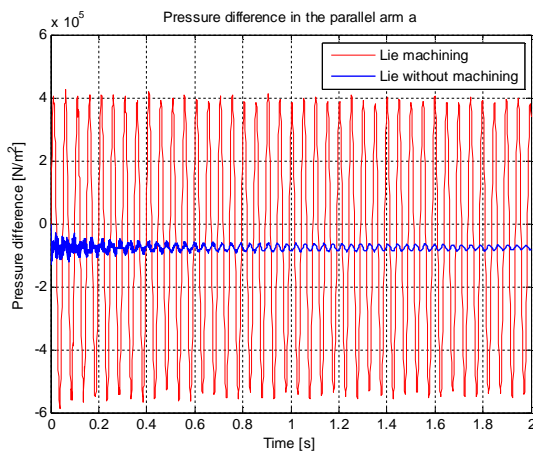


Figure 4.19: Difference in pressure in cylinder *a* of a flexible parallel robot using the flexible Lie group method with and without machining forces.

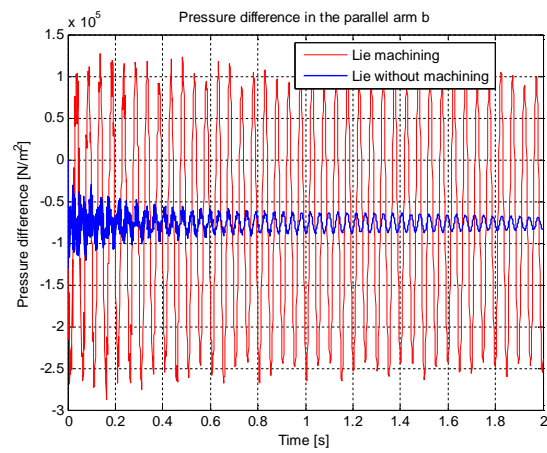


Figure 4.20: Difference in pressure in cylinder *b* of a flexible parallel robot using the flexible Lie group method with and without machining forces.

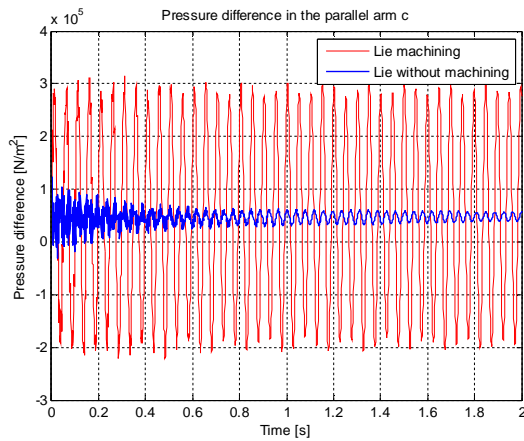


Figure 4.21: Difference in pressure in cylinder *c* of a flexible parallel robot using the flexible Lie group method with and without machining forces.

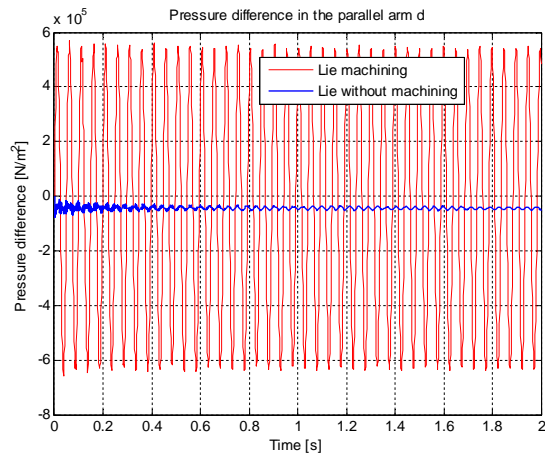


Figure 4.22: Difference in pressure in cylinder *d* of a flexible parallel robot using the flexible Lie group method with and without machining forces.

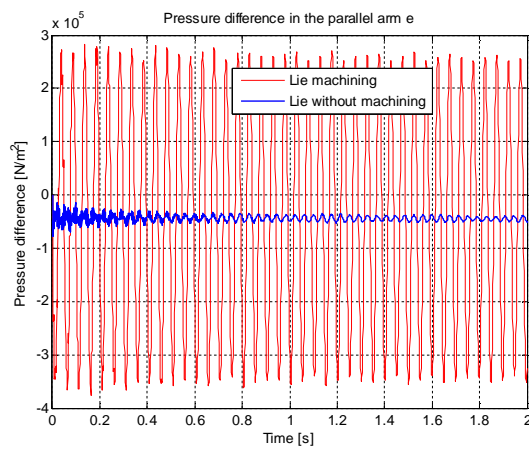


Figure 4.23: Difference in pressure in cylinder *e* of a flexible parallel robot using the flexible Lie group method with and without machining forces.

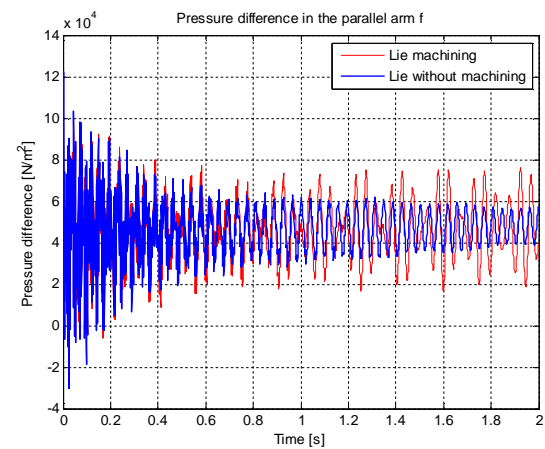


Figure 4.24: Difference in pressure in cylinder *f* of a flexible parallel robot using the flexible Lie group method with and without machining forces.



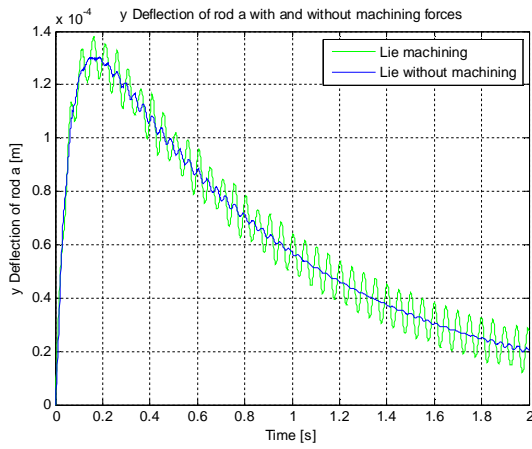


Figure 4.25: X component of deformation of the tip node of a flexible rod in cylinder *a* using the flexible Lie group method with and without machining forces.

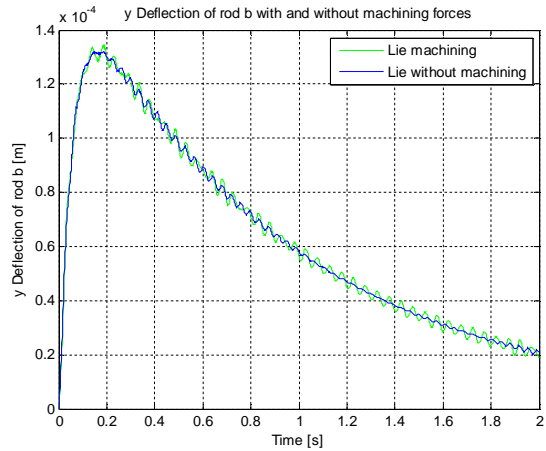


Figure 4.26: Y component of deformation of the tip node of a flexible rod in cylinder *a* using the flexible Lie group method with and without machining forces.

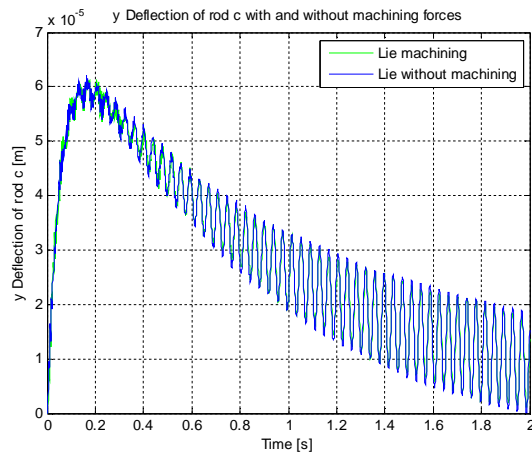


Figure 4.27: Z component of deformation of the tip node of a flexible rod in cylinder *a* using the flexible Lie group method with and without machining forces.

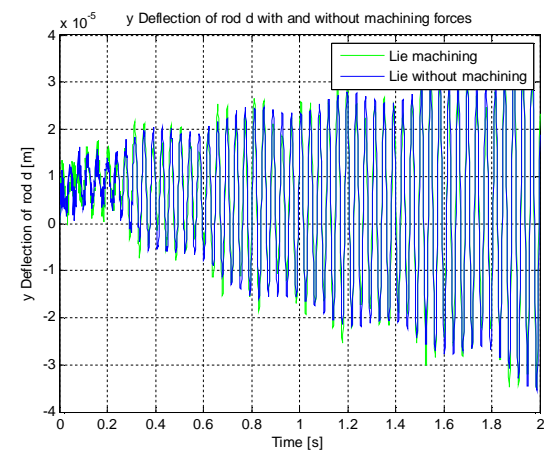


Figure 4.28: X component of deformation of the tip node of a flexible rod in cylinder *f* using the flexible Lie group method with and without machining forces.

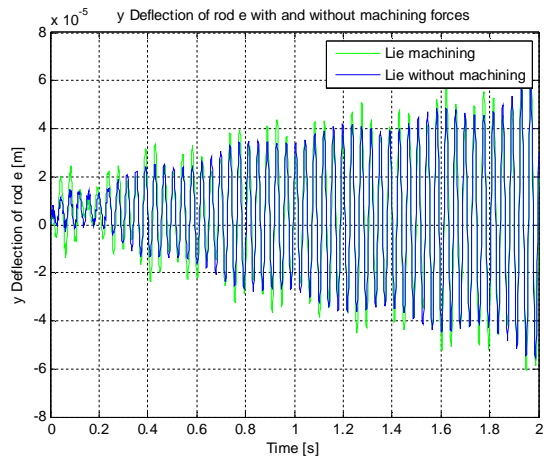


Figure 4.29: Y component of deformation of the tip node of a flexible rod in cylinder  $f$  using the flexible Lie group method with and without machining forces.

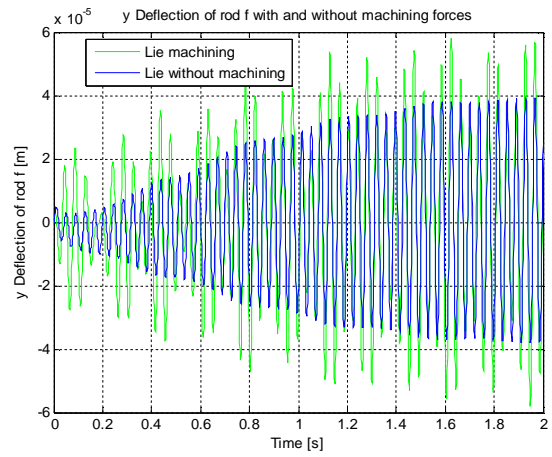


Figure 4.30: Z component of deformation of the tip node of a flexible rod in cylinder  $f$  using the flexible Lie group method with and without machining forces.

## 5 Conclusions

### 5.1 Key results of the work

A modular formulation has been presented for the dynamic analysis of a hybrid robot composed of a hybrid (serial 6-UPS parallel) robot with flexible rods and a control system. The coupled differential and algebraic equations are constructed numerically, and their time-integration is performed according to a strongly coupled approach.

#### Conclusion 1

The dynamic response to 3D machining forces was studied for a hydraulically driven hybrid (serial 6-UPS parallel) mechanism with flexible rods and joints. Cylinder rod flexibility was described using the Craig-Bampton method to reduce the order of the model. Applying the method, the rods were modeled using six beam elements. The coupling of rigid body motion and flexible motion was modeled using the floating frame of reference formulation. The components for the 6-closed-loop flexible rod mechanism were assembled using constrained Lagrange equations. The Lagrange multiplier method enables defining the overall system dynamic behavior. A linearized PID hydraulic control system was used to drive each arm and the serial robot during a typical machining process. The simulation results illustrate that the flexible rods and the moving plate undergo considerable vibration. Furthermore, due to the coupling effects of rigid body motions and elastic motions in the equation of motion, it is feasible to suppress the unwanted vibration of the flexible components using appropriate PID control gains for each rod sliding inside a cylinder. The PID control is stable and appropriate for machining operations.

Simulation results illustrate that achieving precise position control of the end effector in the hybrid robot for maximum precision machining can be accomplished by using the serial robot to hold the parallel robot in a fixed position. This results in minimal positional error being transmitted to the parallel part.

#### Conclusion 2

In chapter two, a hydraulically actuated hybrid robot was investigated. Thus far, the PID controller has been used to operate under difficult conditions in this system. However, since the gains of a manual PID controller have to be tuned by trial and error, obtaining optimal PID gains is very difficult without control design experience and time.

In order to improve the trajectory tracking performance of the parallel robot, which is part of the hybrid robot, fuzzy control and an ANFIS algorithm were proposed to adjust the parameters of the PID control. To evaluate the performance of the proposed control algorithms, the algorithms were compared with the simple PID control. The two controllers were used to control the end effector along a desired path. Both the fuzzy-PID and ANFIS-PID controllers are numerically simulated and the simulation results confirm the success of these controllers in trajectory tracking. The simulation results show that the two methods for tuning the PID controller have better performance than the PID controller in terms of the reduction in position tracking errors of the end effector. Amongst the control schemes developed, ANFIS tuning has provided the best results for the control of parallel robotic manipulators compared to the conventional control strategies. The neuro-adaptive learning techniques provide a method for fuzzy modeling procedures to learn information about data sets. This technique makes the fuzzy logic capable of computing the membership function parameters that best allow the associated fuzzy inference system to track the given input and output data. The result of the ANFIS PID tuning controller shows outstanding performance in terms of achieving the desired value with evident reductions in settling time and steady state errors. In conclusion, the ANFIS for tuning PID control represents a practical and valid alternative to parallel robot control. This has been proved with a MATLAB™ simulation of a parallel robotic manipulator.

A PID hydraulic control system was used to hold the serial robot in a fixed position to minimize the error being transmitted to the parallel robot using the equilibrium of the reaction forces at the hexa-element.

The tuning method used in this system by the ANFIS method has a good response without prior knowledge of the process. Also, this method enables better responses than the fuzzy-PID or only PID controllers. This control method is very useful for the process control system and helpful in the selection of the most appropriate range for servo valves operation.

### Conclusion 3

The dynamics of the hydraulically driven 6-UPS parallel robot with flexible rods and joints under the effect of 3D machining forces was studied. The mechanical part of the robot, which includes rigid bodies, kinematic joints, flexible rods and flexible sliding joints, is modeled using a formulation on the Special Euclidean group  $SE(3)$ . The flexibility of the rods was described using the formulation of a beam finite element in the Lie group framework, namely  $SE(3)$ . Applying the method, the rods were modeled using six beam elements. Based on this rigorous and systematic formalism, a nonlinear interpolation formula using an exponential map is introduced. The internal and inertial forces are derived from variational principles. The inertia forces are obtained from Hamilton's principle. Using the consistent interpolation formula for the velocity in the reference frame, a simplified formulation of the inertia forces is presented. It leads to a constant mass matrix and simplified gyroscopic forces. The equations of motion take

---

the form of a differential algebraic equation on a Lie group, which is solved using a Lie group time integration scheme.

The deformations and the forces are computed from the nodal values. The method relies on the local description of motions, so that it provides a singularity-free formulation, and no parameterization of the nodal variables needs to be introduced as in the method of FFRF. For the method, the rods were modeled using six beam elements. This method, unlike FFRF, depends on the nodal coordinates and does not depend on modal coordinates, making the numerical solution of the equation of motion more efficient. In addition, this method relies on a non-linear interpolation method using the exponential map, which introduces a natural coupling between position and rotation variables and exhibits important theoretical and numerical advantages. The flexible slider constraint is formulated with a Lie group and used for modeling a flexible rod sliding inside a cylinder, where an arc length parameter is introduced in order to define the exact location of the joint.

Assembling component models using Hamilton's principle and the Lagrange multiplier method for the six closed loop chains leads to the system dynamic model. The method allows writing systematically the equations of motion of the parallel robot by collecting generic expressions which are slightly tuned according to the system part of interest. The resulting equations of motion involve mixed nodal coordinates and kinematic joint transformation, and can be solved efficiently using the appropriate Lie group time integration scheme.

The proposed formulation exhibits some important advantages. The velocity of a rigid body is expressed in the local frame so that the mass matrix is constant. Since no parameterization of the global motion is introduced, the gyroscopic forces only depend on the velocity and the dependency is quadratic. Regarding the kinematic joints, a vectorial map is proposed to impose the constraints. Then, the constraint gradient at equilibrium only depends on the relative motion, but it does not depend on the global motion of the nodes it constrains, which reduces the non-linearity in the kinematic joints.

A linearized PID hydraulic control system was used to drive each arm. Simulation results illustrate that it is feasible to suppress the unwanted vibration of flexible components using appropriate PID control gains for each rod sliding inside a cylinder. Moreover, the PID control is stable and appropriate for machining operations. The resulting mechatronic model is monolithically solved in an efficient manner.

To examine the application of the  $SE(3)$  method to the modeling of the parallel robot machine affects the robot's ultimate performance, a comparison was made between the required path for the end effector of the parallel robot with and without machining forces. The results of the evolution of the differences in the pressures inside each cylinder helps to select the appropriate servo valve properties for the actual robot.

Finally, the simulation results indicate that the method of  $SE(3)$  is appropriate for a complex dynamic system like the 6-UPS parallel robot whose performances result from a specific control strategy.

## 5.2 Suggestions for improving performance of the hybrid robot and for the future work

The performance of the hybrid robot under study can be improved by the following suggestions:

- To obtain more accurate results, experimental tests should be implemented at different configurations when the manipulator is moving, considering the effect of nonlinear dynamics on modal shapes and frequencies.
- In order to make the model more realistic, the friction at the joint should be taken into consideration.
- The hydraulic model should be as realistic as possible.
- Although water hydraulics is clean and suitable for the environment inside the ITER vacuum vessel, using water hydraulics for the drive is a challenge because of its limited servo valve flow rate. High speeds result in greater than acceptable speed errors, and the robot will not track accurately. The performance and the speed of the hybrid robot could be further improved by, for example, replacing the hydraulic system by motorized roller screw actuators.
- From the deformation relations of the flexible rods, it was found that the machining forces are sustained majorly by the rods (d) and (e) (see Figure 2.5), moderately by the rods (c) and (f), and a little by the rods (a) and (b). Consequently, the rods (d) and (e) and each ball joint connected it to the end effector should be designed to have stiffness higher than that of rods (a) and (b).

---

## References

- Adhyaru, D. Patel, J. and Gianchandani, R. (2010). Adaptive Neuro-Fuzzy inference system based control of robotic manipulators. *Proceedings 2010 International Conference on Mechanical and Electrical Technology (ICMET 2010)*, IEEE, pp.353-358.
- Akbas, A. (2008). Application of Neural networks to modeling and control of parallel manipulators. ch-2 in the book of “*Parallel Manipulators, New Developments*, Book edited by: Jee-Hwan Ryu, ISBN 978-3-902613-20-2, April, I-Tech Education and Publishing, Vienna, Austria, pp. 21-40.
- Al-saedi, M. I. Wu, H. and Handroos, H. (2012). Flexible multibody dynamics and control of a novel hydraulically driven hybrid redundant robot machine. *the 2nd International Conference on Applied Robotics for the Power Industry CARPI 2012*, Zurich, Switzerland, 11-13 September 2012.
- Al-saedi, M. I. Wu, H., Handroos, H. and Rantalainen, T. (2014). Flexible multibody dynamics modelling and control of a hydraulically driven hybrid redundant robot machine. *accepted to be published in the Journal of Robotica*, 2014.
- Al-saedi, M. I. Wu, H. and Handroos, H. (2013). ANFIS and Fuzzy tuning of PID controller for trajectory tracking of a flexible hydraulically driven parallel robot machine. *Journal of Automation and Control Engineering*, ISSN: 2301-3702, Vol. 1, No. 2, March, pp. 70-77.
- Al-saedi, M. I. Wu, H. and Handroos, H. (2014). Intelligent controller of a flexible hybrid robot machine for ITER assembly and maintenance. *Journal of Fusion Engineering* (accepted to be published 2014).
- Aldair, A. A. (2010). FPG based ANFIC for full vehicle nonlinear active suspension systems. *IJAIA*, Vol. 1, No. 4, October.
- Arnold, V.I. (1989). *Mathematical Methods of Classical Mechanics*. 2-ed, Springer-Verlag, New York, Inc., Translated by K. Vogtmann and A. Weinstein.
- Arpaci, H. and Özgüven, Ö. F. (2011). ANFIS &  $PI\lambda D\mu$  controller design and comparison for overhead cranes. *Indian Journal of Engineering & Materials Sciences*, Vol. 18, June 2011, pp. 191-203.
- Bachir, O. and Zoubir, A. F. (2012). Adaptive Neuro-fuzzy inference system based control of Puma 600 robot manipulator. *International Journal of Electrical and Computer Engineering (IJECE)*, Vol. 2, No. 1, pp. 90-97, February. <http://iaesjournal.com/online/index.php/IJECE>.

- Bae, D. S. Han, J. M. (2000). An implementation method for constrained flexible multibody dynamics using a virtual body and joint. *Multibody System Dynamics*, 4(4), pp. 297-315.
- Brüls, Cardona, O. A. and Arnold, M. (2012). Lie group generalized- $\alpha$  time integration of constrained flexible multibody systems. *Mechanism and Machine Theory*, 48, pp. 121-137.
- Brüls, O., Arnold, M. and Cardona, A. (2011). Two Lie group formulations for dynamic multibody systems with large rotations. *In Proceedings of the IDETC/MSNDC Conference*, August 28-31, Washington, USA.
- Brüls, O. and Cardona, A. (2010). On the use of Lie group time integrators in multibody dynamics. *ASME Journal of Computational and Nonlinear Dynamics*, 5(3), July, pp. 031002-1-13.
- Brüls, O. and Arnold, M. (2008). The generalized- $\alpha$  scheme as a linear multistep integrator: toward a general mechatronic simulator. *ASME J. of Computational and Nonlinear Dynamics*, October, Vol. 3, pp. 041007-1-10.
- Brüls, O. (2005). *Integrated simulation and reduced-order modeling of controlled Flexible Multibody Systems*. Ph.D. thesis, University of Liege, Belgium.
- Boothby, W. (1986). *An introduction to differentiable manifolds and riemannian geometry*, Academic Press, 2nd edition.
- Carbone, G. (2001). Stiffness analysis and experimental validation of robotic systems. *Front. Mech. Eng.* 2011, 6(2): 182-196.
- Carbone, G., Ceccarelli, M., and Teolis, M. (2001). A numerical evaluation of the stiffness of CaHyMan (Cassino HybridManipulator), *2nd Workshop on Computational Kinematics CK 2001*, Seoul, pp.145-154.
- Craig, R. R. and Kurdila, A. J. (2006). *Fundamentals of structural dynamics*, 2nd ed John Wiley & Sons, New Jersey, USA.
- Craig, R. R. and Bampton, M. C. C. (1968). Coupling of substructures for dynamic analysis, *American Institute of Aeronautics and Astronautics Journal*, 6, pp. 1313-1319.
- Craig, J. J. (2005). *Introduction to robotics mechanics and control*, 3<sup>rd</sup> ed Pearson Education, Inc. Upper Saddle River, NJ 07458, USA.



- Crisfield, M. and Jelenic, G. (1999). Objectivity of strain measures in the geometrically exact three-dimensional beam theory and its finite-element implementation, *Proceedings of the Royal Society of London A* 455 (1999) 1125-1147.
- Dan, W., Jianguo, J. and Jietao, W. (2010). The model and simulation of an asymmetric valve controlled cylinder velocity control system based on PID. *2010 Second International Workshop on Education Technology and Computer Science*, DOI 10.1109/ETCS.2010.370.
- De Jalon, J. G. and Bayo, E. (1994). Kinematic and dynamic simulation of multibody systems: The real time challenge, Springer-Verlag, New York.
- Dorf, R. C. and Bishop, R. H. (2005). *Modern control systems* 10th ed. Pearson Prentice Hall.
- Fattah, A., Angeles, J., and Misra, A.K. (1995). Dynamics of a 3-DOF spatial parallel manipulator With Flexible Links. *Proceedings IEEE International Conference on Robotics and Automation*, Vol. 1, pp. 627-632.
- Feng, B., Gong, G. and Yang, H. (2009). Self-tuning-parameter fuzzy PID temperature control in a large hydraulic system. In *Proceedings of the IEEE/ASME International Conference on Advanced Intelligent Mechatronics*, Singapore, July 14-17, pp.1413-1422.
- Gao, Y. F., Dong, X. and Zhao, X. (2011). Dynamics analysis and characteristics of the 8-PSS flexible redundant parallel manipulator, *Journal of Robotics and Computer-Integrated Manufacturing*, pp. 918-928, 27(2011).
- Geradin, M., Cardona, A., Doan, D.B., and Duysens, J. (1994). Finite element concepts in multibody dynamics. chapter in *Computer-Aided Analysis of Rigid and Flexible Mechanical Systems*, M. F. O. S. Pereira and I. A. C. Ambrosio (eds.), 233-284, Kluwer Academic Publishers.
- Geradin, M. (1993). Computational Aspects of The finite element approach to flexible multibody systems. W. Schielen (ed.), *Advanced Multibody System Dynamics*, pp. 337-354, Kluwer Academic Publishers. Printed in Netherlands.
- Geradin, M. and Cardona, A. (2001). *Flexible Multibody Dynamics: A Finite Element Approach*, John Wiley & Sons, Chichester.
- Haug, E. J. (1989). *Computer-Aided Kinematics and Dynamics of Mechanical Systems Volume I: Basic Methods*, Allyn and Bacon, Massachusetts.
- Hwang R. S. and Haug, E. J. (1990). Translational joints in flexible multibody dynamics. *Mechanics of Structures and Machines*, 18(4), pp. 543-564.

- Hopkins, B. R. and Williams II, R.L. (2002). Kinematics, design and control of the 6-PSU platform, in *Proceedings Industrial Robot*, Vol. 29, no. 5, pp. 443-451.
- Indrawanta and A. Santoso, (2009). Design and control of the Stewart platform robot. in *Proceedings Third Asia International Conference on Modeling & Simulation*, IEEE, pp.475-480.
- Jang, J. Sun, C. and Mizutani, E. (1997). *Neuro-Fuzzy and Soft Computing*, Prentice Hall, Upper Saddle River, NJ, USA.
- Jazar, R.N. (2007). *Theory of Applied Robotics: kinematics, Dynamics, and Control*, Springer Science +Business Media, LLC, New York.
- Khoury, G. M., Saad, M., Kanaan, H. Y., and Asmar, C. (2004). Fuzzy PID control of a five DOF robot arm, *Journal of Intelligent and Robotic Systems*, 40:299-320.
- Korkealaakso, P. Mikkola, A. Rantalainen, T. and Rouvinen A. (2009). Description of joint constraints in the floating frame of reference formulation. *Proceedings IMechE* Vol. 223 Part K: J. Multi-body Dynamics JMBD170, IMechE.
- Lee, J. D. and Geng, Z. (1993). A dynamic model of a flexible Stewart platform. *J. of Computers and Structures*, Vol. 48, No. 3, pp. 367-374.
- Lee, S., Park, T., Seo, J., Yoon, J., and Jun, K. (2008). The development of a sliding joint for very flexible multibody dynamics using absolute nodal coordinate formulation. *Multibody System Dynamics*, 20:223-237.
- Li, Y. Wang, Y. and Chen, Z. (2008). Research on trajectory tracking of a parallel robot based on Neural network PID control, *Proceedings of the IEEE International Conference on Automation and Logistics*, Qingdao, China, Sept. 2008, pp, 504-508.
- Mamdani, E. H. (1974). Application of fuzzy algorithms for the control of a simple dynamic plant. *In Proceedings of the IEEE*, 121-159.
- Mohammadipanah, H. and Zohoor, H. (2009). Design and Analysis of a Novel 8-DOF Hybrid Manipulator, World Academy of Science, Engineering and Technology 58.
- Melba Mary, P., Marimuthu, N. S., and Albert Singh, N. (2007). Design of intelligent self-tuning temperature controller for water bath process. (*International Journal of Imaging Science and Engineering (IJISE)*), GA, USA, ISSN:1934-9955, VOL. 1, NO. 4, October, pp. 121-124.
- Murray, R. M. Li, Z. and Sastry, S. S. (1994). *A mathematical introduction to robotic manipulation*, CRC Press.

- Ngo, T. Wang, Y. N. Mai, T. L. Nguyen, M.H. and Chen, J. (2012). Robust adaptive Neural-Fuzzy network tracking control for robot manipulator. *International J. Computer Community*, ISSN 1841-9836, Vol. 7, No. 2, pp. 341-352, June.
- Nguyen, H.T., Prasad, N.R., Walker, C.L., Walker, E.A. (2003). *A First Course in Fuzzy and Neural Control*, published by Chapman & Hall/CRC, Florida, USA.
- Pessi, P. Wu, H. Handroos H. and Jones, L. (2007). A mobile robot with parallel kinematics to meet the requirements for assembling and machining the ITER vacuum vessel. *Fusion Engineering and Design*, 82, pp. 2047-2054.
- Przemieniecki, J.S. (1985). *Theory of Matrix Structural Analysis*. Dover Publications, New York.
- Passino, K. M. and Yurkovich, S. (1997). *Fuzzy Control*, Addison Wesley Longman, Inc., 2725 Sand Hill Road, Menlo Park, California 94025, USA.
- Park, J. and Chung, W. (2005). Geometric integration on Euclidean Group with application to articulated multibody systems. *IEEE Transactions on Robotics*, 21, pp. 850-863.
- Ravi, S., Sudha, M. and Balakrishnan, P. A. (2011). Design of Intelligent self-tuning GA ANFIS temperature controller for plastic extrusion system. *Journal of Modeling and Simulation in Engineering*, Hindawi Publishing Corporation, Vol. 2011, Article ID 101437, 8 pages.
- Seifried, R., Held, A., and Dietmann, F. (2011). Analysis of feed-forward control design approaches for flexible multibody systems. *Journal of System Design and Dynamics, Special Issue ACMD 2010*, Vol. 5, No. 3, pp. 429-440.
- Sunada, W. and Dubowsky, S. (1983). On the dynamic analysis and behavior of Industrial robotic manipulators with elastic members. *Transactions of the ASME*, Vol. 105, pp. 42-51, MARCH.
- Shabana, A. A. (2005). *Dynamics of Multibody Systems*, (third edition), Cambridge University Press.
- Shabana, A. A. (1996). *Vibration of Discrete and Continuous Systems*, Springer-Verlag, New York, USA.
- Shabana, A. A. and Wehage, R. A. (1983). Coordinate reduction technique for transient analysis of spatial substructures with large angular rotations. *J. of Structural Mechanics*, 11(3), pp. 401-431.
- Spanos, J. T. and Tsuha, W. S. (1991). Selection of component modes for flexible multibody simulation. *J. Guidance*, March-April 1991, Vol. 14, No. 2, pp. 278-286.

- Slotine, J. E. and Li, W. (1991). *Applied Nonlinear Control*, Prentice-Hall, Englewood Cliffs, NJ.
- Sugiyama, H. J., Escalona, J. L., and Shabana, A. A. (2003). Formulation of three-dimensional joint constraints using the absolute nodal coordinates. *Nonlinear Dynamics*, 31:167-195.
- Simo, J. (1985). A finite strain beam formulation. The three-dimensional dynamic problem. Part I, *Computer Methods in Applied Mechanics and Engineering* 49 , 55-70.
- Sonneville, V. and Brüls, O. (2014). A formulation on the Special Euclidean group for dynamic analysis of multibody systems. *Journal of Computational and Nonlinear Dynamics*.
- Sonneville, V., Cardona, A. and Brüls., O. (2014). Geometrically exact beam finite element formulated on the special Euclidean group  $SE(3)$ . *Computer Methods in Applied Mechanics and Engineering*, 268:451-474, January.
- Spivak, M. (1999). *A comprehensive Introduction to Differential Geometry*, Vol. 1, 3<sup>rd</sup> ed., PUBLISH OR PERISH, Inc., Huston, Texas.
- Takagi, T., and Sugeno, M. (1985). Fuzzy identification of systems and its applications to modeling and control, Systems, Man and Cybernetics, *IEEE Transactions On Systems, Man, And Cybernetics*, Vol. SMC-15, no.1, pp.116,132, Jan.-Feb.
- Tian, L. (2004). Intelligent self-tuning of PID control for the robotic testing system for human musculoskeletal joints test, *Annals of Biomedical Engineering*, Vol. 32, No.6, June, pp:899-909.
- Vakil, M. Fotouhi, R. Nikiforuk, P. N. and Salmasi, H. (2008). A constrained Lagrange formulation of multilink planar flexible manipulator. *Transactions of the ASME Journal of Vibration and Acoustics*, June, Vol. 130, pp. 031007-1-16.
- Wang, H. Xing, Li, Y. Y. and Li, Z. (2010). Dynamic modeling of five-bar manipulator with structurally flexible linkages. *Proceedings of the 8th World Congress on Intelligent Control and Automation*, July 6-9, Jinan, China.
- Wang, X. and Mills, J. K. (2006). Dynamic modeling of a flexible-link planar parallel platform using a substructuring approach. *J. Mechanism and Machine Theory* 41, pp: 671-687.
- Wang, X. and Mills, J. K. (2004). A FEM model for active vibration control of flexible Linkages. *Proceedings of the 2004 IEEE International Conference on Robotics & Automation*, April, New Orleans, LA, USA.

- Wang, X. and Mills, J. K. (2004). Substructuring dynamic modeling and active vibration control of smart parallel platform. *Proceedings of the IMECE2004, 2004 ASME International Mechanical Engineering Congress*, Anaheim, November 13-19, USA.
- Wang, X., Yang, X., Liu, G. and Qin, H. (2009). Adaptive neuro-fuzzy inference systems PID controller for SG water level of nuclear power plant. *Proceedings of the Eighth International Conference on Machine Learning and Cybernetics*, IEEE, baoding, 12-15 July, pp. 567-572.
- Wiens, G. and Hardage, D. (2006). Structural dynamics and system identification of parallel kinematic machine. *Proceedings of IDETC/CIE 2006, ASME 2006 Int.Dsign Eng.Technical Conferences & Computers and Information in Engineering Conference*, SEP. 10-13, Philadelphia, Pennsylvania, USA.
- Wesley, H. J. (1997). *Fuzzy and Neural Approaches in Engineering, MATLAB Supplement*, Wiley-Interscience, John Wiley and Sons, New York, NY, USA.
- Wu, H., Wang, Y., Li, M., Al-saedi, M., and Handroos, H. (2014). Chatter suppression methods of robot machines for ITER vacuum vessel assembly and maintenance. *Journal of Fusion Engineering (paper accepted to be published in the Journal of Fusion Engineering, in press, 2014)*.
- Xu, Q. and Li, Y. (2007). A 3-PRS Parallel Manipulator Control Based on Neural Network. in *Advances in Neural Networks - ISSN 2007*, D. Liu, S. Fei, Z.-G. Hou, H. Zhang, and C. Sun, Eds., Springer, 2007, ISBN: 978-3-540-72382-0, Lecture Notes in Computer Science 4491, Part I, pp. 757-766.
- Yoo, W. S. and Haug, E. J. (1986). Dynamics of flexible mechanical systems using vibration and static correction modes. *Journal of Mechanisms, Transmissions and Automation in Design*, 108(3), pp. 315-322.
- Yoo, W. S. and Haug, E. J. (1986). Dynamics of articulated structures, Part I: Theory and Part II: computer implementation and application . *J. Struct. Mech.*, 14, pp. 105-106 and pp. 177-187.
- Yongsheng, Z. Zhifeng, L. Ligang, C. and Wentong , Y. (2010). Enhanced fuzzy sliding mode controller for a 3-DOF parallel link manipulator. *Proceedings 2nd International Asia Conference on Informatics in Control, Automation and Robotics CAR 2010*, pp. 167-171.
- Zadeh, Lotfi A. (1965). Fuzzy sets. *Information and Control.*; 8: 338–353.
- Zhang, X. Mills, J.K. and Cleghorn, W.L. (2007). Study on the effect of elastic deformations on rigid body motions of a 3-PRR flexible parallel manipulator.

---

*Proceedings of the 2007 IEEE Int. Conference on mechatronics and Automation*, August 5-8, Harbin, China.

Zhaocai, D. and Yueqing, Y. (2008). Dynamic modeling and inverse dynamic analysis of flexible parallel robots. *International Journal of Advanced Robotics Systems*, ISSN 1729-8806, Vol. 5, No.1, pp.115-122.

Zhou, Z. Xi, J. and Mechefske, C. K. (2006). Modeling of a fully flexible 3-PRS manipulator for vibration analysis. *Journal of Mechanical Design, ASME*, MAR, Vol.128, pp. 403-412.

Zhou, Z. Mechefske, C. K. and Xi, J. (2007). Nonstationary vibration of a fully flexible parallel kinematic machine. *J. of ASME vib. and Acoust*; 129(2), pp. 623-630.

## ACTA UNIVERSITATIS LAPPEENRANTAENSIS

536. TORKKELI, LASSE. The influence of network competence of internationalization of SMEs. 2013. Diss.
537. MOLANDER, SOLE. Productivity and services – safety telephone services for the elderly. 2013. Diss.
538. SITARZ, ROBERT. Identification of research trends in the field of separation processes. Application of epidemiological model, citation analysis, text mining, and technical analysis of the financial markets. 2013. Diss.
539. KATTEDEN, KAMIEV. Design and testing of an armature-reaction-compensated permanent magnet synchronous generator for island operation. 2013. Diss.
540. HÄMÄLÄINEN, HARRI. Integration of learning supportive applications to development of e-portfolio construction process. 2013. Diss.
541. RATCHANANUSORN, WARIN. Development of a process for the direct synthesis of hydrogen peroxide in a novel microstructured reactor. 2013. Diss.
542. PERFILEV, DANIIL. Methodology for wind turbine blade geometry optimization. 2013. Diss.
543. STROKINA, NATALIYA. Machine vision methods for process measurements in pulping. 2013. Diss.
544. MARTTONEN, SALLA. Modelling flexible asset management in industrial maintenance companies and networks. 2013. Diss.
545. HAKKARAINEN, JANNE. On state and parameter estimation in chaotic systems. 2013. Diss.
546. HYYPIÄ, MIRVA. Roles of leadership in complex environments  
Enhancing knowledge flows in organisational constellations through practice-based innovation processes. 2013. Diss.
547. HAAKANA, JUHA. Impact of reliability of supply on long-term development approaches to electricity distribution networks. 2013. Diss.
548. TUOMINEN, TERHI. Accumulation of financial and social capital as means to achieve a sustained competitive advantage of consumer co-operatives. 2013. Diss.
549. VOLCHEK, DARIA. Internationalization of small and medium-sized enterprises and impact of institutions on international entrepreneurship in emerging economies: the case of Russia. 2013. Diss.
550. PEKKARINEN, OLLI. Industrial solution business – transition from product to solution offering. 2013. Diss.
551. KINNUNEN, JYRI. Risk-return trade-off and autocorrelation. 2013. Diss.
552. YLÄTALO, JAAKKO. Model based analysis of the post-combustion calcium looping process for carbon dioxide capture. 2013. Diss.
553. LEHTOVAARA, MATTI. Commercialization of modern renewable energy. 2013. Diss.
554. VIROLAINEN, SAMI. Hydrometallurgical recovery of valuable metals from secondary raw materials. 2013. Diss.
555. HEINONEN, JARI. Chromatographic recovery of chemicals from acidic biomass hydrolysates. 2013. Diss.

556. HELLSTÉN, SANNA. Recovery of biomass-derived valuable compounds using chromatographic and membrane separations. 2013. Diss.
557. PINOMAA, ANTTI. Power-line-communication-based data transmission concept for an LVDC electricity distribution network – analysis and implementation. 2013. Diss.
558. TAMMINEN, JUSSI. Variable speed drive in fan system monitoring. 2013. Diss.
559. GRÖNMAN, KAISA. Importance of considering food waste in the development of sustainable food packaging systems. 2013. Diss.
560. HOLOPAINEN, SANNA. Ion mobility spectrometry in liquid analysis. 2013. Diss.
561. NISULA, ANNA-MAIJA. Building organizational creativity – a multitheory and multilevel approach for understanding and stimulating organizational creativity. 2013. Diss.
562. HAMAGUCHI, MARCELO. Additional revenue opportunities in pulp mills and their impacts on the kraft process. 2013. Diss.
563. MARTIKKA, OSSI. Impact of mineral fillers on the properties of extruded wood-polypropylene composites. 2013. Diss.
564. AUVINEN, SAMI. Computational modeling of the properties of TiO<sub>2</sub> nanoparticles. 2013. Diss.
565. RAHIALA, SIRPA. Particle model for simulating limestone reactions in novel fluidised bed energy applications. 2013. Diss.
566. VIHOLAINEN, JUHA. Energy-efficient control strategies for variable speed controlled parallel pumping systems based on pump operation point monitoring with frequency converters. 2014. Diss.
567. VÄISÄNEN, SANNI. Greenhouse gas emissions from peat and biomass-derived fuels, electricity and heat – Estimation of various production chains by using LCA methodology. 2014. Diss.
568. SEMYONOV, DENIS. Computational studies for the design of process equipment with complex geometries. 2014. Diss.
569. KARPPINEN, HENRI. Reframing the relationship between service design and operations: a service engineering approach. 2014. Diss.
570. KALLIO, SAMULI. Modeling and parameter estimation of double-star permanent magnet synchronous machines. 2014. Diss.
571. SALMELA, ERNO. Kysyntä-toimitusketjun synkronointi epävarman kysynnän ja tarjonnan toimintaympäristössä. 2014. Diss.
572. RIUNGU-KALLIOSAARI, LEAH. Empirical study on the adoption, use and effects of cloud-based testing. 2014. Diss.
573. KINNARINEN, TEEMU. Pressure filtration characteristics of enzymatically hydrolyzed biomass suspensions. 2014. Diss.
574. LAMMASSAARI, TIMO. Muutos kuntaorganisaatiossa – tapaustutkimus erään kunnan teknisestä toimialasta. 2014. Diss.
575. KALWAR, SANTOSH KUMAR. Conceptualizing and measuring human anxiety on the Internet. 2014. Diss.
576. LANKINEN, JUKKA. Local features in image and video processing – object class matching and video shot detection. 2014. Diss.



